Astronomy Letters, Vol. 29, No. 12, 2003, pp. 783–790. Translated from Pis'ma v Astronomicheskiĭ Zhurnal, Vol. 29, No. 12, 2003, pp. 883–891.

On the Detectability of Turbulence and Bulk Flows in X-ray Clusters*

R. A. Sunyaev[**1,2], **M. L. Norman**[1,3], **and G. L. Bryan**[4]

[1]*Max-Planck-Institut für Astrophysik, Karl-Schwarzschild-Strasse 1, 85748 Garching, Germany*

[2]*Space Research Institute, Russian Academy of Sciences, Profsoyuznaya ul. 84/32, Moscow, 117810 Russia*

[3]*Physics Department and CASS, University of California at San Diego, CA 92093, USA*

[4]*Department of Physics, University of Oxford, Keble Road, Oxford, Great Britain*

Received July 11, 2003

Abstract—Cooling flows, cluster mergers, and the motions of galaxies through cluster gas with supersonic and sonic velocities must lead to large scale motions of the intracluster medium (ICM). A high-resolution numerical simulation of X-ray cluster formation by Norman and Bryan (1999) predicts cluster-wide turbulence with $v_{\rm turb} \sim 300$–600 km s^{-1} and eddy scales $l_{\rm outer} \sim 100$–500 kpc, the larger numbers being characteristic of turbulence near the virial radius, while the smaller numbers pertain to the core. The simulation also predicts the existence of ordered bulk flows in the core with $v \sim 400$ km s^{-1} on scales of several hundred kpc. In this paper, we consider the observability of such fluid motions via the distortions they induce in the CMB via the kinematic SZ effect, as well as via Doppler broadening and shifting of metal lines in the X-ray spectrum. We estimate $|\Delta T/T|_{\rm kinematic} <$ few $\times 10^{-6}$—at or below current limits of detectability. However, we find that an energy resolution of a few eV is sufficient to detect several Doppler shifted components in the 6.7 keV Fe line in the cluster core. © *2003 MAIK "Nauka/Interperiodica".*

Key words: *cosmology—galaxies: clusters—X-rays: galaxies.*

INTRODUCTION

Independent lines of observational evidence show that a large fraction of nearby clusters of galaxies are dynamically young. These include the detection of substructure in optical and X-ray surveys (Geller and Beers 1982; Dressler and Shectman 1988, Jones and Forman 1992), non-Maxwellian galaxy velocity distributions in clusters containing substructure (Beers *et al.* 1990; Pinkney *et al.* 1996), X-ray surface brightness distortions (Mohr *et al.* 1993; Buote and Tsai 1995), and X-ray temperature substructure (Markevitch *et al.* 1994). These features can be understood as the result of cluster mergers (e.g., Roettiger *et al.* 1996), which are predicted in hierarchical structure formation scenarios (e.g., White *et al.* 1993).

Cluster mergers induce large-scale bulk flows with velocities on the order of the virial velocity ($\sim$1000 km s^{-1} for rich clusters). Cluster-wide turbulence will then be established in the intracluster medium (ICM) in a few turnover times of the largest eddies $\tau \sim r_{\rm vir}/\sigma_{\rm vir} \sim 10^9$ yr. We expect the turbulence to possess a Kolmogorov-like spectrum down to the dissipation scale $l_{\rm diss} \sim l_{\rm outer}/{\rm Re}^{3/4}$, where Re is the Reynolds number. Due to the low densities and high temperatures of the ICM plasma, the Coulomb mean free path is on the order of 10–100 kpc, yielding the classical estimate $Re \sim 100$. However, the presence of a weak magnetic field will reduce transport coefficients from the Spitzer values by a factor of $\sim 1/M^2$, where $M = \dfrac{v}{\sqrt{B^2/4\pi\rho}}$ is the Alfvén Mach number (Tao 1995). Using typical values for X-ray cluster cores (halos) of $v = 300$ (600) km s^{-1}, $n = 10^{-3}$ (10^{-5}) cm^{-3}, and $B = 10^{-6}$ (10^{-8}) G, we find $M^2 \sim 10$ (10^4). This increases the effective Reynolds number to $\sim 10^3$ (10^6), predicting dissipation scales of $\sim$5 kpc (30 pc), assuming that $l_{\rm outer} = 1$ Mpc.

There are two ways to study the nature and importance of these motions (i.e., their contribution to the local pressure of the gas, their mixing of the high Z elements in the cluster, and their contribution to ion heating due to dissipation on the smallest scales). First, through numerical simulation of the evolution of the gas in the cluster, taking into

*This paper was written in 2000 prior to the launch of ASTRO-E, but was never submitted or published due to the unfortunate loss of that spacecraft. We release it now without major changes in anticipation of the launch of ASTRO-E2, which should have sufficient resolution to see the effects predicted here.

**E-mail: sunyaev@hea.iki.rssi.ru

account the evolution of the gravitational potential, mergings, heating and cooling of the gas, formation of the cooling flows, etc. Recently, Norman and Bryan (1999a) published their results of such simulations. Second, to use X-ray spectroscopy missions (under construction now and under consideration) to measure the real distribution of velocities in rich clusters of galaxies. We are excited by the progress in the energy resolution of the AXAF and XMM (with X-ray grating), the ASTRO-E (with X-ray bolometers). The CONSTELLATION and XEUS projects planned for launch by NASA and ESA in the middle of the next decade would have 1–2 eV energy resolution across the whole band from 1 to 7 keV. Such energy resolution will permit measurements of velocities as low as 50–100 km s^{-1}, more than an order of magnitude lower than the speed of sound in rich clusters of galaxies.

In this paper we use the published data on the velocity distribution in a simulated rich cluster of galaxies (Norman and Bryan 1999a) to demonstrate that the observations of X-ray lines with high energy resolution would open up a new method of investigating the large-scale intergalactic gas velocity distribution in clusters of galaxies. It is important for us that we are dealing with heavy elements and especially with iron, which is 56 times heavier than hydrogen and, therefore, its thermal velocity (and corresponding thermal line broadening) is 7.5 times lower than the proton thermal velocity. This opens the way to measure subsonic turbulent velocities.

Observations and simulations have shown that the gas in the cluster is not isothermal (Markevitch *et al.* 1998, Frenk *et al.* 1999). Using lines of different ions and elements we are able to measure the velocity distribution in the regions with different temperatures in the same line of sight. We note that there is only one way to compete with X-ray observations to measure cluster gas motions. This is to observe the microwave hyperfine structure lines of heavy ions (for example, the 3.03 mm line of lithium-like iron-57) (Sunyaev and Churazov 1984). These lines are analogous to the 21 cm line of hydrogen. Unfortunately they are not sufficiently bright; therefore, it is better to observe the broadening of X-ray lines.

THE NUMERICAL SIMULATION

We have simulated the formation of an adiabatic X-ray cluster in an $\Omega = 1$ universe. The initial spectrum of density fluctuations is CDM-like with a shape parameter of $\Gamma = 0.25$ (Efstathiou *et al.* 1992). The cluster itself is a 3σ fluctuation at the center of the box for a Gaussian filter of 10 Mpc radius. We use a Hubble constant of 50 km s^{-1} Mpc^{-1} and a baryon fraction of 10%. This cluster is the subject of a comparison project between 12 different simulation methods, the results of which can be found in Frenk *et al.* (1999).

The evolution of gas and dark matter is computed using a method new to numerical cosmology: adaptive mesh refinement (AMR). AMR utilizes a logical hierarchy of finer resolution meshes in regions of the calculation which require high resolution (in our case, collapsing halos of dark matter and gas). AMR is adaptive, automatic, and recursive: an arbitrary number of submeshes of different levels of resolution are automatically created as the solution evolves. Within each submesh, the equations of adiabatic gas dynamics are solved subject to boundary conditions interpolated from overlying coarser meshes, using the piecewise parabolic method (PPM) as modified for cosmology by Bryan *et al.* (1995). Dark matter dynamics is solved using an adaptive particle-mesh (APM) algorithm inspired by Couchman's (1991) algorithm. Details of the method can be found in Bryan and Norman (1997), and Norman and Bryan (1999b).

The simulation was initialized with two grids at two levels of refinement. The first is the root grid covering the 64 Mpc^3 triply periodic domain with 64^3 cells. The second grid is also 64^3 cells, but is only 32 Mpc on a side and is centered on the cluster. Thus, over the region that forms the cluster, we have an initial cell size of 500 kpc leading to an approximate mass resolution of $8.7 \times 10^8 M_\odot$ ($7.8 \times 10^9 M_\odot$) for the baryons (dark matter). Cells are flagged for refinement when the baryon mass exceeds $4M_{\rm initial} \approx 3.5 \times 10^9 M_\odot$. We use a refinement factor of $R = 2$; thus, immediately after refinement, a refined cell's baryon mass will be $0.5M_{\rm initial}$. As the simulation evolves, as many as ~400 grids at seven levels of refinement are created, with a minimum cell size of 64 Mpc/$64 \times 2^7 = 7.8$ kpc. Our method thus maintains mass resolution in the gas and dark matter, while providing high force resolution where needed. In this regard, we accomplish the same thing as an adaptive smoothing length SPH calculation (e.g., Navarro *et al.* 1995) with a less viscous, more accurate shock-capturing hydrodynamic scheme. This is a distinct advantage in simulations of cluster turbulence.

Figure 1 shows radial profiles of the spherically averaged gas and dark matter velocity dispersions in the cluster at $z = 0$. The cluster centroid is taken to be the point of maximum total density. The dark matter velocity dispersion is computed after subtracting the mean cluster peculiar velocity inside a sphere of radius $r_{200} = 2.2$ Mpc. It shows the characteristic quasi-isothermal plateau $\sigma \simeq \sigma_{\rm vir}$ for $0.05 \leq r/r_{\rm vir} \leq 0.5$, sharply declining in the outer and inner parts of

the cluster, as discussed by Frenk *et al.* (1999). The gas velocity dispersion exhibits a different profile from the dark matter as the kinetic temperature contribution is not included. Only peculiar fluid velocities due to bulk motions or turbulence are reflected here. We compute the fluid velocity dispersions relative to the mean fluid peculiar velocity inside spheres of three different radii: 0.01, 0.1, and 1 $r_{\rm vir}$. The curves for 0.1 and 1 $r_{\rm vir}$ are nearly identical, and show that fluid peculiar velocities are dominated by infall for $r \geq r_{\rm vir}$. Inside the main cluster shock at $r \approx r_{\rm vir}$, the ICM is in a turbulent state (Bryan and Norman 1998, Norman and Bryan 1999a), with $\sigma_{\rm gas}$ declining from 800 to $\sim$400 km s^{-1} at $r = 0.5 r_{\rm vir}$. The turbulent velocities are roughly constant inside $0.5 r_{\rm vir}$, which is a significant new result of our simulation. Visual inspection of the flowfield reveals turbulent eddies with a range of sizes of 50-500 kpc. In addition, the flowfield in the central few hundred kpc exhibits an ordered circulation with $v \simeq 400$ km s^{-1}. Visualizations of the velocity field can be found in Norman and Bryan (1999a) and at the web site http://zeus.ncsa.uiuc.edu:8080/Xray/clusters.html.

In the following sections, we explore whether such fluid motions are detectable.

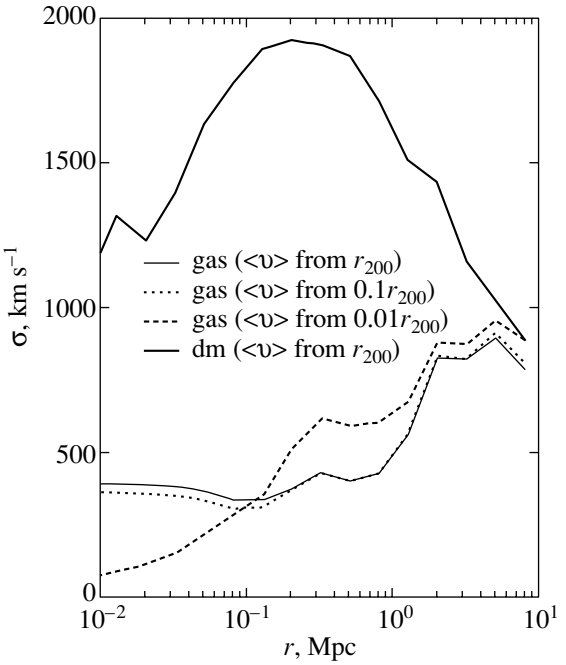

Fig. 1. Spherically averaged profiles of gas (thin lines) and dark matter (heavy line) 3D velocity dispersions in the simulated X-ray cluster. The gas velocity dispersions are computed relative to the center-of-mass velocities inside spheres of different radii: (r_{200} (thin solid line); $0.1r_{200}$ (thin dotted line); and $0.01r_{200}$ (thin dashed line). The plateau in $\sigma_{\rm gas} \sim 400$ km s^{-1} for $r \leq 1$ Mpc is indicative of bulk velocities/turbulence in the cluster gas.

RESULTS

Kinematic and Thermal SZ *Effect*

A hot ICM will inverse Compton scatter the cosmic microwave background radiation, boosting photons to higher frequencies and distorting the Planck blackbody spectrum (Sunyaev and Zel'dovich 1970, 1980). In the Rayleigh-Jeans part of the spectrum, the temperature decrement due to this effect is $\Delta T/T = -2y$, where y is the line of sight integral of the gas pressure through the ICM

$$y = \int_{-\infty}^{\infty} \frac{kT_{\rm e}}{m_{\rm e}c^2} \sigma_{\rm T} n_{\rm e} dl, \qquad (1)$$

$T_{\rm e}, m_{\rm e}$, and $n_{\rm e}$ are the electron temperature, mass, and number density and $\sigma_{\rm T}$ is the Thompson scattering cross section. In addition to this *thermal* effect, which is insensitive to fluid motions in the ICM, there is also a *kinematic* effect, which up to the first order in $\frac{v}{c}$ is

$$\frac{\Delta T}{T} = -\frac{1}{c} \int_{-\infty}^{\infty} \sigma_{\rm T} n_{\rm e} v_{||} dl. \qquad (2)$$

independent of frequency. Here, $v_{||}$ is the line-of-sight component of the cluster gas peculiar velocity (i.e., relative to the CMB frame). The total temperature decrement is the sum of these two effects:

$$\left.\frac{\Delta T}{T}\right|_{\rm tot} = \left.\frac{\Delta T}{T}\right|_{\rm thermal} + \left.\frac{\Delta T}{T}\right|_{\rm kinematic} = \left[-2\frac{k\langle T_{\rm e}\rangle}{m_{\rm e}c^2} + \frac{\langle v_{||}\rangle}{c}\right]\tau_{\rm T}, \qquad (3)$$

where $\tau_{\rm T}$ is the Thompson optical depth, and $\langle T_{\rm e}\rangle$ and $\langle v_{||}\rangle$ are the electron density-weighted electron temperature and fluid velocity along the line of sight.

Because of the $n_{\rm e}$ weighting and the fact that the observed X-ray clusters have monotonically decreasing temperature profiles (Markevitch *et al.* 1998), we expect the thermal SZ effect to be highest in the core. Figures 2a and 2b, where we present images of the y-parameter for our simulated cluster on two spatial scales, confirm this expectation. The isocontours of y are smooth, concentric, and nearly circular, consistent with recent radio interferometric observations (Carlstrom *et al.* 1999). The peak value of $y \approx 10^{-4}$ is also consistent with observed values (Carlstrom *et al.* 1999), although our result is naturally sensitive to our assumed Ω_b.

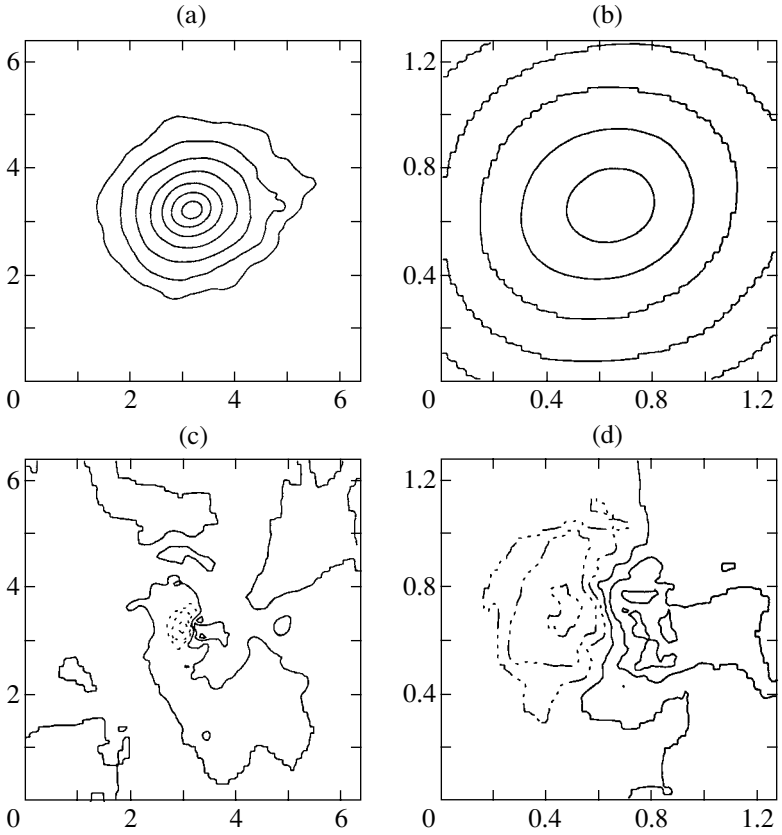

Fig. 2. Top: the SZ thermal y-parameter for a region 6.4 Mpc (left) and 1.2 Mpc (right) on a side. Bottom: the SZ kinematic effect, in terms of $\Delta T/T$. The y contours are logarithmically spaced: (1, 2, 4, 8, 16, 32 and 64) $\times 10^{-6}$ for the large (6.4 Mpc) region and (4, 8, 16, 32 and 64) $\times 10^{-6}$ for the small (1.2 Mpc) region. The kinematic contours are $(-4, -2, 1, 0, 1, 2, 4) \times 10^{-6}$, and the negative contours are dotted.

Since $v_\parallel$ is a signed quantity, the magnitude of the kinematic SZ effect will depend not only on the strength of turbulent or bulk motions in the cluster core, but also on the number of velocity reversals along the line of sight. Images of the kinematic SZ effect on two spatial scales are shown in Figs. 2c and 2d, obtained by integrating equation (2) along multiple lines-of-sight through the simulated cluster. One sees a reversal in $\Delta T/T$, due to the aforementioned circulation in the cluster core. Across the center of the cluster, $\Delta T/T$ changes abruptly from -4 to $+4$ $\times 10^{-6}$, or about 2% the magnitude of the thermal effect. Let us check this result for consistency. From equation (3), setting $k\langle T_e\rangle = 4.8$ keV (the mass weighted temperature inside r_{vir}), we deduce $\langle v_\parallel\rangle = 56$ km s^{-1}, about a quarter of the one-dimensional gas velocity dispersion in the core. In addition to the dominant effect due to core circulation, we can see cluster-wide fluctuations in the kinematic SZ effect image due to turbulent motions in the ICM, as well as due to a subcluster falling in at 3 o'clock in Fig. 3c. These fluctuations are at an amplitude of $\Delta T/T \approx 10^{-6}$.

The kinematic SZ effect due to cluster turbulence is just below current limits of detectability. Subtraction of background radio galaxies, which are not resolvable by the BIMA and OVRO interferometers used for the current observations, introduce a systematic uncertainty of 15–25 μK (Cooray *et al.* 1999) in the SZ decrement, versus our peak signal of ~ 11 μK. Better point source subtraction using future arrays with higher spatial resolution and visibility coverage should allow us to detect the kinematic effect due to cluster mergers, turbulence and bulk flows in the ICM.

Doppler Broadening and Shifting of Metal Emission Lines

The radial component of the thermal velocity of iron ions is $\sim$130 km s^{-1} for 5 keV temperature. Radial turbulent velocities decrease from $\sim$500 km s^{-1} at the virial radius to $\sim$250 km s^{-1} in the core (Fig. 1).

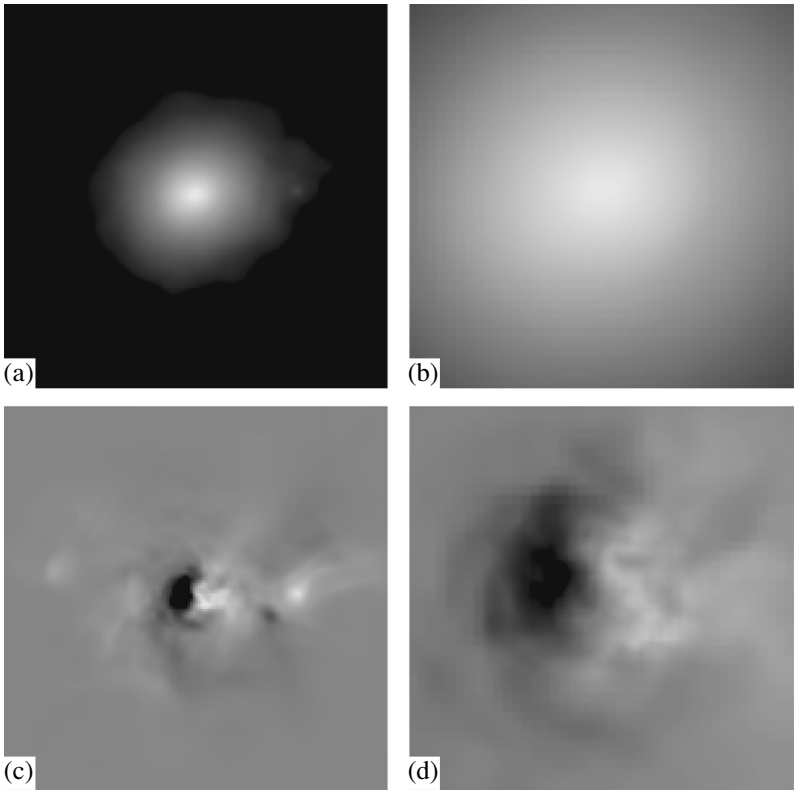

Fig. 3. Same as previous figure, but an image representation. The y-parameter is log-scaled from 10^{-6} to 10^{-4} (a, b), and the kinematic $\Delta T/T$ goes from -2 to $+2 \times 10^{-6}$ on for the large (c) image and -4 to $+4 \times 10^{-6}$ for the small image (1.2 Mpc) (d).

In addition, we have radial infall of gas and subclusters beyond the virial radius with $|v_r| > 1000$ km s^{-1}, and an ordered circulation with $v \sim 400$ km s^{-1} in the core. Thus, we might expect to see in a high resolution X-ray spectrum multiple components in iron emission lines with Doppler shifts of magnitude ΔE 2–6 times the thermal width, or $\pm$6–18 eV. We examine this possibility quantitatively in Fig. 4.

To isolate the effects of gas motions on X-ray line spectra, we plot the distribution of emission for an infinitely thin line with intensity proportional to $n_e^2 f(T_e)$, versus radial velocity relative to the cluster rest frame (top axis) or energy (bottom axis) for nine lines-of-sight through the simulated cluster. The line emissivity is assumed to be proportional to $n_e^2 f(T_e)$. In Fig. 4 we set $f(T_e) = 1$ for simplicity; below, we construct more realistic spectra. Each l.o.s. is normalized to the total amount of flux in the line, and that normalization (relative to the line through the cluster center) is shown in the upper right-hand corner.

In the absence of bulk motions and turbulence, the plot should show delta function emission at $\Delta E = 0$. Instead, we see multiple components spread over the range of energies estimated above. The asymmetric profiles seen at the negative impact parameters are the result of a large sub-clump falling into the cluster at high speed. The profiles at impact parameters $b \gtrsim 0$ show a roughly symmetric plateau of components over the range $\pm$15 eV, with the exception of a strong peak at $b = 0$, $\Delta E = -5$ eV caused by fluid circulation in the core. These components will be observable with order 1 eV spectral resolution, although we point out that each l.o.s. is pencil-thin, and that a real observation will be the (flux-weighted) average of many of these. The net result will be a much broader line with large sub-clumps moving at high speed showing up more clearly.

We now investigate what a realistic spectrum would look like, including the effects of thermal broadening, Doppler broadening and shifting due to fluid motions, and temperature effects along the l.o.s. Fig. 5 shows the 6.702 keV iron line as predicted by a Raymond-Smith code. We assume a constant iron abundance. The lines-of-sight are identical to Fig. 4. The dashed line shows the effect of thermal broadening only, while the solid line shows the full effect of thermal plus bulk motions. The emission is not normalized in this plot, as can be seen from the different scales at left. The absolute scale is arbitrary, as we have not defined the cross-section of the line of sight.

Again, the infalling sub-cluster is visible as a shifted maximum, particularly in the $b = -0.3$ plot.

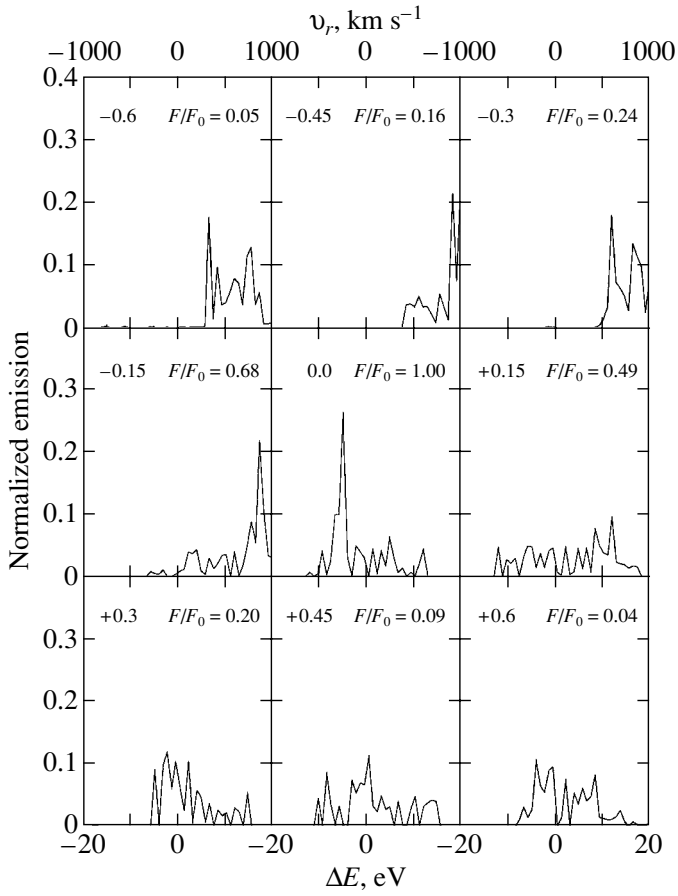

Fig. 4. The normalized X-ray emission versus Doppler shift in eV along nine lines of sight through the simulated X-ray cluster. The corresponding radial velocities are given at the top of the plot. The impact parameter in Mpc for each l.o.s. is given at upper left in each panel. The flux F in units of the central flux F_0 is given at upper right in each panel.

At $b = 0$ and +0.15, the spectrum is turbulently broadened to several times its thermal width. Discrete subcomponents are still visible. Finally, the second peak seen at 6.685 keV is actually another iron line (in fact there are a whole series at lower energy, but this is clearly the strongest). The energy resolution in this plot is much higher than that of any planned mission, but it is evident that 5 eV resolution (such as that planned for ASTRO-E2) would be enough to see these nonthermal features.

DISCUSSION AND CONCLUSIONS

The preceding results suggest that X-ray spectroscopy is the most promising approach in the near term to detect bulk motions and turbulence in X-ray clusters. Therefore, we focus our discussion on these possibilities.

Our hydrodynamic calculations show that the dynamics of cluster formation in a CDM-dominated model produce cluster-wide turbulence and ordered bulk flows in the ICM which are strong enough to be detected in the cluster core in high resolution X-ray spectra. Due to the small thermal broadening of emission lines from heavy elements, these are the most promising probes. We have calculated a synthetic spectrum of the well-separated 6.702 keV emission line of iron which shows strong turbulent broadening and shifting of the line into multiple components over a range $\Delta E \sim \pm 15$ eV. How reliable is this result? Our finite numerical resolution in the core ($\sim$15 kpc) artificially cuts off the turbulent spectrum at this scale. Thus, our simulation underestimates turbulent broadening due to microturbulence which could possibly eliminate discrete, Doppler shifted components. However, we have seen that some components are caused by ordered motions in the core, as well as by infalling sub-clusters, and our resolution is adequate to predict these features with some confidence. A second effect not included in our synthetic spectrum is finite angular resolution, which would average over the components and make the spectra more featureless. Thus, we expect X-ray spectra with a resolution of a few eV will see metal

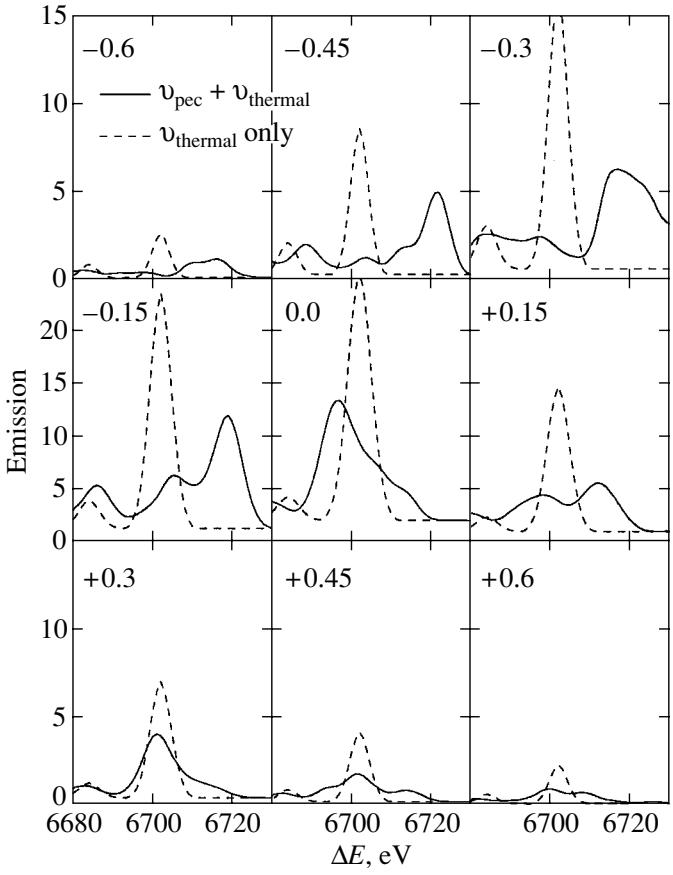

Fig. 5. Synthetic Fe line spectra along nine lines of sight through the simulated X-ray cluster. The dashed lines are computed assuming thermal broadening only, whereas the solid lines include both thermal broadening and Doppler shift.

lines whose widths are dominated by turbulent broadening, with possibly a few components reflecting bulk motions in the core. This implies that temperature measurements from line widths will be difficult or impossible, as they will be dominated by turbulent broadening. Figure 5 demonstrates that this is true, not only in the center, but out to several core radii. However, since the turbulent velocity scales with the virial velocity of the cluster, the line widths will probe the depth of the potential well.

Our predictions are based on a numerical simulation which makes a number of simplifying physical assumptions about the thermal and dynamic properties of the gas which may not reflect conditions in real X-ray clusters. For example, we ignore radiative cooling, which is important in the majority of real X-ray clusters at low redshift. In the simplest models, radiative cooling in dense cluster cores leads to centrally directed cooling flows and lower central temperatures. There is some observational support for these models (Fabian 1994). However, the velocity and temperature structure in the center of a cooling flow cluster is likely to be considerably more complicated, especially if the medium is turbulent or recovering from a recent merger. It is clear from our results that high angular and spectral resolution X-ray spectroscopy will be a powerful tool to probe the physical nature of cooling flow clusters. We can imagine that turbulence provides the perturbations which, when amplified by thermal instability, yield a two-phase medium in cooling flows. Lines of S and Ar would be brighter in the cooler gas. Mapping the cluster in these lines would be very revealing. We also assume the electron and ion temperatures are in LTE. Recently, Chieze *et al.* (1998) have shown via 3D simulations that this is a poor assumption near the virial radius. Since the line emissivity is sensitive to the electron temperature, while the line widths in the absence of turbulent broadening are a function of the ion temperature, one could *in principle* determine both with sufficiently accurate observations. However, the low emission measure and high level of turbulence we find at large radii would make this measurement difficult, if not impossible.

ACKNOWLEDGMENTS

Dr. Norman would like to thank Simon White at the Max-Planck-Institut für Astrophysik, where

this work was done, for his gracious hospitality and the Alexander von Humboldt Foundation for financial support during my stay. The numerical simulations were carried out on the SGI/CRAY Origin2000 system at the National Center for Supercompting Applications, University of Illinois at Urbana-Champaign.

The project was supported in part by the NSF grant AST-9803137, the NASA grant NAGW-3152, and the grant from the President of Russia NSh-2083.2003.2.

REFERENCES

1. T. C. Beers, K. Flynn, and K. Gebhardt, Astron. J. **100**, 32 (1990).
2. G. L. Bryan, M. L. Norman, J. M. Stone, *et al.*, Comput. Phys. Commun. **89**, 149 (1995).
3. G. L. Bryan and M. L. Norman, *Computational Astrophysics. 12th Kingston Meeting on Theoretical Astrophysics,* Ed. by D. Clarke and M. West, ASP Conference Series **123**, 363 (1997).
4. G. L. Bryan and M. L. Norman, Astrophys. J. **495**, 80 (1998).
5. D. A. Buote and J. C. Tsai, Astrophys. J. **452**, 522 (1995).
6. S. D. M. White, U. G. Briel, and J. P. Henry, Mon. Not. R. Astron. Soc. **261**, L8 (1993).
7. M. J. Geller and T. C. Beers, Publ. Astron. Soc. Pac. **94**, 421 (1982).
8. C. Jones and W. Forman, *Clusters and Superclusters of Galaxies,* Ed. by A. C. Fabian (Kluwer, Dordrecht, 1992), NATO Adv. Sci. Inst. Ser. C **366**, 49 (1992).
9. A. Dressler and S. A. Schectman, Astron. J. **95**, 985 (1988).
10. J. E. Carlstrom, J. J. Mohr, E. D. Reese, *et al.*, Bull. Am. Astron. Soc. **194**, 5801 (1999).
11. A. R. Cooray, J. E. Carlstrom, L. Grego, *et al.*, *After the Dark Ages: When Galaxies were Young (the Universe at* $2 < z < 5$*),* Ed. by S. Holt and E. Smith (AIP, Washington, 1999), p. 184.
12. H. M. P. Couchman, Astrophys. J. **368**, L23 (1991).
13. C. Loken, M. L. Norman, E. Nelson, *et al.*, Astrophys. J. **579**, 571 (2002).
14. M. Markevitch, K. Yamashita, A. Furuzawa, and Y. Tawara, Astrophys. J. Lett. **436**, L71 (1994).
15. M. Markevitch, W. R. Forman, C. L. Sarazin, and A. Vikhlinin, Astrophys. J. **503**, 77 (1998).
16. J. J. Mohr, D. G. Fabricant, and M. J. Geller, Astrophys. J. **413**, 492 (1993).
17. J. F. Navarro, C. S. Frenk, and S. D. M. White, Mon. Not. R. Astron. Soc. **275**, 720 (1995).
18. M. L. Norman and G. L. Bryan, *The Radio Galaxy Messier 87,* Ed. by H.-J. Roeser and K. Meisenheimer (Springer, Heidelberg, 1999a), Lect. Notes Phys., No. 530, 106 (1999a).
19. M. L. Norman and G. L. Bryan, *Numerical Astrophysics 1998,* Ed. by S. Miyama and K. Tomisaka (Kluwer, Boston, 1999b), Astrophys. Space Sci. Lib. **240**, 19 (1999b).
20. J. Pinkney, K. Roettiger, J. O. Burns, and C. M. Bird, Astrophys. J., Suppl. Ser. **104**, 1 (1996).
21. K. Roettiger, J. O. Burns, and C. Loken, Astrophys. J. **473**, 651 (1996).
22. R. A. Sunyaev and Ya. B. Zeldovich, Astrophys. Space Sci. **7**, 3 (1970).
23. R. A. Sunyaev and Ya. B. Zeldovich, Ann. Rev. Astron. Astrophys. **18**, 537 (1980).
24. R. A. Sunyaev and E. M. Churazov, Pis'ma Astron. Zh. **10**, 483 (1984) [Sov. Astron. Lett. **10**, 201 (1984)].
25. L. Tao, Mon. Not. R. Astron. Soc. **275**, 965 (1995).
26. A. C. Fabian, Ann. Rev. Astron. Astrophys. **32**, 277 (1994).
27. C. S. Frenk, S. D. M. White, P. Bode, *et al.*, Astrophys. J. **525**, 554 (1999).
28. J.-P. Chieze, J.-M. Alimi, and R. Teyssier, Astrophys. J. **495**, 630 (1998).
29. G. Efstathiou, J. R. Bond, and S. D. M. White, Mon. Not. R. Astron. Soc. **258**, 1 (1992).

Translated by S. Grebnev

Astronomy Letters, Vol. 29, No. 12, 2003, pp. 791–824. Translated from Pis'ma v Astronomicheskiĭ Zhurnal, Vol. 29, No. 12, 2003, pp. 892–926.

Turbulence in Clusters of Galaxies and X-ray Line Profiles

N. A. Inogamov[1, 2*] and R. A. Sunyaev[2, 3]

[1] *Landau Institute for Theoretical Physics, Russian Academy of Sciences, Chernogolovka, Russia*

[2] *Max-Planck-Institut für Astrophysik, Karl-Schwarzschild-Strasse 1, 85748 Garching, Germany*

[3] *Space Research Institute, Russian Academy of Sciences, Profsoyuznaya ul. 84/32, Moscow, 117810 Russia*

Received June 20, 2003

Abstract—Large-scale bulk motions and hydrodynamic turbulence in the intergalactic gas that fills clusters of galaxies significantly broaden X-ray emission lines. For lines of heavy ions (primarily helium-like and hydrogen-like iron ions), the hydrodynamic broadening is appreciably larger than the thermal broadening. Since clusters of galaxies have a negligible optical depth for resonant scattering in the forbidden and intercombination lines of these ions, these lines are not additionally broadened. At the same time, they are very intense, which allows deviations of the spectrum from the Gaussian spectrum in the line wings to be investigated. The line shape proves to be an important indicator of bulk hydrodynamic processes. Doppler probing of turbulence becomes possible, because the cryogenic detectors of the X-ray observatories now ready for launch and being planned will have a high energy resolution (from 5 eV for ASTRO-E2 to 1–2 eV for *Constellation-X* and XEUS). We use the spectral representation of a Kolmogorov cascade in the inertial range to calculate the characteristic shapes of radiation lines. Significant deviations in the line profiles from the Gaussian profile (shape asymmetry, additional peaks, sharp breaks in the exponential tails) are expected for large-scale turbulence. The kinematic SZ effect and the X-ray line profiles carry different information about the hydrodynamic velocity distribution in clusters of galaxies and complement each other, allowing the redshift, the peculiar velocity of the cluster, and the bulk velocity dispersion to be separated. © *2003 MAIK "Nauka/Interperiodica"*.

Key words: *turbulence, clusters of galaxies, intergalactic gas, X-ray line spectroscopy.*

1. THE OVERALL PICTURE

The hot intergalactic gas in clusters of galaxies forms an extended atmosphere in the gravitational potential well produced by the distribution of weakly interacting dark matter, whose mass exceeds the intergalactic gas mass by a factor of about 6. The cluster gas temperature reaches 2–10 keV. The speed of sound in this gas is 1000–1500 km s^{-1}. Galaxies move through the cluster gas with subsonic, sonic, and supersonic velocities. In energy terms, the presence of galaxies is of little importance, since the total mass of the galaxies is appreciably smaller than the total cluster mass. The intergalactic gas consists of completely ionized hydrogen together with ~25% (by mass) of helium. Heavy elements, including iron, are represented at a 30–40% level of their solar abundance.

Because of the growth of large-scale cosmological density perturbations, clusters of galaxies sometimes merge together and capture surrounding galaxies and groups of galaxies. During their merger, the colliding components move with supersonic or transonic velocities. Each merger is accompanied by shock formation and violent motion-generating turbulence on smaller scales. The characteristic time between mergers is long. The effects of no more than one to three large mergers appear to be observed simultaneously; a large merger is the merging of clusters with comparable masses. The capture of low-mass companions or individual galaxies gives a smaller contribution to the generation of turbulence.

It follows from N-body simulations with cold dark matter and gas that the turbulent pressure can account for up to 15% of the thermal pressure of the intergalactic gas in relaxed clusters of galaxies. This value implies very high turbulent pulsation velocities (up to 40% of the speed of sound). Remarkably, the calculations by different groups yield similar results (the methods, codes, and results were carefully compared by Frenk *et al.* 1999; see also Norman and Bryan 1999).

The activity of accreting supermassive black holes in the dominating cluster galaxy can trigger additional small-scale turbulence through collimated high-velocity mass outflows and jet acceleration (Churazov *et al.* 2001, 2002).

* E-mail: nail@landau.ac.ru

1063-7737/03/2912-0791$24.00

1.1. X-ray Line Profiles

The ISAS and NASA are planning to launch the ASTRO-E2 satellite in 2005.[1] This satellite will be equipped with cryogenically cooled X-ray bolometers. They will be placed in the focal planes of grazing-incidence telescopes. The expected energy resolution is $\sim$5 eV (FWHM) in the photon energy range from 0.5 to 10 keV, which includes the line of the helium-like iron ion (the iron ion with two electrons) at an energy of 6.7 keV. Since we compare the line profiles with Gaussian fits below, it is important to note (Porter and Mitsuda 2003) that this resolution corresponds to a dispersion of 2.7 eV. The prospective Constellation-X[2] and XEUS[3] missions will have X-ray detectors with an energy resolution as high as 1–2 eV. Therefore, it will become possible to detect line shifts and broadenings in rich clusters of galaxies that correspond to turbulent velocities $\sim 3\times 10^{-4}$ of the speed of light, i.e., up to 100 km s^{-1} or less than 10% of the speed of sound.

During turbulent pulsations, iron ions move in a mixture with hydrogen and helium nuclei. Accordingly, all ions have the same hydrodynamic velocities. The thermal velocities of ions of different types with the same temperature differ greatly because of the large difference between the nuclear masses. Therefore, the Doppler turbulent broadening of iron lines $\Delta E/E \sim v_{\rm turb}/c$ can significantly exceed their thermal broadening. The thermal velocity of iron ions is $\sim\sqrt{m_p/m_{\rm Fe}} = 1/\sqrt{56} = 13\%$ of the speed of sound, where m_p and $m_{\rm Fe}$ are the masses of the proton and the iron atomic nucleus, respectively. The amplitude of the turbulent velocity pulsations produced by a cluster merger can exceed the thermal velocities of iron ions severalfold. Thus, iron ions become effective tracers of turbulent velocity fields in the cluster interiors.

Let us introduce the parameter

$$\mathrm{Ma}_i = \frac{u_{\rm rms}}{\sqrt{kT/m_i}} = \sqrt{2}\frac{\Delta\nu_{\rm DH}}{\Delta\nu_{\rm DT}}$$
$$= 4.2\frac{u_{\rm rms}}{300[\mathrm{km\ s^{-1}}]}\sqrt{\frac{3[keV]}{kT}}\sqrt{\frac{m_i}{56m_p}}, \qquad (1.1)$$

which characterizes the ratio of the turbulent ($v_{\rm turb}\sim u_{\rm rms}$) and thermal velocity scales for an ion of mass m_i. It resembles the Mach number $\mathrm{Ma} = u_{\rm rms}/c_{\rm s}$ (the ionic Mach number), where $c_{\rm s}$ is the speed of sound. Parameter (1.1) defines the ratio of the hydrodynamic ($\Delta\nu_{\rm DH}$) and thermal ($\Delta\nu_{\rm DT}$) Doppler broadenings:

$$\Delta\nu_{\rm DT} = \nu_0\frac{u_{\rm rms}}{c}, \quad \Delta\nu_{\rm DH} = \nu_0\frac{\sqrt{2kT/m_i}}{c}. \quad (1.2)$$

In (1.1) and (1.2), $u_{\rm rms}$ is the line-of-sight hydrodynamic velocity dispersion[4] and ν_0 is the frequency at the center of the line profile.

The most intense lines observed in the spectral range between 2 and 10 keV are those of helium- and hydrogen-like iron ions. The equivalent width of the most intense iron lines reaches 100–500 eV. At a thermal Doppler width of $\sim$3 eV, they must rise by tens and hundreds of times above the smooth continuum associated with hydrogen–helium plasma bremsstrahlung. XMM observations of the central part of the Perseus cluster of galaxies gave 10^5 photons in 40 ks in the complex of iron K-lines (Churazov *et al.* 2003). The Constellation-X and XEUS satellites will have an effective area that is tens of times larger than that of XMM, which will make it possible to study in detail the weak wings of X-ray lines.

The spectral surface brightness of a cluster in a line is given by the formula

$$I(\Delta E, y, z) = \int dx j[E_0, T_{\rm e}(x,y,z)]$$
$$\times\, n_{\rm e}(x,y,z)\frac{dn_i(x,y,z,\Delta E)}{d(\Delta E)},$$

where I is measured in photons cm^{-2} s^{-1} eV^{-1}, the coefficient j characterizes the rate of production of excited ions[5] and the emission of photons with energy E_0 by these ions,[6] $n_{\rm e}$ is the electron density, and $dn_i/d(\Delta E)$ is the number of ions of a given type in the range of velocities that shift the line photons to the energy range from ΔE to $\Delta E + d(\Delta E)$. The energy $\Delta E = E - E_0$ is measured from the line center and is proportional (see below) to the line-of-sight ion velocity. The line-of-sight velocity of ions can be determined by taking into account their thermal and hydrodynamic velocities. We assume that the thermal velocity distribution of ions is Maxwellian, with an ion temperature equal to the electron temperature. The hydrodynamic velocity distribution can be calculated in terms of the turbulence model presented below. In the above formula, the natural line width

[1] http://www.isas.ac.jp/e/enterp/missions/astro-e2/
[2] http://constellation.gsfc.nasa.gov/docs/main.html
[3] http://astro.estec.esa.nl/SA-general/Projects/XEUS/

[4] The dispersion of the radial velocity component.
[5] Therefore, j depends on the electron temperature $T_{\rm e}$. Ions are excited in pair collisions of ions of a given type with electrons (electron impact excitation, a binary reaction). In an isothermal gas at a constant (in volume) elemental abundance, $n_{\rm e}n_i \propto n_{\rm e}^2$.
[6] In the frame of reference associated with the ion, the photon energy is E_0 (without Doppler and intrinsic broadenings).

is disregarded (see formulas (12.2)–(12.5) below). The surface brightness is determined by the emission contributions from individual regions.

In this paper, we consider qualitative effects, primarily the degree of deviation of the emission line profile from the Gaussian profile and the causes of such deviation. Therefore, for illustration, we investigate the simplest case of an isothermal cloud with constant density and elemental abundance over its volume. In this case, the above formula for the brightness I takes the form

$$I(\Delta E, y, z) = j(E_0, T_\mathrm{e}) n_\mathrm{e} \int dx \frac{dn_i(\Delta E)}{d(\Delta E)}$$
$$= \alpha j(E_0, T_\mathrm{e}) n_\mathrm{e}^2 \int dx \psi(x, y, z, \Delta E),$$

where α is the elemental abundance, and the function ψ specifies the local line-of-sight velocity distribution. We ignore the nonlinear density variations due to turbulent pulsations.

An efficient method for solving the problem of the iron line profile involves direct numerical simulation. The first attempt of this kind was made by Sunyaev *et al.* (2003). Below, we attempt to construct a relatively simple turbulence model (see formulas (4.1) and (11.1) below) to understand in which cases *the shape of a turbulently broadened line can differ from the Gaussian shape expected from the central limit theorem of probability theory*. The model is based on the assumption about a Kolmogorov cascade in the inertial range limited by the mixer size L_mix and the viscous scale L_ν. The number of mixers in the large-scale case ($L_\mathrm{mix} \sim L$) is limited. As a result, the line spectrum significantly deviates from the Gaussian spectrum.[7]

Figure 1 shows the characteristic profile of the helium-like iron (Fe XXV) permitted w-line (curve *4*) obtained in the adopted model. As we see (cf. curves *2* and *4*), there are qualitative deviations from the commonly assumed Gaussian line profile

$$\frac{1}{\sqrt{2\pi}} \frac{1}{\sqrt{u_\mathrm{rms}^2 + kT/m_i}} \exp\left(-\frac{1}{2}\frac{u^2}{u_\mathrm{rms}^2 + kT/m_i}\right)$$
$$= \frac{1}{\sqrt{2\pi}} \frac{1}{\sqrt{1 + \mathrm{Ma}_i^{-2}}} \frac{1}{u_\mathrm{rms}} \exp\left(-\frac{1}{2}\frac{\hat{u}^2}{1 + \mathrm{Ma}_i^{-2}}\right)$$

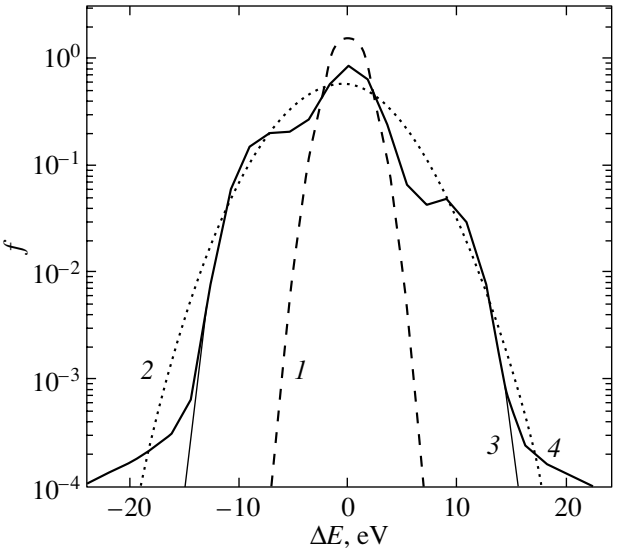

Fig. 1. Fe XXV w-line spectrum (*4*) at $kT = 3$ keV; *1*—the thermally broadened line profile (without hydrodynamic broadening), *2*—the Gaussian profile with a total (hydrodynamic plus thermal) dispersion $u_{HT} = 190$ km s^{-1} (see the table), and *3*—the line profile without Lorentz broadening.

with a dispersion the square of which is equal to the sum of the squares of the thermal and hydrodynamic dispersions (curve *2*). In what follows,

$$\hat{u} = u/u_\mathrm{rms}, \qquad (1.3)$$
$$\Delta E[\mathrm{eV}] = -6.7[\mathrm{eV}](u_\mathrm{rms}/300[\mathrm{km\ s^{-1}}])\hat{u},$$

$\hat{u}$ is a dimensionless velocity (in units of dispersion), and ΔE is the deviation from the profile center. Formula (1.3) is used to recalculate $\hat{u}$ to ΔE. Parabola *1* in Fig. 1 corresponds to the Maxwellian distribution of ions $f_\mathrm{T}(\hat{u}) = (\mathrm{Ma}_i/\sqrt{2\pi})\exp(-\mathrm{Ma}_i^2\hat{u}^2/2)$ (purely thermal broadening). All distributions were normalized to unity: $\int_{-\infty}^{\infty} f(\hat{u})d\hat{u} = 1$. Curves *3*, $f_\mathrm{HT}(\hat{u})$, and *4*, $f_\mathrm{HTL}(\hat{u})$, represent the turbulent line profiles. The distribution $f_\mathrm{HT}(\hat{u})$ includes hydrodynamic (H) and thermal (T) broadenings, while the distribution $f_\mathrm{HTL}(\hat{u})$ includes hydrodynamic, thermal, and Lorentz (L) broadenings. The intrinsic or Lorentz broadening was calculated[8] for the Fe XXV w-line.

Figure 2a shows, first, the thermal Gaussians of the helium-like iron w-line (dashed curves, narrow parabolas), second, the computed spectra (fluctuating solid curves), and, third, the Gaussian fits to the computed spectra (wide parabolas). These spectra were constructed for nine points of the cluster projection onto the plane of the sky. The Gaussian fits are specified by two parameters (shift and broadening)

[7] The influence of the number of mixers on the deviation from the Gaussian distribution is discussed below in Sections 7 (see Table 2), 10, and 11.3. For $L_\mathrm{mix} \sim L$, large-scale motions appreciably shift the line center (see Fig. 2, Table 1, and Figs. 6 and 7). The presence of a Kolmogorov tail per se at small scales does not imply that the velocity distribution will be Gaussian.

[8] Lorentz broadening is considered in Sections 12 and 13.

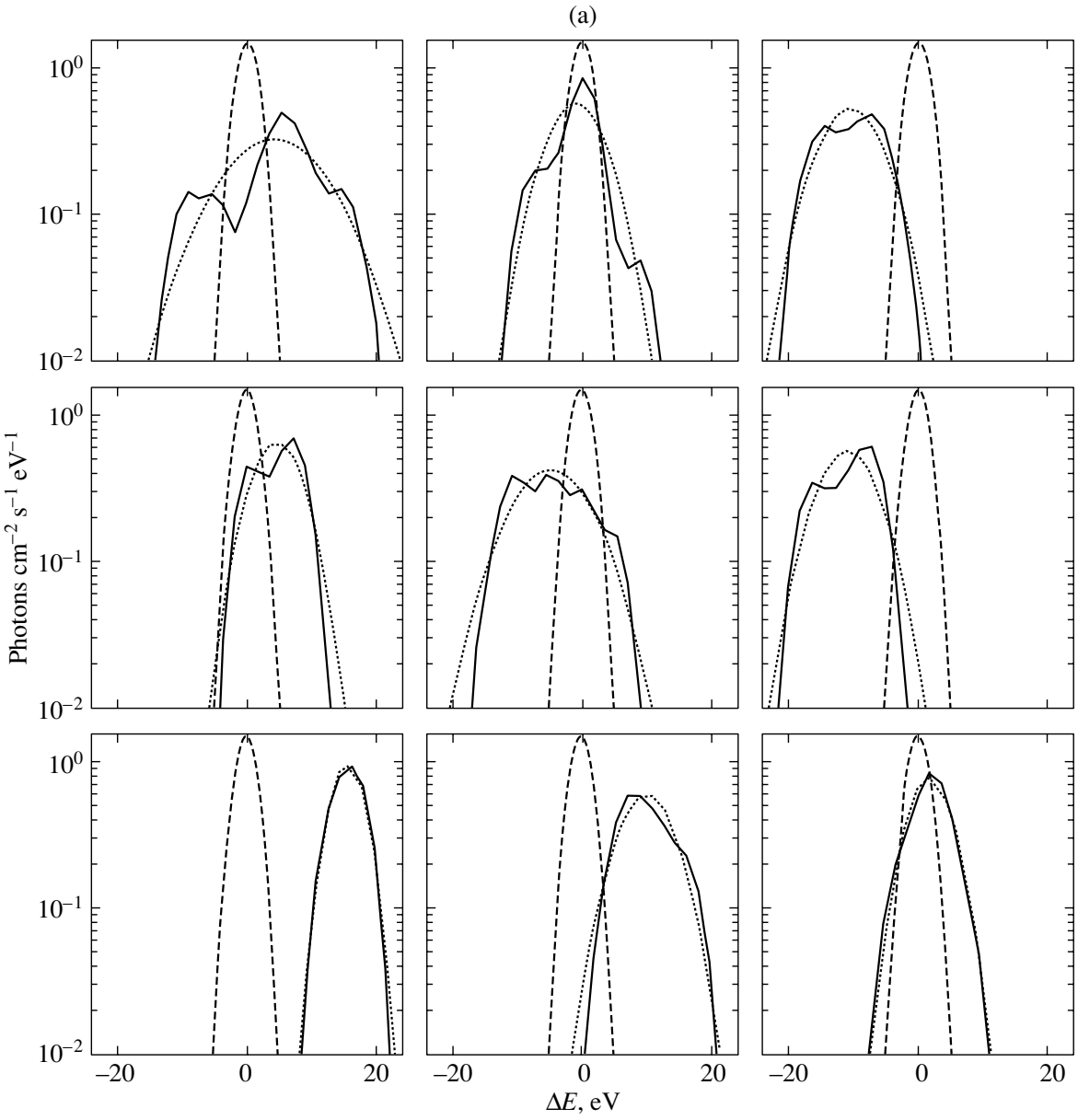

Fig. 2. (a) Helium-like iron line profiles at nine points in the image of a cluster with $kT = 3$ keV. The dashed curves (narrow parabolas) specify the thermal line broadening, and the solid curves take into account the lines shift and broadening through hydrodynamic and thermal motions (fluctuating curves, computed spectra). The hydrodynamic and thermal velocity dispersions and the velocity corresponding to the shift of the line profile centroid are given in Table 1 for each of the nine lines. The dotted curves represent the Gaussian fits to the computed spectra. (b, c) Spectra for the complexes of iron lines near 6.7 keV at $kT_e = 3$ (b) and near 6.9 keV at $kT_e = 8$ keV (c). The dashed curves specify the thermal line broadening. The lines were normalized to the most intense permitted helium-like iron w-line. (d, e, f) Spectra for the complex of iron lines near 6.7 keV at $kT_e = 3$ keV were obtained by folding with the profiles shown in the upper middle, central, and lower left panels of Fig. 2a, respectively. The dashed curves again specify the spectrum for the thermally broadened lines of the complex. All curves were normalized to the same total number of photons in the complex of lines. (g) An approximate spectrum for the complex of iron lines near 6.7 keV from the cluster as a whole obtained by folding the profile in Fig. 2h with the spectrum in Fig. 2b. (h) The iron line profile (curve *3*) at $E_0 = 6.7$ keV obtained by adding the nine profiles shown in Fig. 2a. This profile was also normalized to the total number of photons. To a first approximation, this profile corresponds to the line profile observed from the entire cluster. The thermal broadening (curve *1*) and the Gaussian curves for the total broadening in the entire cluster (total dispersion 460 km s^{-1}, curve *4*) and for dispersion $u_{rms} = 270$ km s^{-1} (curve *2*) corresponding to the central panel in Fig. 2a are shown for comparison.

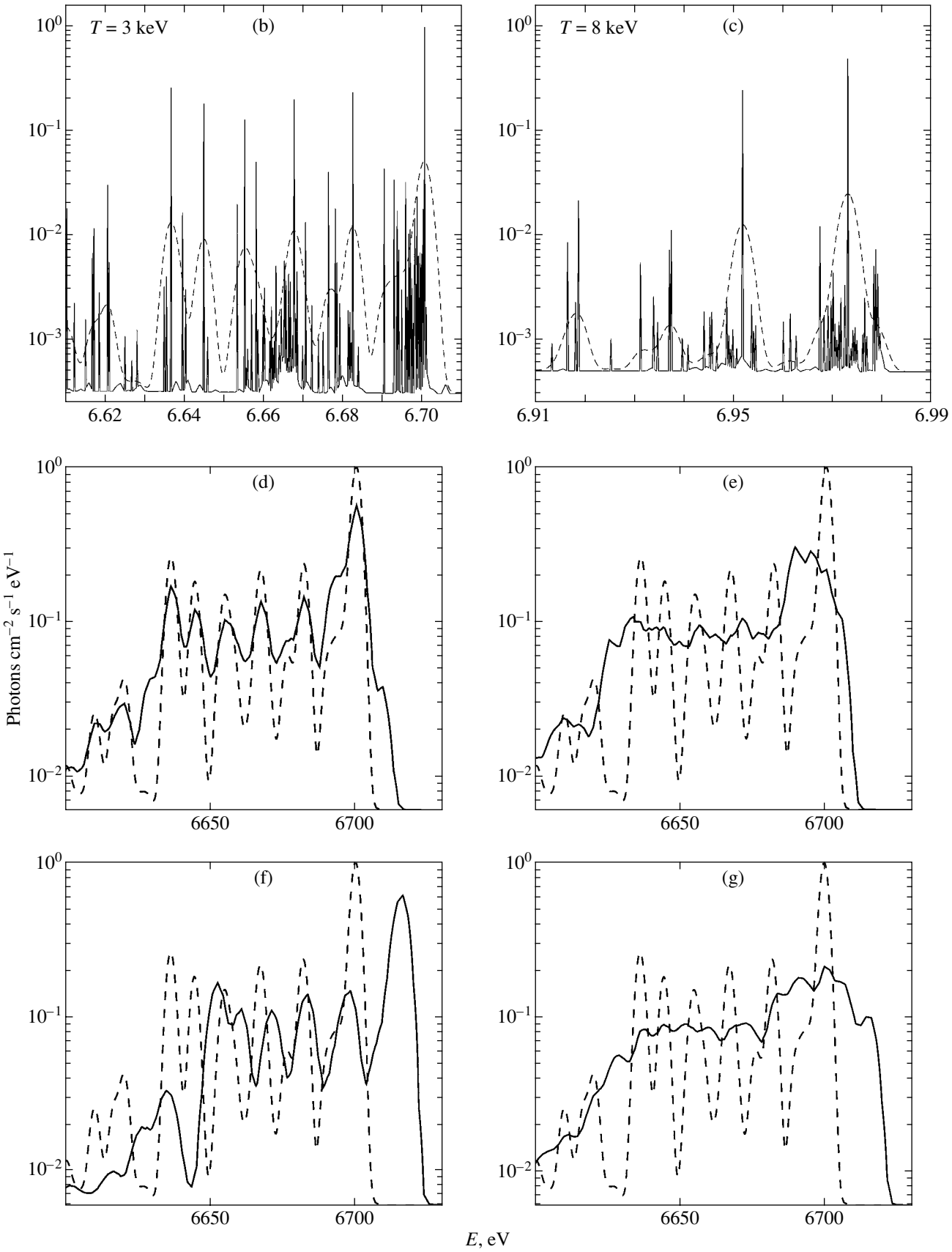

Fig. 2. (Contd.)

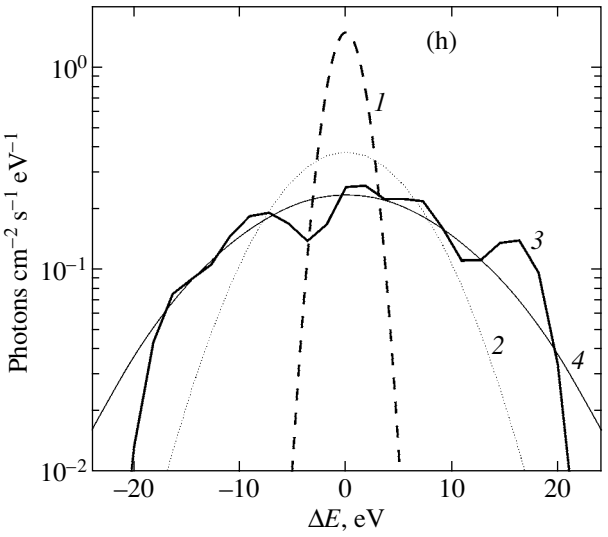

Fig. 2. (Contd.)

that can be determined from the computed spectrum (see Table 1). These nine points correspond to the center, vertices, and middles of the square in the plane of the sky described in Sections 1.2, 1.3, and 11. Note that curve *3* in Fig. 1 corresponds to the line profile shown in the middle panel in the upper row of Fig. 2a.

Figure 2b shows the radiation spectrum for a hot plasma with a temperature of 3 keV and a normal chemical abundance[9] in the energy range[10] near the permitted helium-like iron line at ≈ 6.7 keV. The complex of iron lines near the hydrogen-like iron line ($E_0 \approx 6.9$ keV) is shown in Fig. 2c at $kT_e = 8$ keV. These plots show the individual lines without including their radiation widths in the form of narrow peaks with a width close to 10^{-2} eV. The plots were constructed by using the APEC code (Astrophysical Plasma Emission Code; Smith *et al.* 2001), which is part of the XSPEC V11.2 code. All lines were normalized to the most intense permitted w-line ($E_0 =$ 6.7005 keV). As an illustration, the dashed curves in Fig. 2b indicate the same spectra, broadened by the thermal motions of the ions.

Figures 2d–2f show the complex of lines near 6.7 keV with allowance made for both thermal and hydrodynamic motions. These spectra were computed by folding the profiles presented in the upper middle, central, and lower left panels of Fig. 2a with the complex of individual lines and satellites shown in Fig. 2b. The dashed curves again represent the broadening of the individual lines due to thermal ion motions in the absence of hydrodynamic motions.

[9]The abundance affects only the relative continuum intensity.

[10]The helium-like iron lines and their satellites are intense in this energy range.

The solid and dashed curves in Figs. 2d–2f were normalized to the same number of photons in the whole complex of lines.

The plasma emission is a function of the temperature. An increase in temperature affects both the relative line intensity and the thermal line width. At high temperatures (e.g., $kT = 8$ keV), the complex of hydrogen-like iron lines near energy 6.9 keV becomes intense (Fig. 2c).

The supersonic motion of the gas clouds in the process of merging leads to the formation of high-temperature shock waves. Fine X-ray spectroscopy allows one to separate the regions with temperatures well above the average due to their contribution to the radiation in the complex of hydrogen-like iron lines near 6.9 keV (see Fig. 2c). The 6.9 keV lines are much stronger at higher temperatures. Comparing the line profiles of helium-like iron (near 6.7 keV) and hydrogen-like iron (near 6.9 keV), we can distinguish the internal motion in the zone heated by shock waves from the motion in the colder gas.

Using Figs. 2b and 2c, we wish to emphasize the following. The most favorable energy range for observing hydrodynamic iron line broadening effects is to the right of the w-line center, because there are virtually no other intense lines at $kT = 3$–10 keV within several tens of eV of the center of this line. Thus, the far wings of the broadened line can be studied in detail.

Also of considerable interest is the iron z-line at photon energy $E_0 = 6.6366$ keV that corresponds to the transition from the 1s2s triplet to the ground state: $^3\mathrm{S} \rightarrow {}^1\mathrm{S}$. In this case, the left line wing is favorable for observations. In a detailed study, it will be possible to simulate the spectrum of the entire set of lines in both complexes and to compare it with the observed spectrum.

Figure 2f shows a very large shift of the line observed from the column in the lower left panel in Fig. 2a. All of this column is flying toward us. The velocity dispersion in it slightly exceeds the thermal velocity dispersion. In contrast, the upper right panel of Fig. 2a shows that the corresponding column is flying away from us with a slightly lower radial velocity and a larger velocity dispersion. Collectively, these two panels suggest the presence of a large-scale motion similar to the rotation of the entire cluster gas—this is a manifestation of a large-scale mixer, i.e., the last large merger.

In the central part of the cluster (Figs. 2a and 2e), the broadening and the shift are so large that the individual lines and satellites in the complex of lines are barely discernible.

Since the ASTRO-E2 spectrometers have a limited angular resolution, they will yield detailed images

only for the nearest rich clusters of galaxies. For distant clusters, the line profiles from the entire cluster will be investigated. Figures 2g and 2h give the first idea of this profile. A comparison of Fig. 2g with Figs. 2d–2f shows how informative the set of high-resolution spectroscopic data is even with a limited angular resolution. The profile in Fig. 2h was obtained by averaging the nine profiles presented in Fig. 2a with equal statistical weights. Recall that each of these nine profiles was obtained for a very narrow unit column in a cube with a volume of 160^3 mesh points. Clearly, the line profile from the entire cube must be even smoother. On the other hand, the shifts of the profiles shown in Fig. 2a and Table 1 suggest the presence of intense large-scale motions inside the cluster. In observations of the cluster as a whole, they give a large contribution to the dispersion but must leave traces in high-energy-resolution spectra. The profile in Fig. 2h is much broader than any of the nine profiles in Fig. 2a (see Table 1); in particular, it is broader than the profile in Fig. 1. This is the result of large-scale motions.

The spectrum in Fig. 2g was obtained by folding the profile in Fig. 2h with the complex of iron lines near 6.7 keV. We see individual spectral features, but their amplitude is appreciably smaller than that predicted in the model with thermal broadening and a smaller hydrodynamic velocity dispersion. The high-energy wing of the permitted helium-like iron w-line makes it possible to judge the total velocity dispersion in the cluster.

The turbulent broadening determined for all the nine profiles shown in Fig. 2a corresponds to a large (at least severalfold) decrease of the optical depth in the resonance w-line. This is why we disregard the broadening of this line due to resonant scattering (Gilfanov *et al.* 1987) in the plots of Fig. 2.

To elucidate the turbulence model, Fig. 3 shows a Kolmogorov spectrum of the Fourier velocity amplitudes u_n with a power-law scaling in the wavelength range $L_\nu < \lambda < L_{\rm mix} \le L$ and harmonic numbers $1 \le N_{\rm mix} < n < N_\nu$, where L is the cluster scale, $\lambda = \lambda_n = L/n$, $k = k_n = 2\pi/\lambda_n = 2\pi n/L$, $N_{\rm mix} = L/L_{\rm mix}$, $N_\nu = L/L_\nu$, and L_ν is the viscous damping scale. Note that the total number of energy-containing eddies in volume L^3 is $N_{\rm mix}^3$ Below, we show that the velocity dispersion and the hydrodynamic Doppler broadening (1.2) are determined by large-scale fluctuations with $\lambda \sim L_{\rm mix}$. The fractal line profile fluctuations, which are smoothed out by thermal broadening, are associated with the Kolmogorov small-scale tail.

When computing the realization shown in Figs. 1 and 2, we took $N_{\rm mix} = 1$ and $N_\nu = 40$. Because of the significant thermal broadening of the profile and the decrease in small-scale pulsation velocity amplitude with decreasing scale, the difference between the realizations for $N_\nu = 40$ and $N_\nu \gg 40$ is small (see Sections 8–10 for a discussion). The dependence on $N_{\rm mix}$ is discussed in detail in Sections 7 and 11.3.

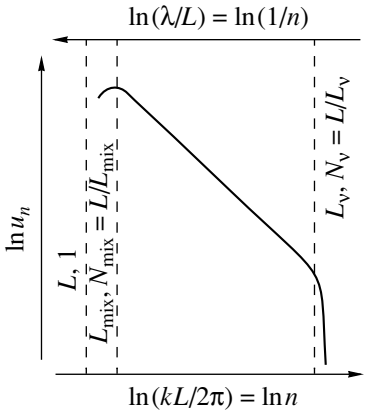

Fig. 3. The λ and k fluctuation spectrum in a Kolmogorov model. The scales $(L, 1)$, $(L_{\rm mix}, N_{\rm mix})$, and (L_ν, N_ν) characterize the cluster, the turbulence-maintaining mixers, and the viscous dissipation region, respectively.

We calculated the velocity field $u(x, y, z)$ in a cube $(2l)^3$ with an edge $2l$. The function $u(x, y, z)$ satisfies the periodic boundary conditions at the boundaries of the large cube L^3; see formula (11.1) in Section 11. In our calculations (Figs. 1 and 2, and 4–7), we took $L = 1$ and $2l = 0.4$. We chose $2l < L$ to reduce the influence of the periodic boundary conditions. The cube $(2l)^3$ was covered by a $3D$ mesh of 160^3 computational points. The separations between the mesh points are $\delta l = 2l/160$. Each column in Fig. 2a has a length $2l$ along the line of sight and a cross section in the plane of the sky in the form of a $\delta l \times \delta l$ square.

Table 1. Shifts and broadening of the X-ray line profile at $E_0 = 6.7$ keV

u_1, $u_{\rm HT}$	+180, 330	−39, 190	−450, 200
u_1, $u_{\rm HT}$	+205, 165	−205, 280	−470, 190
u_1, $u_{\rm HT}$	+695, 110	+440, 180	+80, 140
$u_{\rm HT}$		460	

Note: The positions of the cells in the table and the data in them correspond to the nine line-of-sight columns in Fig. 2a. The fourth row of the table gives the velocity dispersion for the cluster as a whole. This is the dispersion of the integrated spectrum in Fig. 2h. In what follows, u_1 is the shift of the line profile center in km s^{-1}, and u_{HT} is the dispersion of the computed distributions from Fig. 2a.

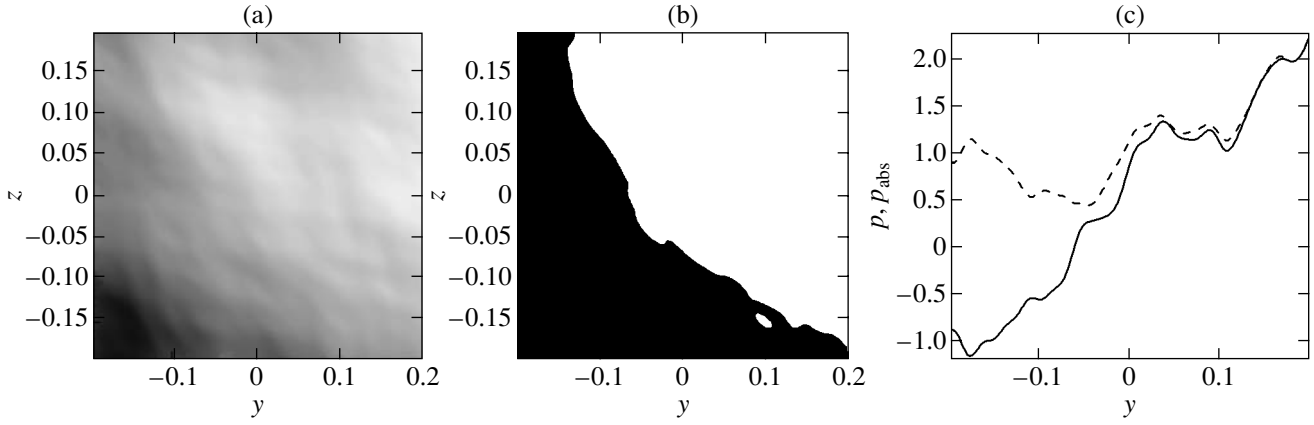

Fig. 4. Distribution of the CMB intensity fluctuations (1.4) in the y, z plane of the sky that follows from the Kolmogorov model. (a) A map of the line-of-sight momentum $p(y, z)$; $L = 1$. The white and black colors correspond to the motion away from and toward the observer, respectively. The shades of gray give the local values of $\Delta T_r(y, z)/T_r$. (b) The $\Delta(y, z)/T_r = 0$ isoline that separates the black and white regions with opposite signs of ΔT_r. (c) The $p(y, z = 0)$ cut (solid curve) of the $p(y, z)$ surface. The dashed line represents $p_{\rm abs}$ (1.6).

1.2. Turbulence and the Kinematic SZ *Effect*

The hydrodynamic velocity distribution of a cluster in the plane of the sky can also be analyzed by studying manifestations of the kinematic SZ effect (Sunyaev and Zeldovich 1980), i.e., by measuring the intensity fluctuations of the cosmic microwave background (CMB) within the cluster:

$$\frac{\Delta T_r(y,z)}{T_r} = \sigma_{\rm T} \int\limits_{-\infty}^{\infty} \frac{v_{||}(x,y,z)}{c} n_{\rm e}(x,y,z)dx. \quad (1.4)$$

Nagai *et al.* (2003) and Sunyaev *et al.* (2003) used this method of analysis in their numerical calculations. Formula (1.4) was first suggested by Sunyaev and Zeldovich (1970) to calculate the primordial Doppler CMB fluctuations and was used by Sunyaev (1977) in calculating the fluctuations due to secondary ionization. In formula (1.4), y and z are the coordinates in the plane of the sky; x is the coordinate along the line of sight; and $v_{||}$ is the component of the local hydrodynamic velocity vector along the line of sight (the x velocity component) denoted below by u, $\hat{v}_{||} = v_{||}/u_{\rm rms}$; and T_r is the CMB temperature. The $\Delta T_r/T_r$ fluctuations (1.4) differ only by one factor from the fluctuations in the dimensionless total momentum

$$p(y,z) = \int \hat{n}_{\rm e}\hat{v}_{||}(x,y,z)dx/(2l), \quad (1.5)$$

of the emitting matter along the x axis (the line-of-sight or column momentum), where $\hat{n}_{\rm e} = n_{\rm e}/(n_{\rm e})_{\rm centr}$, and $(n_{\rm e})_{\rm centr}$ is the central cluster density. Below, the density n_e is assumed to be roughly uniform over the cluster core.

Figures 4 and 5 show maps, reliefs, and cuts of the intensity fluctuations (1.4). The degree of blackening in Fig. 4a is proportional to the local $\Delta T_r(y, z)/T_r$ fluctuation amplitude and the local momentum $p(y, z)$. Figure 4b shows regions in the y, z plane of the sky that are moving[11] toward (black) and away from us (white). We performed our calculations by using the Kolmogorov model (for details, see the sections below). For long-wavelength turbulence with $N_{\rm mix} \sim 1$ (see Fig. 3), the size of the region with the same sign of p (1.5) is on the order of the cluster size L. In the typical realization shown in Figs. 1, 2, and 4–7, $N_{\rm mix} = 1$ and $N_\nu = 40$. Figure 4c shows the cut of the $p(y, z)$ surface (see Fig. 5) by the $z = 0$ plane that passes through the cluster center. The solid and dashed curves in this figure indicate, respectively, the functions $p(y, 0)$ (1.5) and

$$p_{\rm abs}(y,0) = \int\limits_{-l}^{l} \hat{n}_{\rm e}|\hat{u}(x,y,0)|dx/(2l). \quad (1.6)$$

In the case of a large scale ($N_{\rm mix} \sim 1$), the functions $|p(y, z)|$ (1.5) and $p_{\rm abs}(y, z)$ (1.6) are of the same order of magnitude, as illustrated by Fig. 4c.

The sizes of the identically signed spots (Fig. 4b) for the function $p(y, z)$ and the $|p|/p_{\rm abs}$ ratio are determined by the scale $L_{\rm mix} = L/N_{\rm mix}$. If there are many mixers ($N_{\rm mix} \gg 1$), then the function $p(y, z)$ changes sign during a displacement $\Delta l_\perp \sim L_{\rm mix}$ in the plane of the sky transverse to the line of sight. In this case,

[11] Here, we are dealing with the motion on average, because $p = \int \hat{n}_{\rm e}\hat{u}dx/L$.

$|p|/p_{\rm abs} \sim 1/\sqrt{N_{\rm mix}}$. In deriving these estimates,[12] we assume that (1) the separation between mixers is on the order of their size, (2) the fluctuation amplitude of the velocity $u_{\rm rms}$ on each mixer is of the same order of magnitude, and (3) the velocity correlation decays on a scale on the order of $L_{\rm mix}$. In this case, $p_{\rm abs} \sim 1$, because $\langle \hat{u} \rangle \sim 1$, $\langle 2l \rangle \sim 1$ (we set $\hat{n}_{\rm e} = 1$), and $|p| \sim N_{\rm mix}^{-1/2}$, because the total momentum $p(y,z)$ (1.5) along the x line of sight is the sum of the momenta of $N_{\rm mix}$ out-of-phase mixers.

It is interesting to calculate the Kolmogorov scaling law for the CMB fluctuations $\Delta T_r/T_r \propto p$ (1.4). This law determines the amplitude of the fractal "fringes" (small fluctuations or spots)[13] in the dependences $\Delta T_r(y,z)$ and $p(y,z)$ (see Figs. 4a, 4c, and 5). The velocity is known (see Sections 3 and 4) to be given by

$$\langle |\mathbf{v}(\mathbf{r}_2) - \mathbf{v}(\mathbf{r}_1)| \rangle = (\Delta v)_{\Delta l} \propto (\Delta l)^{1/3}, \qquad (1.7)$$
$$\Delta l = |\mathbf{r}_2 - \mathbf{r}_1|.$$

Let us show that the following law holds for the kinematic SZ effect:

$$\langle |\Delta T_r(\mathbf{r}_{\perp 2}) - \Delta T_r(\mathbf{r}_{\perp 1})| \rangle$$
$$= [\Delta(\Delta T)]_{\Delta l_\perp} \propto (\Delta p)_{\Delta l_\perp} \propto (\Delta l_\perp)^{5/6}, \qquad (1.8)$$
$$\Delta l_\perp = |\mathbf{r}_{\perp 2} - \mathbf{r}_{\perp 1}|,$$

where $\mathbf{r}_\perp = (y,z)$ is a two-dimensional vector in the plane of the sky. We restrict our analysis to the case $N_{\rm mix} \sim 1$ presented in Figs. 1, 2, and 4–7. Below, we give a brief derivation.[14] Let us consider two adjacent parallel x lines of sight separated by a distance $\Delta l_\perp$. The value of $(\Delta p)_{\Delta l_\perp}$ is equal to the difference between the momenta p (1.5) on these lines of sight. Let us calculate this difference. The contributions of large eddies with a size $l_{\rm rot}$ ($l_{\rm rot} > \Delta l_\perp$) to the difference between integrals (1.5) are small, because these contributions are almost equal on adjacent lines of sight. The contribution of small eddies ($l_{\rm rot} < \Delta l_\perp$) increases with size $l_{\rm rot}$ and reaches a maximum at $l_{\rm rot} \sim \Delta l_\perp$. Consequently, eddies with sizes on the order of the separation between the lines of sight should be considered to estimate (1.8).

These eddies are uncorrelated. Indeed, the correlation in the velocity field induced by them decays on a scale of $\sim \Delta l_\perp$. Therefore, the corresponding contribution to the difference $\Delta(\Delta T_r) \propto \Delta p$ is accumulated through a random addition. According to formulas (1.5) and (1.7), the momentum from a single eddy is $\sim u_{\rm rms}(\Delta l_\perp/L_{\rm mix})^{1/3}(\Delta l_\perp/L)/u_{\rm rms}$.

[12] Section 11.3 is devoted to the corresponding calculations.

[13] Small oscillations or fringes are formed by a random addition of many eddies with different scales; see the sections below.

[14] For a more detailed proof, see Section 11.

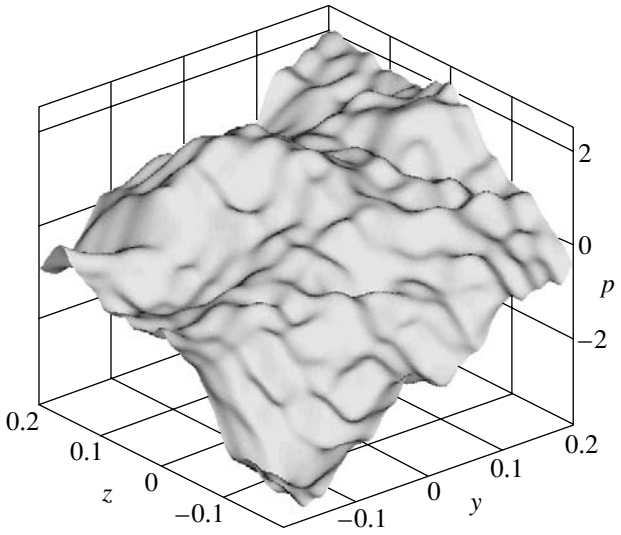

Fig. 5. Relief of the kinematic SZ effect. The height p of the point (y,z,p) on the $p(y,z)$ surface above the y, z plane is proportional to the fluctuation amplitude $\Delta T_r(y,z)/T_r$ (1.4).

There are $\sim L/\Delta l_\perp$ such eddies on a line of sight with a length $\sim L \sim L_{\rm mix}$. Expression (1.8) follows from this and from the fact that the effect is proportional to the square root of the number of small-scale eddies under consideration, because

$$(\Delta p)_{\Delta l_\perp} \sim (\Delta l_\perp/L_{\rm mix})^{1/3}(\Delta l_\perp/L)\sqrt{L/\Delta l_\perp}.$$

Scaling (1.8) is valid in the Kolmogorov range of scales $L_\nu < \Delta l_\perp < L_{\rm mix}$. In observations of $\Delta T_r/T_r \propto p$ or in direct numerical simulations, the small-scale limit is determined by the aperture resolution and the spatial mesh step, respectively.

1.3. Comparison of the Two Methods for Studying Turbulence

Let us compare the two effects under discussion, the Doppler broadening of X-ray lines and the kinematic SZ effect. The map of CMB intensity (1.4) carries information about the momentum of a unit column along the line of sight. This gives the velocity relative to the frame of reference associated with the CMB near the cluster,[15] i.e., its peculiar velocity. The X-ray line profiles are more informative. In the

[15] The velocity of the cluster as a whole can be determined by integrating the line profile over the plane of the sky within the cluster and finding its centroid. This operation will allow us to measure the sum of the cluster recession velocity due to the expansion of the Universe (redshift) and the line-of-sight peculiar cluster velocity in the frame of reference associated with the CMB. The kinematic SZ effect allows this peculiar velocity component to be determined.

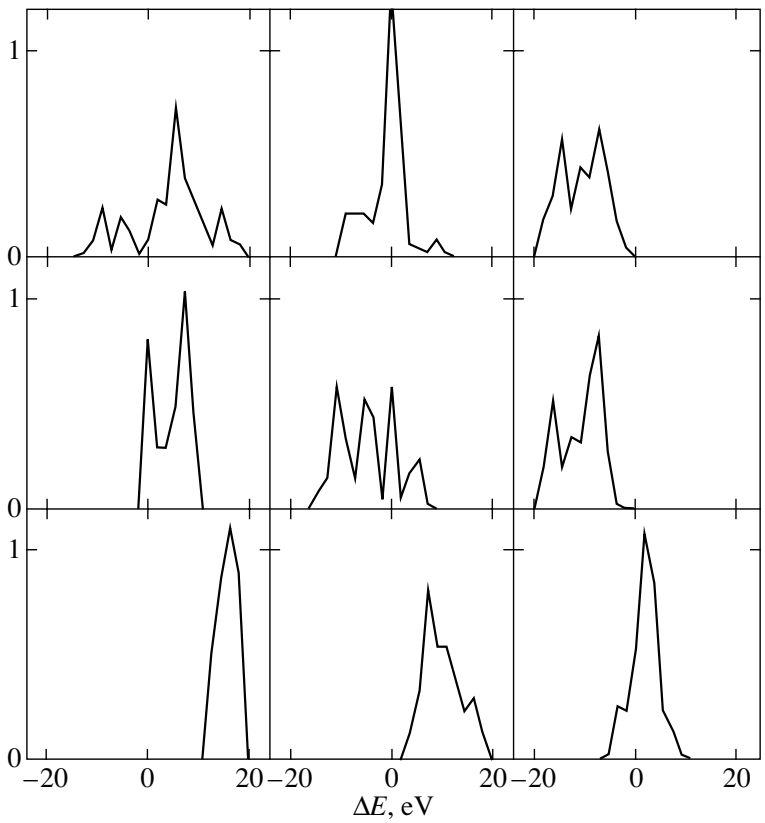

Fig. 6. A map of the $f_{\rm H}(\Delta E, y, z)$ profiles for iron ions in the y, z plane at the points that roughly coincide with the center, vertices, and middles of the sides of the square shown in Fig. 4a.

simplest case of an isothermal plasma with a constant iron abundance along the x axis, they provide information about the velocity distribution of matter relative to the velocity of the cluster as a whole (in particular, the velocity dispersion). Below, we discuss in detail several characteristic features of the spectrum and their relationship to the turbulent velocity field.

To compare the two effects, Fig. 6 shows a map of the velocity distributions $f_{\rm H}(\Delta E)$ over the (y, z) cluster plane. The distributions $f_{\rm H}(\Delta E)$ were computed at the points located at the center, vertices, and middles of the sides of the $2l \times 2l$ square shown in Figs. 4 and 5. We took a frame of reference in which the total momentum $\int\int p(y,z)dydz$ of the emitting and scattering matter is equal to zero. We are seeking for the distributions $f_{\rm H}(\hat{u})$ in this frame. The scale of dimensionless velocities $\hat{u}$ was recalculated to energy shifts ΔE by using formula (1.3) at $u_{\rm rms} = 270$ km s^{-1}. The velocity dispersion changes from point to point in the plane of the sky, $u_{\rm rms} = u_{\rm rms}(y, z)$. To be definite in our normalization of $u_{\rm rms} = 270$ km s^{-1}, we chose the dispersion at the center $y = 0, z = 0$. Note that the dispersion over the cluster as a whole appreciably[16] exceeds the local dispersion. The relief of the kinematic SZ effect is determined by the shift velocity distribution (the average velocity of the column as a whole). We see from Figs. 2a and 2h that these shift velocities give a large contribution to the velocity dispersion in the cluster as a whole.

The $f_{\rm HT}(\Delta E)$ profiles of Fe XXV ($E_0 = 6.7$ keV) lines with turbulent and thermal broadenings are shown in Fig. 7. They were obtained from the distributions $f_{\rm H}(\Delta E)$ in Fig. 6 by folding with the Maxwellian distribution at $kT = 3$ keV. Thermal smoothing "blurs" some of the features in the hydrodynamic distribution $f_{\rm H}$ (at $u_{\rm rms} = 270$ km s^{-1} and $kT = 3$ keV, $\Delta\nu_{\rm DH}/\Delta\nu_{\rm DT} = 2.7$), although the spectra remain fairly complex and varied. The centers of the $f_{\rm H}(\Delta E)$ and $f_{\rm HT}(\Delta E)$ profiles coincide. Of course, they coincide with the profile center determined from the line-of-sight momentum $p(y, z)$. Therefore, the map of the kinematic SZ effect (Figs. 4 and 5) is simultaneously the map of the shifts in profile centers in Figs. 6 and 7. Let us show this by using an example. The black color in the left panel of Fig. 4a

[16] By a factor of 1.5 to 2.5; cf. parabolas *2* and *4* in Fig. 2h.

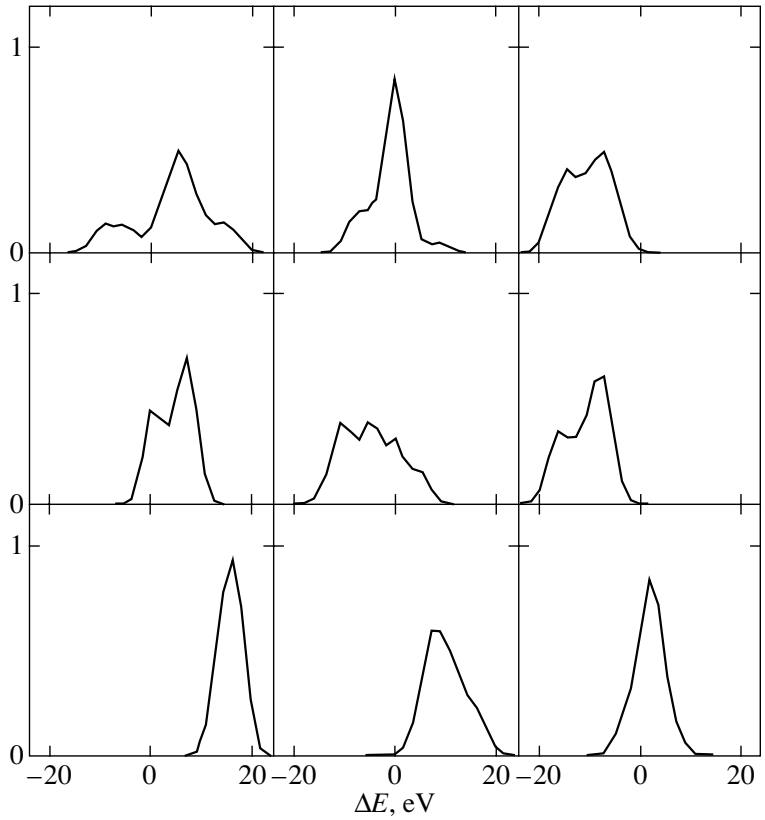

Fig. 7. The $f_{\rm HT}(\Delta E)$ profiles of Fe XXV lines at $kT = 3$ keV (the same as Fig. 2a, but in linear coordinates). The spectrum shown in the middle panel of the upper row is from the three panels used to construct Figs. 1 and 2d. The central panel and the left panel of the bottom row were used in Figs. 2e and 2f.

(the lower left corner of the square) corresponds to the high velocities directed toward the observer. These velocities show up clearly in the rightward shift of the profile along the energy axis from $\Delta E = 0$ in the spectrum in the lower left corner of Figs. 6 and 7, since motion toward the observer causes the photon energy to change. The shifts of the profile center as the position varies in the plane of the sky are large (3–6 local velocity dispersions). Thus, it is possible to independently and experimentally determine the shifts of the profile center by two different methods (the kinematic SZ effect and analysis of the line profile).

The line shape completely changes during the shift to a large distance $\Delta l_\perp \sim L$ in a direction transverse to the x line of sight ($N_{\rm mix} \sim 1$). The shape changes continuously:[17] the change in shape is small for small shifts. For example, the variation of such a parameter as the shift of the profile center during transverse shifts is shown in Fig. 4c. The profiles significantly deviate from the Gaussian profiles (with a large shift of the spectrum center, a splitting of the maximum, and a sharp break in the exponential tails). A comparison with the Gaussian distribution for the middle spectrum from the upper triplet of spectra (Fig. 7) is shown in Fig. 1.

The presence of turbulence in the intergalactic cluster gas and its amplitude can also be judged from differences in the intensity distributions of permitted, on one hand, and forbidden and intercombination lines and their satellites, on the other hand, over the cluster (Gilfanov *et al.* 1987). The optical depth in permitted lines can appreciably exceed unity in the absence of turbulence. Turbulent broadening reduces the optical depth in lines and this effect. *This is a third independent method for studying turbulence in clusters of galaxies.*

Note that Fabian *et al.* (2003) pointed to the existence of long cold Hα-emitting filaments in the Perseus cluster of galaxies as an argument against the well-developed turbulence in this cluster.

The paper is arranged as follows. Section 2 gives a geometrical formulation of the problem with projection onto the observer's direction (line of sight). Section 3 presents the three main components of the Kolmogorov model: two boundaries with the sizes ($L_{\rm mix}, L_\nu$) of the inertial hierarchy of eddies and fluctuation amplitude scaling. Section 4 is devoted to the

[17] Given note (1.8).

Fourier expansion with random phases of the turbulent velocity field. The procedure for calculating the velocity distribution $f_{\rm H}(u)$ from the specific realization $u(x)$ of a random velocity field is described in Section 5. The distribution $f_{\rm H}(u)$ can be calculated approximately from the first moments of the turbulent velocity field (Section 6). When there are many mixers, $N_{\rm mix} \gg 1$, the turbulent distribution $f_{\rm H}(u)$ tends to a Gaussian distribution $f^{\rm G}(u)$ (Section 7). The superposition of thermal and hydrodynamic broadenings is analyzed in Section 8. A theory of the turbulent profile shape is constructed in Sections 9 and 10. We elucidate the question of typical spikes in the profile and its wings and the variety of possible shapes. The transverse correlations (in the plane of the sky) are studied in Section 11. The Lorentz line broadening is taken into account in Sections 12 and 13.

2. TURBULENCE AND DOPPLER SHIFT

We are interested in the emission from the hot intergalactic plasma that fills cluster of galaxies. The plasma is in hydrostatic equilibrium in the gravitational well produced by collisionless dark matter. The density decreases toward the periphery of the well on scales of the order of the cluster scale L. The kinetic energy of the turbulent motion caused by mergers reaches $\sim 15\%$ of the thermal energy. In the context of the formulated problem (a Doppler shift), the hydrodynamic density and plasma temperature fluctuations, which affect the local intensity but not the frequency, are of little importance. The velocity fluctuations dominate.

There is a three-dimensional velocity field, $\mathbf{v}(\mathbf{r}, t)$. It is necessary to determine the Doppler shift in a frame of reference in which the cluster as a whole is at rest. We will consider the line profile when the X-ray telescope is pointed at a point in the cluster plane of the sky. The profile is defined by the function $u(x, t)$ that specifies the velocity u along the x line of sight passing through the observer and the point at which the telescope is pointed. The small eddies that are localized at the points separated along the x axis are statistically equivalent. The turnover time of large-scale eddies is much longer than the time it takes for light to pass through the cluster. In addition, the evolution time of even the smallest observed velocity fluctuations is much longer than the exposure time during which an object is observed from a satellite. Consequently, we may omit the time dependence of the function $u(x, t)$ and deal with the instantaneous velocity field $u(x)$.

The Doppler change in photon energy $\Delta E = E - E_0$ is

$$\frac{\Delta E}{E_0} = -\frac{u}{c}, \tag{2.1}$$

$$\Delta E[\text{ eV}] = 6.7 \frac{u}{300[\text{ km s}^{-1}]} \frac{E_0}{6700[\text{ eV}]},$$

where E_0 is the energy of the photon emitted from a region that is at rest relative to the cluster as a whole, and E is the energy of the photon emerging from a region that is moving with velocity u relative to the adopted frame of reference. Let the cluster be to the right of the observer on the x axis. Accordingly, the velocity u is positive if the emitting region recedes from the observer.

3. THE KOLMOGOROV MODEL

An individual line profile corresponds to each velocity field $u(x)$. We are interested in statistically representative realizations of $u(x)$. The Kolmogorov views of turbulence are of great importance in constructing a typical profile. The point is that they solve the difficult problem of the contribution of small-scale fluctuations.

In a Kolmogorov cascade, energy is transferred from large to small scales. The largest eddies have scales on the order of the mixer size $L_{\rm mix}$. The size L_ν of the smallest eddies is determined by viscous dissipation. A cluster of volume L^3 is assumed to be covered by a three-dimensional mesh of $N_{\rm mix}^3$ statistically equivalent mixers,

$$N_{\rm mix} = L/L_{\rm mix}. \tag{3.1}$$

The $\mathbf{v}(\mathbf{r})$ fluctuations are isotropic in velocity vector orientation. The x axis is not highlighted in any way. Therefore, the Kolmogorov scaling (1.7) can be written for the x velocity component (the projection of three-dimensional fluctuations onto the line of sight). In the hierarchy of scales, the mean energy losses $\dot{E}$ within the inertial range are scale-independent (Kolmogorov 1941),

$$\dot{E} \sim \frac{[(\Delta u)_{\Delta t}]^2}{\Delta t} \sim \frac{[(\Delta u)_{\Delta x}]^3}{\Delta x}, \tag{3.2}$$

where $\dot{E}$ are the hydrodynamic energy losses per gram of matter, and Δu is the velocity variation due to the shift in time Δt or along the line of sight Δx. The Kolmogorov scaling follows from (3.2):

$$(\Delta u)_{\Delta x} \sim \dot{E}^{1/3} (\Delta x)^{1/3}. \tag{3.3}$$

The locally viscous dissipation is given by the formula

$$\dot{E} = (\nu/2) \sum\sum (\partial v_i/\partial x_j + \partial v_j/\partial x_i)^2 \sim \nu (\Delta u)_\nu^2/(\Delta x)_\nu^2, \tag{3.4}$$

where $(\Delta u)_\nu$ and $(\Delta x)_\nu$ are, respectively, the velocity and diameter scales of the eddies in which viscous dissipation takes place. To estimate these

scales, law (3.3) is extended to the range of dissipation through viscosity (Kolmogorov 1941; Monin and Yaglom 1965; Landau and Lifshitz 1986). We then find from formula (3.4) that

$$(\Delta x)_\nu \sim \nu^{3/4}/\dot{E}^{1/4} \sim (c_\mathrm{s}/u_\mathrm{rms})^{3/4} l_p^{3/4} L_\mathrm{mix}^{1/4}, \quad (3.5)$$
$$N_\nu = L/(\Delta x)_\nu,$$

$$(\Delta t)_\nu \sim \sqrt{\nu/\dot{E}}, \quad (3.6)$$

where c_s is the speed of sound, u_rms is the characteristic hydrodynamic velocity (rms deviation or dispersion) defined by the second moment

$$u_\mathrm{rms}^2 = \int u^2 dx/L$$

of the function $u(x)$ (the integral is taken over a range on the order of L), and l_p is the proton mean free path. Large-scale eddies mainly contribute to the dispersion u_rms, while the kinetic energy of the turbulence (see Section 10). N_ν (3.5) gives the number of the smallest eddies on the characteristic cluster scale. Formulas (3.5) and (3.6) define the smallest scales.

The size of small eddies (3.5) is mainly determined by the proton mean free path l_p. The latter varies over a wide range (many orders of magnitude) with amplitude of the random magnetic field in the intergalactic plasma of the cluster. Below, we give the corresponding estimates. In the absence of a magnetic field, the plasma viscosity

$$\nu = 0.48 v_{Tp} l_p = 1.5 \times 10^{27} \frac{T^{5/2}}{n_{-2}},$$

$$l_p = v_{Tp}\tau_p = 7.2 \times 10^{19} \frac{(kT)^2}{n_{-2}}, \quad v_{Tp} = \sqrt{\frac{2kT}{m_p}}$$

is determined by Coulomb collisions between ions (see, e.g., Rosenbluth and Sagdeev 1983); in what follows, the kinematic viscosity ν and the mean free path l_p are in CGS units, the temperature kT is in keV, $n = 10^{-2} n_{-2}$ cm^{-3}, and m_p is the proton mass. The gyroviscosity of plasma with a magnetic field is given by the expression (Rosenbluth and Sagdeev 1983)

$$\nu = 0.5kT/m_p\omega_\mathrm{cp} = 0.25 v_{Tp} r_\mathrm{L},$$
$$r_\mathrm{L} = m_p v_{Tp} c/eH,$$

where ω_cp is the cyclotron frequency of the protons, and r_L is their Larmor radius. The viscous scale ratio is

$$\Delta x_\nu(H=0)/\Delta x_\nu(H\neq 0) = (1.92\tau_p\omega_\mathrm{cp})^{3/4}$$
$$= 2.3 \times 10^6 H_{-8}^{3/4} (kT)^{9/8} n_{-2}^{-3/4},$$

where $H = 10^{-8} H_{-8}$ G. Accordingly, the dimensionless viscous wave numbers N_ν (3.5) are

$$N_\nu(H=0) = 900 N_\mathrm{mix}^{1/4} \mathrm{Ma}^{3/4} L_{200}^{3/4} n_{-2}^{3/4} (kT)^{-3/2},$$

$$N_\nu(H\neq 0)$$
$$= 3.5 \cdot 10^9 N_\mathrm{mix}^{1/4} \mathrm{Ma}^{3/4} L_{200}^{3/4} H_{-8}^{3/4} (kT)^{-3/8},$$

where $\mathrm{Ma} = u_\mathrm{rms}/c_\mathrm{s}$; u_rms and c_s are the characteristic hydrodynamic velocity and the speed of sound, respectively; and $L = 200 L_{200}$ kpc.

In a hot rarefield plasma without a magnetic field, the mean free path l_p is very large. Thus, a situation where N_ν is very small ($N_\nu \sim 1$) is hypothetically possible. As we show in Sections 9 and 10, the line profile in this situation exhibits features that allow it to be distinguished from the case where $N_\nu \gg 1$. Currently available estimates based on Faraday rotation measurements give magnetic field strengths in the range of 1–10 μG (see, e.g., Ge and Owen (1993)), suggesting that the Kolmogorov range in the intergalactic turbulence spectrum is very wide.

4. FOURIER EXPANSION

For the line profile to be constructed, we must know the velocity distribution $f_\mathrm{H}(u)$. The distribution $f_\mathrm{H}(u)$ can be calculated from the velocity field $u(x)$. Let us write out an analytical formula for the function $u(x)$ that satisfies law (3.3). It would be natural to represent the stochastic turbulent motions in the Kolmogorov range of scales as a Fourier series:

$$u'(x;\psi) = N_\mathrm{mix}^\alpha \mathrm{Re} \sum_{n=N_\mathrm{mix}}^{N_\nu} \frac{\exp(i\psi_n)}{n^{\alpha+1/2}} \times \exp\left(\frac{i2\pi n x}{L}\right), \quad (4.1)$$
$$\alpha = 1/3.$$

In formula (4.1), the index α specifies the velocity fluctuation scaling $(\Delta u)_{\Delta x} \propto (\Delta x)^\alpha$. In case (3.3), $\alpha = 1/3$. The phases ψ_n in the harmonic expansion (4.1) are independent random variables uniformly distributed in the segment $[0, 2\pi]$. The velocity is given by the real part of expansion (4.1) (the symbol Re). The summation limits in (4.1) coincide with boundaries (3.1) and (3.5) of the inertial range. The function of x (4.1) is considered in the segment $[l_1, l_2]$ with a length on the order of L. *Series* (4.1) *describes the fractal curve* $u(x)$ *whose fluctuations satisfy the Kolmogorov scaling law* (3.3). This series makes it possible to carry out specific calculations.

Let us displace the auxiliary function u' (4.1) so that the velocity field is centered ($\int u_0 dx = 0$). We change $u' \to u_0$, where

$$u_0(x) = u'(x) - u_1, \quad u_1 = \int_{l_1}^{l_2} u'(x)dx/l_{21}, \quad (4.2)$$
$$l_{21} = l_2 - l_1, (l_1, l_2) \sim L;$$

the function u' can be calculated from formula (4.1). We normalize the function u_0 (4.2) to the rms velocity $u_{\rm rms}$. By definition, $u_{\rm rms}$ gives the dispersion σ of the velocity distribution. The velocity dispersion, along with the kinetic energy of the turbulence, is determined by the large eddies. We write

$$u(x) = u_0(x)/u_{\rm rms}, \quad (4.3)$$
$$u_{\rm rms}^2 = \int_{l_1}^{l_2} [u_0(x)]^2 dx/l_{21}.$$

Below, we deal with the centered (4.2) and normalized (4.3) function $u(x)$, defined by formulas (4.1)–(4.3).

The model of a homogeneous cloud with size L is used as the first approximation to the density distribution. Clearly, this picture can be easily generalized to the real density distribution in clusters of galaxies.

5. THE VELOCITY DISTRIBUTION

Let us explain the meaning of the distribution $f_{\rm H}(u)$. There is the function $u(x)$. Let us divide the u axis into segments δu that are small compared to the viscous fluctuation amplitude $(\Delta u)_\nu$. We consider an arbitrary point $u_\star$ on the u axis. By definition,

$$f_{\rm H}(u_\star) = \frac{dp}{du} = \frac{\sum \delta x}{l_{21}\delta u}, \quad (5.1)$$

where the differential dp characterizes the "weight" of the set of subregions that move with velocity $u_\star$. We assume that the argument of the function $u(x)$ belongs to the region $l_1 \le x \le l_2$ inside the cluster. The condition $u_\star - \delta u/2 \le u(x_\star) \le u_\star + \delta u/2$ is satisfied in each of the small segments δx in sum (5.1). In this condition, the points $x_\star$ belong to any of the small segments δx in sum (5.1). Because of the statistical pulsations in velocity $u(x)$, sum (5.1) can contain many terms. Their number is approximately equal to the numbers of intersections of the function $u = u(x)$ with the straight line $u = u_\star$. It is easy to see that distribution (5.1) is normalized, $\int_{-\infty}^{\infty} f_{\rm H} du = 1$. The corresponding illustration is presented in Fig. 8.

Let us first consider an example with a monotonic function $u(x)$ and then return to the nonmonotonicity and multivaluedness of the function $x(u)$, that is the inverse of $u(x)$, and to the turning points. In the monotonic case,

$$\frac{1}{du(x)/dx} = \frac{dx(u)}{du} = l_{21} f_{\rm H}(u);$$

i.e., the velocity gradient determines $f_{\rm H}$. The equations $u = u(x)$ and $f_{\rm H} = [l_{21} du(x)/dx]^{-1}$ parametrically specify the distribution $f_{\rm H}(u)$. Eliminating the parameter x from this pair of equations yields an explicit dependence $f_{\rm H}(u)$.

Let $u(x) = U \sin(2\pi x/L)$. Eliminating the parameter x, we then obtain

$$f_{\rm H}(u) = \left(l_{21}\frac{du}{dx}\right)^{-1}$$
$$= \frac{L/2\pi l_{21}}{U\cos(2\pi x/L)} = \frac{L/2\pi l_{21}}{\sqrt{U^2 - u^2}}. \quad (5.2)$$

Expression (5.2) specifies the dependence $f_{\rm H}(u)$ in explicit form. Of course, an explicit expression can be derived only for very simple functions $u(x)$.

The example with an oscillating function $u(x)$ clearly illustrates an interesting singularity of the distribution $f_{\rm H}$ in the cold[18] case. It becomes infinite[19] at the stop, turning, or cuspidal points of the inverse function $x(u)$ that are the extrema of the function $u(x)$; because of the root behavior, the distribution $f_{\rm H}(u)$ is asymmetric about the singularity. This question is explored in Section 9. The case with one harmonic (5.2) is an example that differs greatly from the Gaussian distribution. In this example, the dependence $f_{\rm H}(u)$ has a minimum at the center and a singular break in the distribution tail. Consequently, in this example, the regions in which there is motion relative to the observer are more representative than the regions at rest (which is why the distribution maximum is off the center). As we will see below, in the case of many harmonics, the turning points or extrema lead to a needle-shaped distribution, $f_{\rm H}(u)$.

Thus, it is clear that distribution (5.1) is, in a sense, obtained by "projecting" the inverse function $x(u)$ onto the u axis, as shown in Fig. 8 (the connection between Figs. 8a and 8b). Figure 8a shows a realization of $u(x)$ (4.1)–(4.3) with random phases ψ_n ($N \le n \le N_\nu, N_{\rm mix} = 2, N_\nu = 100$) in the interval $l_1 \le x \le l_2$ ($l_1 = 0.2L, l_2 = 0.7L$). The viscous limit is fairly close: $(\Delta x)_\nu = l_{21}/N_\nu \sim 10^{-2}L$, $(\Delta u)_\nu \sim 0.1 u_{\rm rms}$. The viscous values determine the heights and widths of the $u(x)$ spikes (Fig. 8).

[18] In Section 8, we show how thermal Doppler broadening "smears" the singularities caused by turning points.

[19] Of course, this is an integrable singularity.

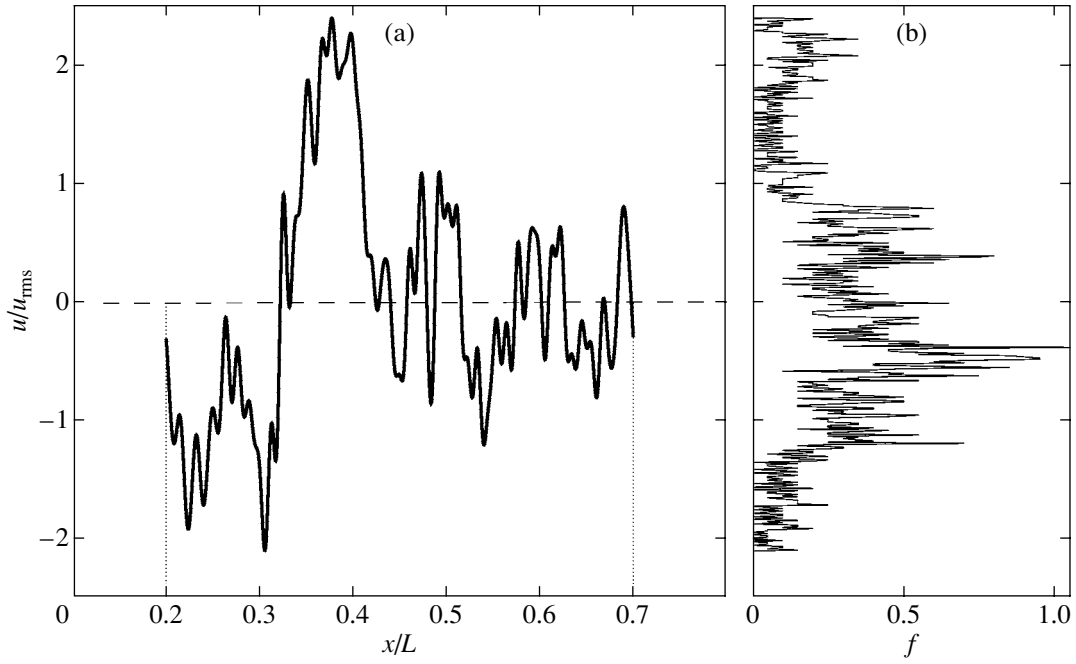

Fig. 8. A scheme for recalculating the instantaneous velocity field $u(x)$ (a) to the velocity distribution $f_{\rm H}(u)$ (b). The recalculation is performed by "projecting" the multivalued function $x(u)$ (the inverse of the function $u(x)$) onto the u axis. The $f_{\rm H}(u)$ profile is similar to the profile of a hydrodynamically (without thermal broadening) broadened line.

In calculating the distribution $f_{\rm H}(u)$, we substituted the velocity $u(x)$ with the set of its values U_i at points $x_i = i\delta x$ (discretization). The δx step was chosen to be small compared to the viscous length $(\Delta x)_\nu$ in order to resolve dissipating eddies. The distribution $f_{\rm H}(u)$ was calculated numerically. It was replaced by a histogram (Fig. 8b) with a small velocity step $\delta u \ll (\Delta u)_\nu$ in order not to lose any fluctuation. Because of discretization, the above singularities of the distribution $f_{\rm H}(u)$ are cut off at turning points. The height of the spikes in the distribution $f_{\rm H}(u)$ is on the order of $\sqrt{(\Delta u)_\nu/\delta u}$; cf. (5.2). The value of $f_{\rm H}(u_\star)$ at the step

$$u_\star - \delta u/2 \le u \le u_\star + \delta u/2$$

of the histogram is proportional to the number of discretization points U_i at the limits $u_\star \pm \delta u/2$. After the normalization $\int f_{\rm H} du = 1$, we obtain the distribution $f_{\rm H}$ shown in Fig. 8b.

It would be natural to analyze the deviations from the Gaussian distribution together with the calculation of moments, because the extent to which the distribution is non-Gaussian can be characterized by the deviations of moments from their Gaussian values.

6. THE METHOD OF MOMENTS

Above, we described the procedure for an exact calculation of the distribution $f_{\rm H}$ (the example in Fig. 8). Concurrently, it is instructive to describe the method for its analytical calculation. We approximate the distribution $f_{\rm H}$ by a polynomial

$$f_{\rm H}(u) = a_0 + a_1 u + a_2 u^2 + ... = \sum_{j=0}^{n_{\rm app}} a_j u^j. \quad (6.1)$$

The calculation procedure is based on the fact that the moments are determined by two independent methods. Let us calculate the moments μ_n directly from the velocity field $u(x)$ and the distribution $f_{\rm H}(u)$. By definition,

$$\mu_n = \int_{l_1}^{l_2} [u(x)]^n dx/l_{21} = \int_{-\infty}^{\infty} u^n f_{\rm H}(u) du. \quad (6.2)$$

The first three moments are known (do not depend on the phases ψ_n): $\mu_0 = 1$ (the normalization condition $\int f_{\rm H} du = 1$), $\mu_1 = 0$ (centering (4.2)), and $\mu_2 = 1$ (the choice of velocity unit (4.3)).

We truncate series (6.1) at the approximation order $n_{\rm app}$. Expansion (6.1) contains $n_{\rm app} + 1$ unknown coefficient a_n. Let us set up a system of equations to determine them. The equations are $\mu_n^u = \mu_n^f$, where the expressions for μ_n^u and μ_n^f are calculated from u and $f_{\rm H}$, respectively (see (6.2)). Let us first calculate the missing moments $\mu_3^u, \mu_4^u, \ldots, \mu_{n-app}^u$ from the velocity $u(x)$. For the given realization, these

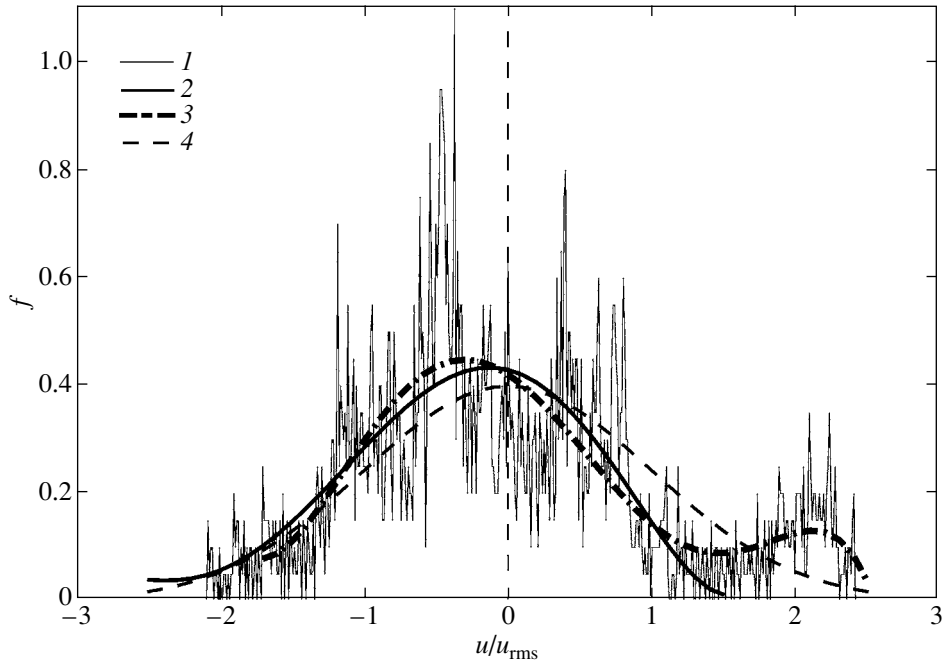

Fig. 9. Comparison of the distributions $f_{\rm H}(u)$: *1*—exact calculation, *2*—calculation by the method of moments (a polynomial up to u^5 inclusive), *3*—a polynomial up to u^6, *4*—Gaussian distribution $f^{\rm G}$ (symmetric about the $u = 0$ vertical line).

are simply certain specific numbers. We then express integrals (6.2)

$$\mu_n^f = \int_{u_l}^{u_r} u^n f_{\rm H}(u) du \qquad (6.3)$$

in terms of expansion (6.1).

Moments (6.3) are linear forms in the unknown a_n. The coefficients of the forms depend on the left, $u_l < 0$, and right, $u_r > 0$, integration limits in (6.3). Clearly, the power-law approximation (6.1) does not describe the decaying tails of the distribution $f_{\rm H}$. Polynomial (6.1) intersects the u axis at points u_l and u_r. Inside the segment $u_l \le u \le u_r$, the polynomial is positive.

Solving the linear system of equations $\mu_n^u = \mu_n^f$ for the unknowns a_n, we express a_n in terms of the zeros u_l and u_r of the polynomial $f_{\rm H}$ in the form of a rational[20] function of u_l and u_r. Substituting the derived expressions for $a_n(u_l, u_r)$ into (6.1) yields the distribution $f_{\rm H}(u_l, u_r; u)$. The zeros u_l and u_r are defined by a system of two equations, $f_{\rm H}(u_l, u_r; u_l) = 0$ and $f_{\rm H}(u_l, u_r; u_r) = 0$. At $n_{\rm app} = 2$ (approximation (6.1) is a parabola), $u_l = -\sqrt{5}$ and $u_r = \sqrt{5}$. In high orders, the equations rapidly become cumbersome.

[20]The ratio of polynomials.

Examples of polynomials for $n_{\rm app} = 5$ and 6 are given in Fig. 9. They refer to the realization of $u(x)$ shown in Fig. 8. The polynomials satisfactorily fit the exact distribution $f_{\rm H}$. The sixth-order polynomial (heavy dash–dotted line) catches even the additional peak in the right wing. Of course, polynomials of a limited order smooth out the needles of the exact distribution. The Gaussian distribution is indicated in Fig. 9 by the dashed curve. We see essentially non-Gaussian behavior, which manifests itself in the profile asymmetry relative to the dashed $u = 0$ vertical line (Fig. 9) and in the break of the distribution tails and the appearance of additional peaks. In addition, the odd moments are nonzero, and the ratios of sequential even moments differ markedly from the Gaussian ratios. For the typical realization shown in Fig. 8, $\mu_3 = 0.51$ and $\mu_5 = 2.97$. The measure of smallness of the odd moments is determined by the normalization $\mu_2 = 1$ (4.3). The increase in the absolute value of the moment with increasing moment number should also be taken into account. In the Gaussian case, the following relations hold: $\mu_4^{\rm G} = 3(\mu_2^{\rm G})^2$, $\mu_6^{\rm G} = 15(\mu_2^{\rm G})^3$. In our case, however, $\mu_4/3 = 0.93$ and $\mu_6/15 = 0.71$.

Let us consider the influence of viscosity. To assess the role of the width of the inertial range $\log \dfrac{N_\nu}{N_{\rm mix}}$, we compared the velocities $u(x)$ and the distributions $f_{\rm H}(u)$ with $N_\nu \sim 10^2$ and $N_\nu \sim 10^3$. As should be the case, the differences are attributable to

the appearance of small-scale fluctuations as N_ν (3.5) greatly increases. The positions and shapes of the significant fluctuations with $\Delta u \sim 0.1 u_{\rm rms}$ depend weakly on N_ν if $N_\nu > 100$. The first moments (up to the sixth moment inclusive) change only slightly (by $\sim 1\%$).

7. GAUSSIAN ASYMPTOTICS

The main regulator on which the deviation of $f_{\rm H}$ from the Gaussian distribution $f^{\rm G}$ depends is the parameter $N_{\rm mix}$ that specifies the extent to which the scale of turbulence (3.1) is large. The viscous scale in this ratio is unimportant. Therefore, we set $N_\nu = \infty$. The difference between the distributions $f_{\rm H}$ and $f^{\rm G}$ decreases with increasing $N_{\rm mix}$. At $N_{\rm mix} = \infty$, the profile is Gaussian. Let us first show this, and then present the results that illustrate the pattern of convergence $f_{\rm H} \to f^{\rm G}$ with increasing $N_{\rm mix}$.

Let us analyze the case with $N_{\rm mix} \gg 1$. Above, the calculations were associated with the dependence of velocity u on coordinate x. In this case, the phases ψ_n (4.1) were fixed. This is an approach that involves averaging over the coordinate. Let us look at the question differently. Let x be fixed ($x = x_{\rm fix}$). The quantity $u(x_{\rm fix}; \psi) = u(\psi)$ gives the velocity at point $x_{\rm fix}$ for a given set of phases ψ (4.1). Let us study the statistics of $u(\psi)$ (an approach that involves phase averaging).

Since the phases ψ_n are independent and random and the position x is fixed, we may omit the regular oscillating factors $\exp(i2\pi nx/L)$ in (4.1). Consequently, the velocity $u(x_{\rm fix}; \psi)$ is given by

$$u = N_{\rm mix}^{1/3} \sum_{n=N_{\rm mix}}^{\infty} \xi_n / n^{5/6}, \qquad (7.1)$$

where, in place of the phases ψ_n, we introduced the equivalent independent random variables ξ_n, $\langle \xi_n \rangle = 0$, and $\langle \xi_n^2 \rangle = 1$; $\langle\rangle$ denotes averaging. We assume for simplicity that ξ_n takes on values of $+1$ or -1 with equal probabilities. The probability distribution function $f_{\rm H}(u)$ of the random variable u (7.1) should be determined.

We see from definition (7.1) that the mean velocity $\langle u \rangle$ is equal to zero. The probability distribution $f_{\rm H}(u)$ is symmetric ($f_{\rm H}$ is an even function of u). All odd moments are zero.[21] It is easy to show that the second moment of (7.1) is

$$\langle u^2 \rangle = N_{\rm mix}^{2/3} \sum_{n=N_{\rm mix}}^{\infty} n^{-5/3}$$
$$= N_{\rm mix}^{2/3} \zeta(5/3, N_{\rm mix}), \qquad (7.2)$$

where $\zeta(5/3, N_{\rm mix})$ is the generalized Riemann zeta function (Vinogradov 1979). In the limit $N_{\rm mix} \gg 1$, $\langle u^2 \rangle = 3/2$, because $\sum n^{-5/3} \approx \int dn/n^{5/3}$.

Let us calculate the fourth moment. We have

$$u^4 / N_{\rm mix}^{4/3} = (\sum \xi_n / n^{5/6})^4$$
$$= -2 \sum \xi_n^4 / n^{10/3} + 3(\sum \xi_n^2 / n^{5/3})^2 + A. \qquad (7.3)$$

In (7.3), the term A is the sum of the terms with an odd number of factors ξ_n. After averaging, the term A vanishes, and we obtain

$$\langle u^4 \rangle / N_{\rm mix}^{4/3} = -2 \sum n^{-10/3} + 3(\sum n^{-5/3})^2$$
$$= -2\zeta(10/3, N_{\rm mix}) + 3[\zeta(5/3, N_{\rm mix})]^2, \qquad (7.4)$$

because $\xi_n = \pm 1$ and $\xi_n^4 = 1$. For $N_{\rm mix} \gg 1$, expression (7.4) tends to the limit

$$\langle u^4 \rangle = 3(3/2)^2. \qquad (7.5)$$

As we see, the ratio of the fourth moment (7.5) to the square of the second moment (7.2), $\langle u^4 \rangle / (\langle u^2 \rangle)^2$, is equal to three. This should be the case for the Gaussian distribution. The aforesaid is also true for the random variables ξ_n of a more general form than $\xi_n = \pm 1$. Indeed, for $N_{\rm mix} \gg 1$, sum (7.1) u includes many approximately equal (in absolute value) independent random terms. In this case, in view of the central limit theorem, the probability distribution of the random variable u is Gaussian. At $N_{\rm mix} \sim 1$, this is not the case, because the first terms in sum (7.1) differ significantly due to the factor $n^{-5/6}$.

It remains to study the convergence $f_{\rm H} \to f^{\rm G}$ with increasing $N_{\rm mix}$. The corresponding results are presented in Table 2.

This table shows how the moments converge to their Gaussian values (the last row). The moments μ_n are defined by formulas (6.2), $R_4 = \mu_4 / 3\mu_2^2$, $R_6 = \mu_6 / 15\mu_2^3$. The first moment is equal to zero due to centering (4.2). Because of normalization (4.3), the second moment is always equal to unity. In the Gaussian limit, $\mu_3 = \mu_5 = 0$ and $R_4 = R_6 = 1$. The procedure for calculating the moments μ_3–μ_6 was described in Sections 5 and 6. The table lists the mean values obtained by averaging over many realizations $\boldsymbol{\xi}$, $u(x)$ (4.1). For the odd moments, we averaged the absolute value of the moment to establish the degree of deviation from zero. The realization-averaged values are given in rows 3–5 of Table 2. For comparison with a unit realization, the second row gives the values that refer to the example in Fig. 8; see also the end of Section 6. This row is highlighted by the symbol ($\star$). The formula

$$R_4^\zeta(N_{\rm mix}) - 1 = \langle u^4 \rangle / 3(\langle u^2 \rangle)^2 - 1$$

[21] In the specific realizations considered in Sections 4–6, the function $f_{\rm H}(u)$ is asymmetric. Here, we deal with the probability distribution after averaging over all possible phases (i.e., over all possible realizations. This distribution is symmetric).

Table 2

$N_{\rm mix}$	μ_2-1	μ_3	R_4-1	$R_4^\zeta-1$	μ_5	R_6-1
$2(\star)$	0	0.51	−0.07		2.97	−0.29
2	0	0.31	−0.11	−0.078	4.8	−0.21
10	0	0.21	−0.077	−0.013	1.7	−0.23
50	0	0.014	−0.045	−0.0026	0.25	−0.16
∞	0	0	0	0	0	0

$$= (-2/3)\zeta(10/3, N_{\rm mix})/[\zeta(5/3, N_{\rm mix})]^2$$

used in column 5 of the table follows from expressions (7.2) and (7.4). It shows the deviation from the Gaussian distribution in the case of averaging over all realizations ξ_n. The corresponding R_4 calculated from the zeta function is denoted by the superscript ζ.

Let us discuss the data in the table. We see that the moments approach their Gaussian values as $N_{\rm mix}$ increases (the refinement of the leading or dominant turbulence scale (3.1)). Therefore, the distribution $f_{\rm H}$ also tends to $f^{\rm G}$. As should be the case, the convergence in lower moments (μ_3, μ_4) is faster than the convergence in higher moments (μ_5, μ_6). The deviations in higher moments are larger, and they decrease with increasing $N_{\rm mix}$ more slowly. The main conclusion is that for large-scale turbulence with $N_{\rm mix} = 2$–10 ($L_{\rm mix} \sim L$, (3.1)), there are significant deviations from the Gaussian distribution.

8. ALLOWANCE FOR THE THERMAL CONTRIBUTION

Above, we analyzed the hydrodynamic component of the line profile. The profile is a combination of the hydrodynamic and thermal components. The thermal velocity distribution along the x axis is given by the Maxwell formula $f_{\rm M} = (1/\sqrt{2\pi}\sqrt{kT/m_i})\exp(-m_i u^2/(2kT))$, where m_i is the ion mass. For iron, $\sqrt{kT/m_i} = 41.4\sqrt{kT}$ km s^{-1}, where kT is in keV. The combined distribution in hydrodynamic and thermal velocities is

$$f_{\rm HT}(u) = \frac{{\rm Ma}_i}{\sqrt{2\pi}u_{\rm rms}} \times \int\limits_{-\infty}^{\infty} f_{\rm H}(u')\exp[-{\rm Ma}_i^2(u-u')^2/2]du'. \quad (8.1)$$

In (8.1), $f_{\rm H}(u')$ under the integral specifies the hydrodynamic or "cold" distribution $f_{T=0}$ studied in Sections 2–7. The distribution $f_{\rm HT}(u)$ is normalized, because $\int f_{\rm H}du = 1$. It depends on temperature T. The line shape is specified by one parameter, the ionic Mach number ${\rm Ma}_i = u_{\rm rms}/\sqrt{kT/m_i}$. The ratio ${\rm Ma}_i$ is proportional to the standard Mach number

$${\rm Ma} = u_{\rm rms}/c_{\rm s} = \sqrt{3/10}\sqrt{m_p/m_i}{\rm Ma}_i,$$

where $c_{\rm s} = 566\sqrt{kT}$ km s^{-1} is the adiabatic speed of sound in a completely ionized hydrogen plasma. Because of the small factor $\sqrt{m_p/m_i}$, the values of Ma and ${\rm Ma}_i$ differ greatly for heavy ions.

Figure 10 compares the cases with ${\rm Ma}_i = \infty$ (thin fluctuating curve), ${\rm Ma}_i = 4.2$ (smooth heavy curve), and ${\rm Ma}_i = 2.3$ (smooth thin curve). The values of ${\rm Ma}_i$ are given for the iron ion. Because of the large iron nuclear mass, the ionic Mach number exceeds unity. The respective values of the Mach number (Ma) are ∞, 0.306, and 0.17. At $u_{\rm rms} = 300$ km s^{-1}, the temperatures kT are 0, 3, and 10 keV in these three cases.

Even a low temperature completely smooths out the small fluctuations in $f_{\rm H}$. As we see, significant deviations from the Gaussian distribution (a shift of the center, asymmetry in the line wings) remain in a hot plasma with $kT = 10$ keV.

The $f_{\rm HT}(u)$ profile (velocity distribution) is similar to the $f_{\rm HT}(\Delta E)$ line profile (energy or frequency distribution). The point $\Delta E = 0$ corresponds to $u = 0$ and $T = 0$. Formula (2.1) should be used to recalculate the $u/u_{\rm rms}$ axis in Fig. 10 to the ΔE axis. For the iron line with energy $E_0 = 6.7$ keV and velocity $u_{\rm rms} = 300$ km s^{-1}, the features of the profile in Fig. 10 attributable to turbulent fluctuations include several bumps, with peaks at energies $\Delta E = -2.8$, 3.7, and 14.1 eV.

9. THE SPECTRUM OF A SINGLE TURNING POINT

The velocity function $u(x)$ along the x line of sight through the cluster is constrained within the fixed limits

$$-\hat{u}'_{\rm H_{max}}u_{\rm rms} < u(x) < \hat{u}_{\rm H_{max}}u_{\rm rms}, \quad l_1 < x < l_2. \quad (9.1)$$

The important constraints (9.1) characterize the maximum hydrodynamic velocities relative to the cluster center. We assume that the velocity u changes continuously with coordinate x. The shock spectrum is not considered here. We also exclude the monotonic $u(x)$ profiles that correspond to simple expansion or contraction of the cluster. Of considerable interest are the nonmonotonic profiles with a "wriggling" (turbulent) function $u(x)$. The most important singularity of a nonmonotonic function is the turning point (Section 5).

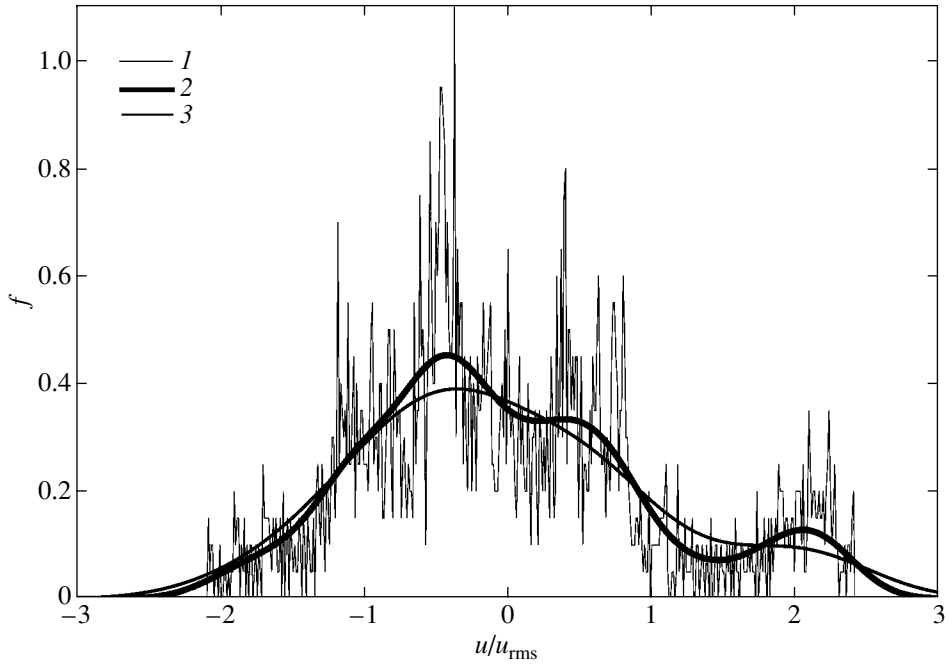

Fig. 10. An illustration of the thermal contribution: *1*—$T = 0$; *2*—$u_{\rm rms} = 300$ km s^{-1}, $kT = 3$ keV; *3*—$u_{\rm rms} = 300$ km s^{-1}, $kT = 10$ keV. For the helium-like iron line with $E_0 = 6.7$ keV, one $u/u_{\rm rms}$ scale division is 6.7 eV.

For Kolmogorov turbulence, $u(x)$ is a fractal function (Sections 3 and 4). Certain statistics of turning points are associated with this function. The shape of the curve $u(x)$ is determined by the dimensionless wave numbers $N_{\rm mix}$ (3.1) and N_ν (3.5), the boundaries of the inertial range. We are interested in the large-scale turbulence ($N_{\rm mix} \sim 1$) that accompanies a cluster merger. It is appropriate to sequentially consider the cases with increasing N_ν, starting from the lowest possible value of $N_\nu \sim 1$. In the simplest case with $N_\nu \sim 1$, there is one turning point (see the example in Fig. 11). We fix the set of random phases ψ_n from $n = N_{\rm mix} = 1$ to $n = N_\nu = \infty$ and retain N_ν terms in series (4.1). We will increase N_ν. The functions $u(x)$ shown in Figs. 11a–15a were constructed in this way.

As the number of generations $\ln(N_\nu/N_{\rm mix})$ increases, the curve $u(x)$ becomes more complex. Since all phases are fixed, the large bumps (eddies) of the curve u are left in their places, and new bumps and dips with a smaller velocity amplitude u and a smaller spatial scale along the x axis pile[22] upon them as the number $\ln(N_\nu/N_{\rm mix})$ increases. A hierarchy of generations or logarithmic tiers known in the theory of fractals arises. In this hierarchy, eddies with velocity $\sim$dm s^{-1} and scale $\sim$dm (second tier), then eddies with velocity $\sim$cm s^{-1} and scale $\sim$cm (third tier), etc., are superimposed on eddies with velocity $\sim$m s^{-1} and scale $\sim$m (first tier). When $\ln(N_\nu/N_{\rm mix}) \to \infty$, the function $u(x)$ and the spectrum $f_{\rm H}(u)$ tend to their fractal limits. The "dressing" of the curve $u(x)$ with small features and the splitting of large spikes in the spectrum $f_{\rm H}(u)$ into small subspikes because of the increase in $\ln(N_\nu/N_{\rm mix})$ clearly show up when comparing Figs. 11a–15a and 11b–15b.

It would be natural to begin our analysis of the spectrum from a single turning point (Fig. 11). This is the subject of this section. The splitting of spikes into subspikes because of the superposition of the next generation of turning points is analyzed in the next section.

Let us consider the spectral trace of a single turning point. We approximate the function $u(x)$ at this point by a parabola: $u(x) = u_0 - (k/2)(x - x_0)^2$, where k is the curvature of the curve $u(x)$ at the turning point (x_0, u_0). We associate the x and u coordinate origins with the vertex of the parabola. In the shifted coordinates,

$$u = -kx^2/2. \qquad (9.2)$$

The "cold" hydrodynamic spectrum $f_{\rm H}$ can be easily found (Section 5, a root singularity):

$$f_{\rm H} \propto dx/du \propto 1/\sqrt{(-u)k}. \qquad (9.3)$$

[22] Since representation (4.1) is the sum of terms with different scales that can be written as a lacunary series.

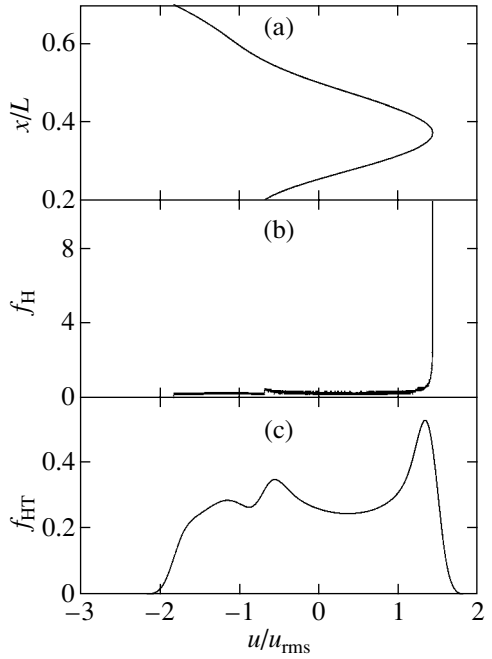

Fig. 11. (a) Gas velocity $u(x)$ in the cluster along the x line of sight, $N_\nu = 3$; (b) the cold velocity distribution $f_H(\hat{u})$ that corresponds to a given field $u(x)$; (c) the distribution $f_{HT}(\hat{u})$ with thermal spread (8.1). The velocities were normalized to u_{rms}, $\hat{u} = u/u_{rms}$.

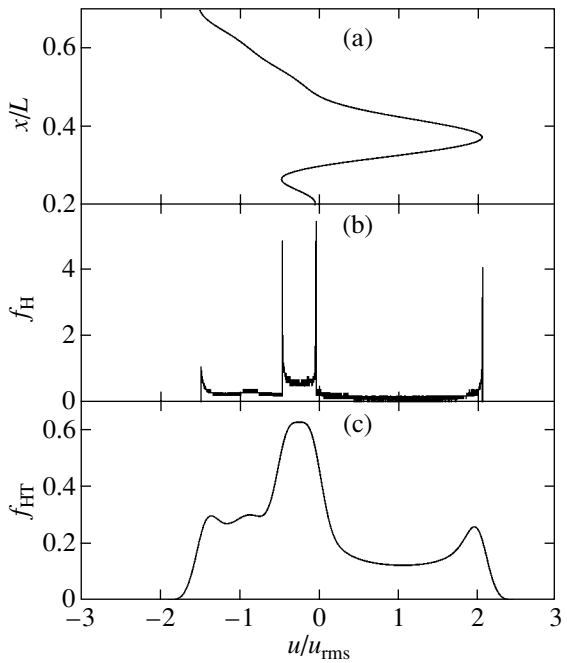

Fig. 12. Same as Fig. 11 for $N_\nu = 7$.

According to (8.1), the thermally broadened hydrodynamic spectrum is given by

$$f_{HT}(u) \propto k^{-1/2} \int_{-\infty}^{0} dw(-w)^{-1/2} \times \exp[-(M_i^2/2)(u-w)^2]. \quad (9.4)$$

Integral (9.4) can be expressed in terms of a modified Bessel function of the second kind. For example, for $u > 0$, we have

$$f_{tp}(u) = \int_{-\infty}^{0} dw \frac{\exp[-(u-w)^2/2]}{\sqrt{-w}} = \sqrt{\frac{u}{2}} \exp\left(-\frac{u^2}{4}\right) K_{1/4}\left(\frac{u^2}{4}\right). \quad (9.5)$$

In Fig. 16, the solid curve represents the spectrum of the turning point $f_{tp}(u)$ (9.5). It is universal. Its spectral width does not depend on the curvature k (9.2). The amplitude of the spectrum for parabola (9.2) is proportional to $1/\sqrt{k}$. The curvature k for large turning points is smaller than that for small ones (see Figs. 11a–15a). Accordingly, the amplitude of the spike from a large parabola is larger (cf. Figs. 11b–13b). We normalize the spectrum f_{tp} to the maximum value of $f_{tp}(u_{max}) = 1$, where $u_{max} = -0.764951$ is the coordinate of the maximum of the function $f_{tp}(u)$ (9.5) (see Fig. 16). The $u = 0$ origin of the u axis in Fig. 16 is at the turning point. The f_{tp} spike is shifted relative to the turning point toward the inside of the parabola by u_{max}. For the normalization $f_{tp}(u_{max}) = 1$, the intensity at the turning point is $f_{tp}(0) = 0.842238$. The f_{tp} spike is asymmetric relative to its maximum. To describe the spectral profile, we also introduce the quantities $\Delta_{0.7}^+$ and $\Delta_{0.7}^-$ that characterize the width and asymmetry of the spike at 70% of its height:

$$\Delta_{0.7}^+ = u_{0.7}^+ - u_{max} = 1.07605, \quad (9.6)$$
$$\Delta_{0.7}^- = u_{max} - u_{0.7}^+ = 1.60725,$$
$$f_{tp}(u_{0.7}^\pm) = 0.7.$$

The parameters u_{max}, $f_{tp}(0)$, and $\Delta_{0.7}^\pm$ (9.6) fully describe the spectral profile of the turning point.

For comparison, Fig. 16 shows the distribution $0.5\exp(-u^2/2)$ proportional to the Maxwellian distribution (dashed curve). The root spectrum (9.3) contains no hydrodynamic velocity scales. The velocity scale appears only in the spectrum f_{HT} or f_{pt} when folded with the Maxwellian distribution. This scale is the thermal velocity $\sqrt{2kT/m_i}$. To reduce the dimensionless spectral widths u_{max} and $\Delta_{0.7}^\pm$ (9.6) to dimensional ones, they must be multiplied by the factor $\sqrt{kT/m_i}$. The unit scale division of the u axis in Figs. 11–15 and Fig. 16 is u_{rms} and $\sqrt{kT/m_i}$,

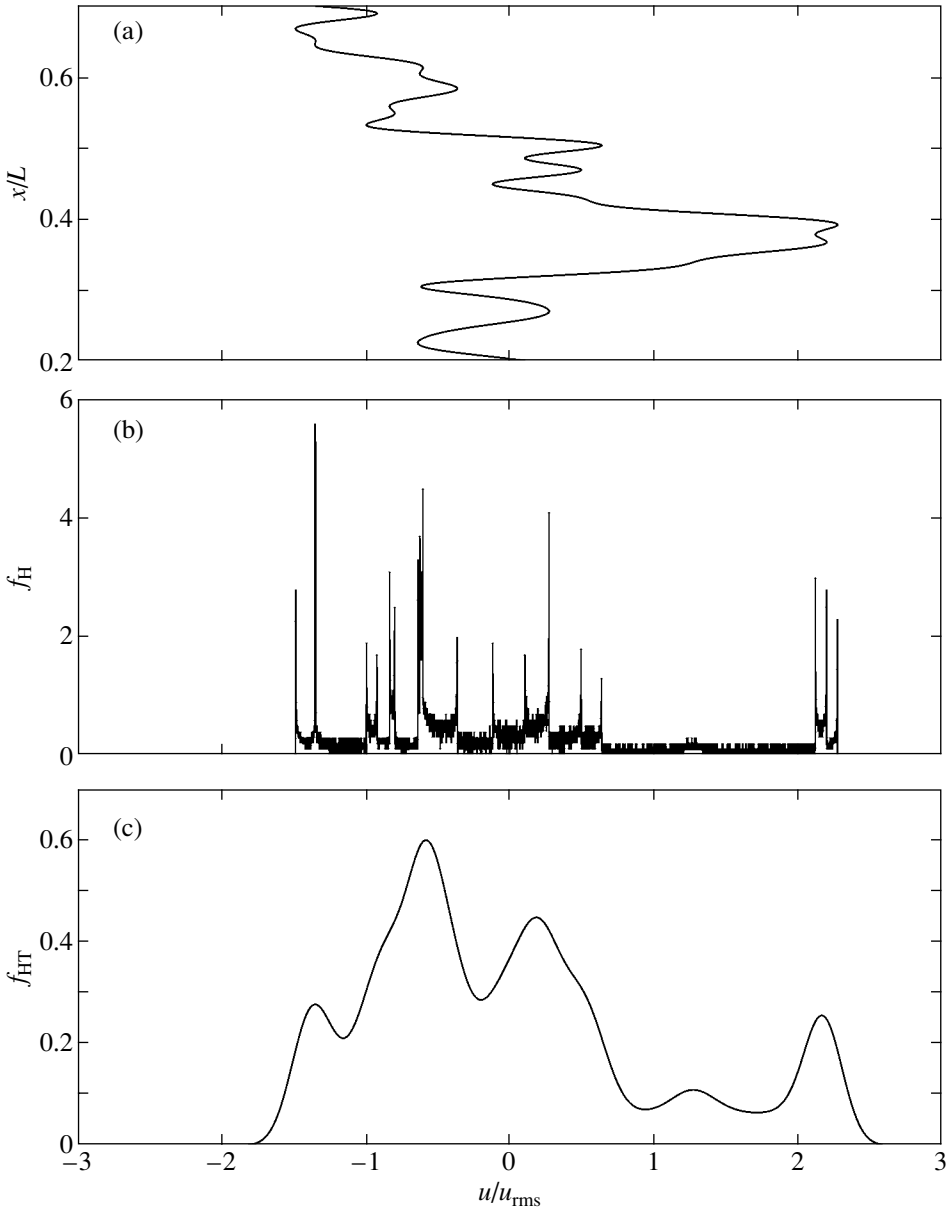

Fig. 13. Same as Fig. 11 for $N_\nu = 30$.

respectively. To reduce Figs. 11–15 and Fig. 16 to the same velocity, frequency, or energy scale, the scale division in Fig. 16 must be decreased by a factor of Ma_i, as can also be clearly seen from a comparison of formulas (9.4) and (9.5).

Let us reconcile, as was said above, the u and peak height scales and superimpose the spike from Fig. 16 on the extreme right spikes in Figs. 11 and 12. The right bump or spike in the spectrum in Figs. 11c–15c corresponds to the large cusp of the function $u(x)$ (cf. Figs. 11a–15a and 11b–15b). The deviation of the right spike in Figs. 11 and 12 from the spectrum of the parabola (9.4, 9.5) is attributable to the presence of cubic terms in the expansion of the function $u(x)$ of general form at the turning point. Let us estimate this deviation quantitatively by comparing parameters (9.6). In Figs. 11 and 12, the maximum of the spike is farther from the turning point (by 6% and 22%, respectively) than that in Fig. 16. The intensity at the turning point is 0.80 (Fig. 11) and 0.75 (Fig. 12) of the intensity at the maximum. These values are lower than 0.84 pertaining to Fig. 16 by 5 and 11%, respectively. The widths $\Delta^{\pm}_{0.7}$ increase by several percent compared to the values (9.6). At the same time, the width ratio $\Delta^{-}_{0.7}/\Delta^{+}_{0.7}$, which characterizes the asymmetry, is approximately the same as that for profile (9.6). In general, it should be concluded that

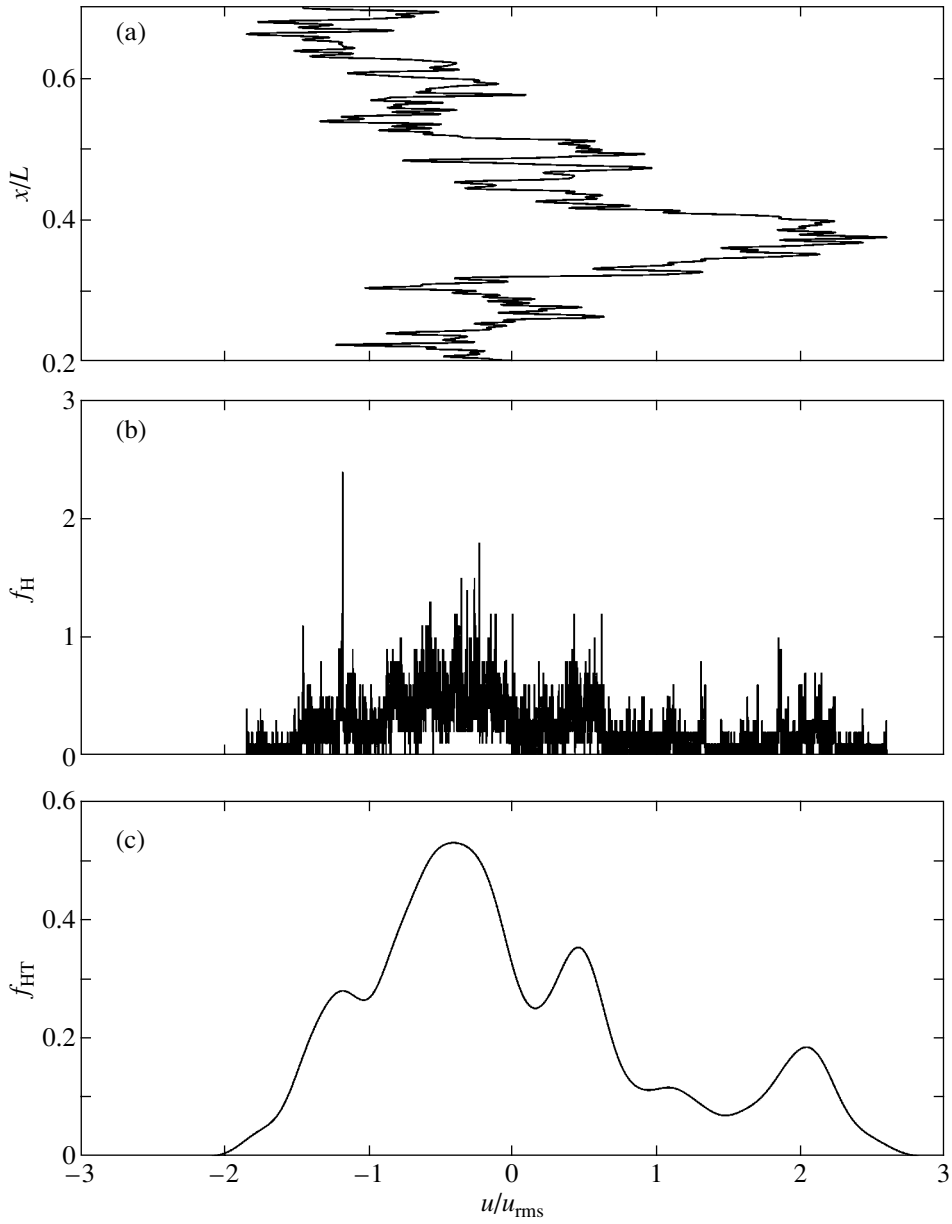

Fig. 14. Same as Fig. 11 for $N_\nu = 200$.

the profiles of the right spikes in Figs. 11 and 12 are well described by the spectrum of the parabola (9.5).

The situation is different when the number N_ν is large, the viscous scale is small, and the curve $u(x)$ is complex. In this case, there are many small turns of the curve $u(x)$ near the large cusp of the function $u(x)$ (see Figs. 14 and 15). Each of these turns has its own root singularity. If the distance along the u axis between these singularities is smaller than the thermal widths (9.6) $\sim\sqrt{kT/m_i}$, then they can merge into a single spike of approximately the same or slightly larger width. A typical example is the right bump in the spectrum $f_{\rm HT}$ in Figs. 14c and 15c. This is how a spectral structure with bumps of an intermediate width between $\sqrt{kT/m_i}$ and $u_{\rm rms} = {\rm Ma}_i\sqrt{kT/m_i}$ arises in a turbulently broadened profile. Let us now study this question.

10. THE NUMBER OF GENERATIONS IN THE KOLMOGOROV HIERARCHY AND THE SHAPE OF A COMPLEX LINE

The goal of the spectroscopic analysis of the line profile structure is to detect the relative bulk motions of intergalactic masses. Information about the spatial velocity field $\mathbf{v}(\mathbf{r})$ is contained, first, in the positions

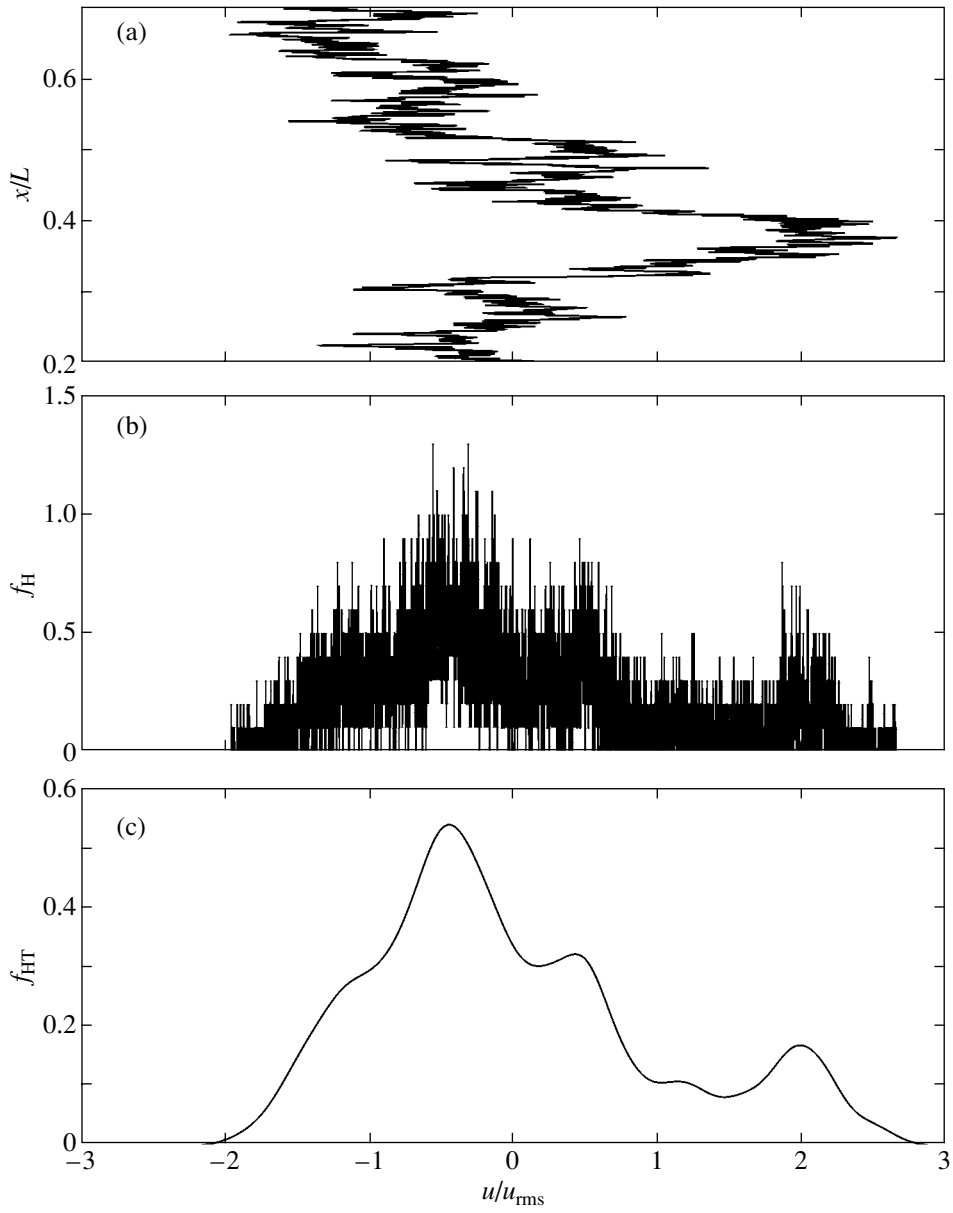

Fig. 15. Same as Fig. 11 for $N_\nu = 1000$.

of the breaks in the profile tails (see Sections 12 and 13), second, in the profile shape itself, and, third, in the correlations in the plane of the sky (Section 11). An important objective of X-ray spectroscopy is the detection of internal spikes in the line profile and their analysis, because, as we showed in Section 9, these spikes directly originate from important features of the velocity distribution $u(x)$.

The Kolmogorov cascade is limited by $N_{\rm mix}$ (3.1) and N_ν (3.5) from large and small scales, respectively (Sections 3 and 4). The number of generations of eddies with different scales in the hierarchy of sizes is $\sim\ln(N_\nu/N_{\rm mix})$. The viscous scale N_ν determines the velocity gradient $|\nabla v|$ or u_x. At $N_{\rm mix} \sim 1$, $(\Delta u)_{\Delta x} \sim u_{\rm rms}/(L/\Delta x)^{1/3}$; accordingly,

$$u_x \sim (\Delta u)_\nu/(\Delta x)_\nu \sim N_\nu^{2/3}(u_{\rm rms}/L). \qquad (10.1)$$

At very low viscosity, gradient (10.1) is large compared to the characteristic value of $u_{\rm rms}/L$. In the limit $N_\nu \to \infty$, the function $u(x)$ is similar to the continuous but nondifferentiable Weierstrass function (Vinogradov 1979). Since the velocity variation scale is limited above by $\sim u_{\rm rms}$, the larger the gradient (10.1), the greater the "wriggling" of the function $u(x)$ (and the stronger its jaggedness; cf. Figs. 11a–15a).

Depending on the magnetic field strength (Section 3), the functions $\mathbf{v}(\mathbf{r})$ have different degrees of

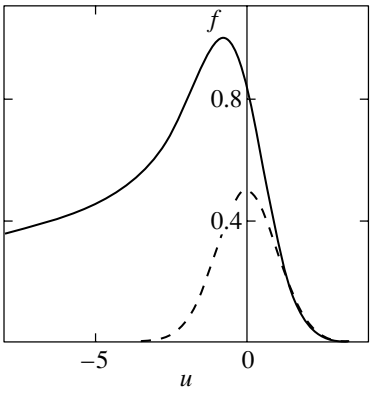

Fig. 16. The asymmetric spectrum of a turning point. The dashed curve indicates a symmetric distribution proportional to the Maxwellian distribution. The tip of the turning point is taken as the coordinate origin $u = 0$. The scale division on the u axis is $\sqrt{kT/m_i}$.

smoothness. In the absence of a magnetic field, the ion mean free path is comparable to the cluster size L. Under these conditions, a situation with large N_ν is possible: $N_\nu \sim 1$. Smooth functions $u(x)$ correspond to this situation. Even weak magnetic fields greatly increase N_ν, which is the reason why the extremely jagged functions $u(x)$ appear.

Let us consider the influence of the smoothness of $u(x)$ on the spectrum. The corresponding examples with $N_{\rm mix} = 1$ (3.1) and different values of N_ν (3.5) are presented in Figs. 11–15. There are smooth and nonsmooth cases. The separation between them is determined by the ratio of hydrodynamic and thermal broadenings $\mathrm{Ma}_i = u_{\rm rms}/\sqrt{kT/m_i} = \sqrt{2}\Delta\nu_{\rm DH}/\Delta\nu_{\rm DT}$, and the instrumental resolution $\Delta E_{\rm line}/\delta E$, where $\Delta E_{\rm line}$ is the profile width, and δE is the energy resolution. In clusters of galaxies, the largest value of Ma_i for the iron ion is ~ 10. For a line of width $\Delta E_{\rm line} \sim 40$ eV, the thermal spread is $\sim \Delta E_{\rm line}/\mathrm{Ma}_i \sim 4$ eV. We assume that the instrumental value of δE is lower.

Figures 11a–15a, 11b–15b, 11c–15c are grouped so as to make clear the threads that link the velocity profile $u(x)$ and the spectrum $f(u)$ (the "reading" of the spectrum in direct, $u \to f_{\rm H} \to f_{\rm HT}$, and reverse, $f_{\rm HT} \to u$, orders; cf. Fig. 8). The correspondence between the field $u(x)$ and the "cold" spectrum $f_{\rm H}$ is closer. Part of the information is lost through thermal smoothing ($f_{\rm H} \to f_{\rm HT}$). The largest number of features (spikes) that the turbulent–thermal spectrum $f_{\rm HT}$ can contain is on the order of Ma_i. It would be reasonable to assign the cases where all features of $u(x)$ and $f_{\rm H}$ are resolved into separate spikes in the spectrum $f_{\rm HT}$ to the smooth fields and spectra u and $f_{\rm H}$. Examples of smooth fields are shown in Figs. 11 and 12. Figures 11–15 pertain to the case with $\mathrm{Ma}_i = 8.37$ ($kT = 3$ keV, $u_{\rm rms} = 600$ km s^{-1}). Therefore, the smooth functions $u(x)$ must contain no more than several characteristic features. Roughly speaking, $u(x)$ with $N_\nu < \mathrm{Ma}_i$ are smooth functions, because the number of features is on the order of N_ν.

We assign $u(x)$ with a rich ($N_\nu > \mathrm{Ma}_i$) "cold" spectrum $f_{\rm H}$ to very jagged or nonsmooth functions. In this case, there are many features. In the spectrum $f_{\rm HT}$, they are statistically grouped into broadened spikes (see Figs. 13c–15c). The characteristic features are the turning points of the curve $u(x)$ with which the root singularities of the hydrodynamic distribution $f_{\rm H}$ are associated (Sections 5 and 9). As we said above, the number of features increases together with the number of generations. The causes of the spectrum complication due to the splitting of spikes become completely clear if we compare Figs. 12a, 12b and 13a, 13b (the "reading" of the spectrum). There is one right turning point in Fig. 12 ($N_\nu = 7$). In Fig. 13 ($N_\nu = 30$), three turns appear instead of one due to the extension of the range $N_{\rm mix} < n < N_\nu$ and the increase in gradient (10.1). Accordingly, the right spike in the spectrum $f_{\rm H}$ splits into a group of three spikes. Whereas the right spike in the spectrum $f_{\rm HT}$ in Fig. 12 has a root profile (Section 9, Fig. 16), the spike in the spectrum $f_{\rm HT}$ in Fig. 13 is symmetrized, $\Delta^-_{0.7}/\Delta^+_{0.7} \approx 1.15$, because of its splitting and shifts farther from the extreme turn $u_{\max} = 1.06\sqrt{kT/m_i}$. At the same time, it remains narrow, $\Delta^-_{0.7} + \Delta^+_{0.7} \approx 2.1\sqrt{kT/m_i}$.

Let us present the thermally broadened hydrodynamic spectrum $f_{\rm HT}$ in the case of $N_\nu = \infty$ concerned. Figures 11c–15c are collected in Fig. 17, which illustrates the spectrum transformation with increasing N_ν. $N_\nu = 30$ is the boundary case that separates the smooth ($N_\nu < \mathrm{Ma}_i$) and "saturated" spectra: $N_\nu \gg \mathrm{Ma}_i$, $N_\nu = \infty$ (here,[23] $\mathrm{Ma}_i = 8.37$). The dependence on N_ν is "saturated" for $N_\nu > 200$. To show this, we superimposed the spectrum with $N_\nu = 1000$ on the spectrum with $N_\nu = 200$ (Fig. 17d). As we see, the difference between the spectra is small. Thus, the spectrum with $N_\nu = 1000$ may be taken as the limit at $N_\nu = \infty$.

The first bump at the edge of the profile can be easily interpreted. This is a large intense velocity fluctuation "dressed" at $N_\nu = \infty$ with the fractal cascade of its accompanying fragmenting eddies.[24] A large-scale cusp of the continuous function $u(x)$ is always

[23] For the iron ion, $\mathrm{Ma}_i \sim 10$ is the maximum possible value for typical clusters.

[24] The turbulent broadening of the bump was caused precisely by this "dressing" with fractal subspikes. It is important that this broadening is much smaller than the hydrodynamic velocity scale $u_{\rm rms}$. Therefore, the turbulent spectrum $f_{\rm HT}$ is complex; see below.

associated with a bump in the spectrum. Thus, the presence of a bump at the edge of the profile determined by velocities (9.1) is a typical phenomenon. The largest fluctuation in the curve $u(x)$ is almost always single (see the examples in Figs. 6, 8, 15). The bump in the spectrum associated with it (the thermal broadening of an agglomerate of small eddies) is then also single (here, in the sense that it is not superimposed on other bumps—agglomerates of small eddies).

Let us compare the right bump in the smooth, boundary, and "saturated" cases. In the limit $N_\nu = \infty$, (i) its profile is roughly symmetric relative to the top; (ii) the width is on the order of the thermal width, and in Figs. 15 and 17, we have

$$\Delta^-_{0.7} + \Delta^+_{0.7} \approx 3\sqrt{kT/m_i}; \qquad (10.2)$$

(iii) the maximum is far[25] from the edge $\hat{u}_{\mathrm{H_{max}}}$ ($u_{\max} \approx 4.5\sqrt{kT/m_i}$); (iv) accordingly, the amplitude at the edge[26] is small:

$$f_{\mathrm{HT}}(u_{\mathrm{H_{max}}})/(f_{\mathrm{HT}})_{\max} \sim 0.1,$$

where $(f_{\mathrm{HT}})_{\max}$ is the intensity at the top of the bump. The monotonically falling tail of the Maxwellian thermal distribution protrudes from the edge $u_{\mathrm{H_{max}}}$. It decays exponentially on a thermal scale $\sim\sqrt{kT/m_i}$ that is small compared to the characteristic hydrodynamic velocity, $\sqrt{kT/m_i} = u_{\mathrm{rms}}/\mathrm{Ma}_i$. The Maxwellian thermal decay is clearly seen on a logarithmic scale (cf. Figs. 2a and 7). We will naturally elucidate this question below (Sections 12 and 13) when studying the separation of the profile into hydrodynamic, thermal, and radiation (Lorentz) zones.

Above, we considered a separate bump (agglomerate) near the edge $u_{\mathrm{H_{max}}}$ of the "cold" hydrodynamic distribution. It is a product of the thermal merging of an agglomerate of small eddies near the large-scale velocity fluctuation (hence the agglomerate). Let us now consider the thermal–hydrodynamic profile f_{HT} (at $N_\nu = \infty$) as a whole. In contrast to the simple Maxwellian bump f_{Maxw}, the structure of the turbulent profile f_{turb} is much more complex. The two main differences associated, respectively, with the wings and the central zone are as follows: First, the distribution f_{turb} lies within interval (9.1) of very limited velocities $u_{\mathrm{H_{max}}}/u_{\mathrm{rms}}$, while the wing of the distribution $f_{\mathrm{Maxw}} = (\sqrt{2\pi}u_{\mathrm{rms}})^{-1}\exp(-u^2/2u^2_{\mathrm{rms}})$ begins early (at the inflection point $u = u_{\mathrm{rms}}$) and extends quite far (up to $u = \infty$). Second, whereas the profile f_{Maxw} is single,[27] there is a wide variety of profiles for the spectrum f_{turb}. The point is that the profile f_{turb} is the sum of several ($\sim\mathrm{Ma}_i$) individual agglomerate bumps with random positions and heights. The positions of narrow (with a width $\sim\sqrt{kT/m_i}$) individual agglomerates vary over a wide ($\sim u_{\mathrm{rms}}$) range. This is the reason why the above wide variety of profiles f_{turb} arises (see, e.g., Fig. 6). In the central zone, the profiles f_{turb} differ significantly from the Gaussian distribution with the total dispersion squared

$$f_{\mathrm{Maxw}} = \frac{\exp[-u^2/2(1+\mathrm{Ma}_i^{-2})u^2_{\mathrm{rms}}]}{\sqrt{2\pi}\sqrt{1+\mathrm{Ma}_i^{-2}}u_{\mathrm{rms}}} \approx \frac{\exp(-u^2/2u^2_{\mathrm{rms}})}{\sqrt{2\pi}u_{\mathrm{rms}}}, \quad \mathrm{Ma}_i \gg 1, \qquad (10.3)$$

in that they strongly fluctuate about this Maxwellian function (see Figs. 9 and 17). The dashed curve in Fig. 17e indicates function (10.3) (see also Figs. 1, 2).

The group of agglomerate bumps of thermal width scattered over a wide range on the order of the hydrodynamic velocity form the thermal–hydrodynamic profile f_{HT} shown in Fig. 17e. The largest bump *1* is the sum of several individual agglomerate bumps some of which (marked by numbers *2*) are clearly seen against the general background. Vertex *1* is shifted significantly from the center $u = 0$ (deviation *3*). This shift is attributable to the large odd moments (see Table 2 in Section 7). The individual agglomerate bump *4* discussed above lies on the periphery of the profile f_{HT}; its large distance from the center compensates for shift *3* of the main bump (by definition (4.2), the mean velocity is equal to zero).

Let us now consider the wings of the turbulent–thermal distribution $f_{\mathrm{HT}}(u)$. The wing position and shape are determined, respectively, by $\hat{u}_{\mathrm{H_{max}}}$ and the function $f_{\mathrm{HT}}(u)$ near this extreme value. The boundary value $\hat{u}_{\mathrm{H_{max}}}$ is important, because at high velocities, $\hat{u} > \hat{u}_{\mathrm{H_{max}}}$, the function $f_{\mathrm{HT}}(u)$ decays exponentially with a large[28] exponent. The $\hat{u}_{\mathrm{H_{max}}}$ value bounds the hydrodynamic zone shortly after which the Lorentz asymptotics begins (Sections 12 and 13). After averaging over phases (4.1), $\hat{u}_{\mathrm{H_{max}}}$ becomes a function of the parameters N_{mix} and N_ν. The dependences on N_{mix} and N_ν are qualitatively different. We begin from the simpler dependence on N_ν.

[25] Cf. $u_{\max} = 0.764951\sqrt{kT/m_i}$ in the case of a root bump, Section 9.

[26] Cf. $f_{\mathrm{tp}}(0)/(f_{\mathrm{HT}})_{\max} = 0.842238$, Section 9.

[27] One well-filled bump fixed at the center $u = 0$.

[28] Since the parameter Ma_i is large. This parameter ($\mathrm{Ma}_i = u_{\mathrm{rms}}/\sqrt{kT/m_i}$) determines the ratio of the decay rates of the hydrodynamic and thermal exponents.

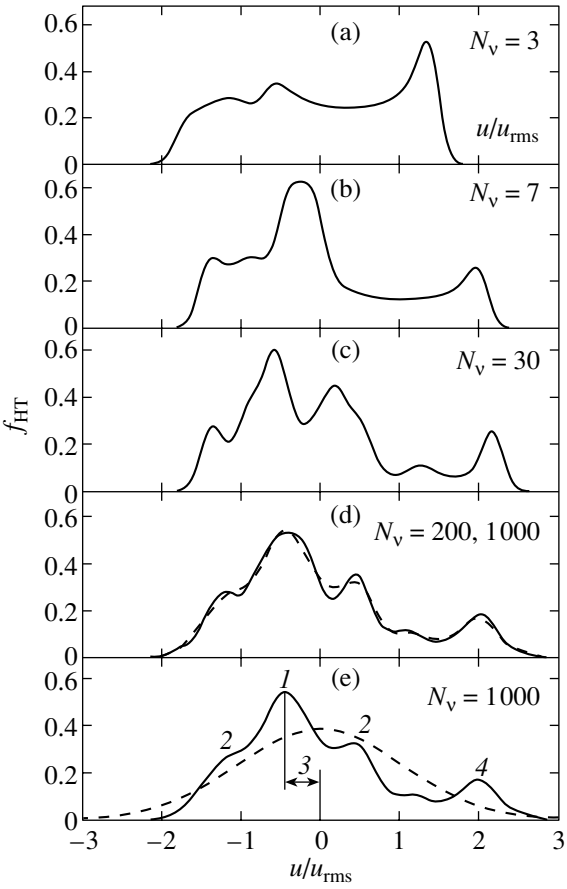

Fig. 17. Modification of the spectrum $f_{\rm HT}(\hat{u})$ when the number of generations $\ln(N_\nu/N_{\rm mix})$ in the Kolmogorov hierarchy increases. The spectrum with $N_\nu = 1000$ is superimposed on the spectrum with $N_\nu = 200$. The dashed curve in the lower panel indicates the Gaussian profile with total dispersion $\sqrt{u_{\rm rms}^2 + kT/m_i}$.

We fix $N_{\rm mix} \sim 1$ and vary N_ν between $N_\nu \sim 1$ and $N_\nu = \infty$. The $\hat{u}_{\rm H_{max}}$ value turns out to remain finite ($\hat{u}_{\rm H_{max}} \sim 1$) as N_ν is varied. Indeed, when we add new generations,[29] $\hat{u}_{\rm H_{max}}(N_\nu)$ increases roughly as the sum of a geometric progression with decreasing terms, as follows from representation (4.1). Each generation or tier has its own spatial scale and variability amplitude. The fluctuation amplitudes in adjacent tiers differ by a finite factor (see also Section 9). The geometric progression is obtained from this and from the equivalence of different tiers. Since the fluctuation amplitude decreases with increasing N_ν, the series rapidly converges. Thus, the formation of the curve $u(x)$ through the fractal pile-up of eddies discussed in Sections 9 and 10 leaves the velocity range (9.1) very limited.

[29] The number of generations or logarithmic tiers $\ln(N_\nu/N_{\rm mix})$ increases with N_ν.

The boundary of the hydrodynamic zone (Sections 12 and 13) $\hat{u}_{\rm H_{max}}$ is determined by the number of mixers $N_{\rm mix}$ (3.1) along the line of sight. We set $N_\nu = \infty$. Consider the dependence $\hat{u}_{\rm H_{max}}(N_{\rm mix})$. At $N_{\rm mix} = 1$, $\hat{u}_{\rm H_{max}}(1) \approx 1.8$–$2.7$. These values follow from experiments with many different realizations of representation (4.1). The function $\hat{u}_{\rm H_{max}}(N_{\rm mix})$ increases with $N_{\rm mix}$; the condition $\hat{u}_{\rm H_{max}}(\infty) = \infty$ is satisfied. In the limit $N_{\rm mix} \to \infty$, the spectrum $f_{\rm HT}(u)$ tends toward the Gaussian distribution (10.3) (see Section 7).

The number $N_{\rm mix}$ determines the wavelength $\lambda_N = L/N_{\rm mix}$ and the wave number $k_N = 2\pi N_{\rm mix}/L$ of the largest-scale harmonic in series (4.1). Some $N_{\rm mix}$ bumps or maxima of the harmonic $\cos(k_N x)$ fit in a segment of the x line of sight with a length on the order of the length L of the cluster of intergalactic gas. Given the factor $N_{\rm mix}^{\alpha}$ in front of sum (4.1), the amplitude of this harmonic is $1/\sqrt{N_{\rm mix}}$. Let us consider the range $N_{\rm mix} \le n \le 2N_{\rm mix}$ of numbers n adjacent to the first number $n = N_{\rm mix}$. $N_{\rm mix} + 1$ harmonics with wavelengths λ_n of the same order of magnitude as the wavelength λ_N of the first harmonic fall within this range. All these harmonics are roughly equivalent, since their spatial scales λ_n are of the same order of magnitude. These waves form the first tier with the largest scale and amplitude.

Since the phases ψ_n in representation (4.1) are randomly scattered, there is a random interference between the waves of the first tier. We fix the realization.[30] We add $\sim N_{\rm mix}$ harmonics of the first tier or generations with amplitudes $a_n \sim 1/\sqrt{N_{\rm mix}}$ according to rule (4.1). As a result, we obtain the function $u(x)$ that has approximately $N_{\rm mix}$ bumps and dips in a segment $\sim L$ with a bump amplitude (height) $\sim A_N \sim 1$. Representation (4.1) models the physical situation with the interference of random waves. Note the qualitative difference between the amplitude a_n of harmonic n and the fluctuation amplitude A_N of the random sum of such harmonics. It is equivalent to the difference between the Fourier harmonic amplitude u_n of the function $u(x)$ and the characteristic scale of the velocity change $(\Delta u)_{\Delta x}$ for a shift in coordinate by $\Delta x \sim \lambda_n$. This difference is large for large numbers $N_{\rm mix}$, when many harmonics fall within the range of characteristic scales $\lambda_n \sim \lambda_N$.

Let us consider the function $u(x)$ and the corresponding distribution $f_{\rm H}(u)$ (Section 5). The dispersion of the distribution $f_{\rm H}$ is determined by the mean height of the bumps of the first tier, $\sim A_N$. As we said above, $A_N \sim 1$. Here, we use the dimensionless

[30] That is, we throw out one set of phases with a random number generator.

velocity (normalized to the dispersion $u_{\rm rms}$; see Section 4). The position of the hydrodynamic boundary $\hat{u}_{\rm H_{max}}$ is specified by the highest bump in the ensemble of bumps on the x axis. Since the ensemble is limited ($N_{\rm mix} < \infty$), the probability of occurrence of a very high (many dispersions) bump is exponentially low.[31] Estimation of this probability yields the sought-for boundary $\hat{u}_{\rm H_{max}}$.

For our calculation, we use the Gaussian distribution $f_{\rm G}(\hat{u})$ (10.3). The following relation is well-known:

$$\Phi(\hat{u}) = 1 - \int_{-\hat{u}}^{\hat{u}} f_{\rm G}(\hat{w})d\hat{w} = 1 + {\rm Erf}(\hat{u}/\sqrt{2}). \quad (10.4)$$

The velocity boundary $\hat{u}_{\rm H_{max}}$ is a statistical quantity. We are interested in its typical highest value of $\hat{u}_\star$ that can appear in a representative percentage (say, 50% ($p = 0.5$)) of spectra.[32] Using the definition of the function $\Phi(\hat{u})$ (10.4), we obtain

$$\Phi(\hat{u}_\star) = 1/(N_{\rm mix}/p). \quad (10.5)$$

It follows from simple calculations using Eq. (10.5) that

$$\hat{u}_{\rm H_{max}}(2) \approx 1.2, \quad \hat{u}_{\rm H_{max}}(7) \approx 1.8, \quad \hat{u}_{\rm H_{max}}(30) \approx 2.4.$$

Above, we discussed the estimation of the height for the largest typical bump in the ensemble of $N_{\rm mix}$ bumps.[33] The bump is formed by a random superposition of the waves of the first tier. All of the next smaller-scale tiers must be taken into account for $N_\nu = \infty$. As we said, the corresponding problem leads to a rapidly converging geometric progression. Adding higher tiers increases $\hat{u}_{\rm H_{max}}$ by a certain factor F that depends weakly on $N_{\rm mix}$ in the range $1 \le N_{\rm mix} \le 30$. Statistical simulation based on representation (4.1) yields $F \sim 1.1$–1.5.

We emphasize that $\hat{u}_{\rm H_{max}}$, the highest velocity, is limited above by the speed of sound $c_{\rm s}$.

Above, we analyzed the first part of the problem on the wing of the spectrum $f_{\rm H}$ pertaining to the determination of its extent.[34] In the second part, the shape of the profile near the boundary $\hat{u}_{\rm H_{max}}$ must be studied. Again, we deal with the typical shape that shows up in a representative percentage of the spectra. As we said, in the ensemble of $N_{\rm mix}$ bumps, the distance from the center of the spectrum $u = 0$ to its boundary is equal to the height of the highest bump. It is important to note that since the ensemble is "short,"[35] the next highest bump is much lower (approximately equal high spikes are unlikely). A certain gap in heights Δ arises between the highest bump and the bump that follows it. At high values of the main parameter ${\rm Ma}_i$, the gap Δ in a representative percentage of the spectra can significantly exceed the thermal scale $\sqrt{kT/m_i}$.

In this situation, a spike of approximately thermal width emerges in the spectrum $f_{\rm HT}$ near the boundary $\hat{u}_{\rm H_{max}}$. It is quite similar to spike *4* in Fig. 17e. We emphasize that $N_{\rm mix} = 1$ in the case shown in Fig. 17. In contrast, here, we discuss the ensemble ($N_{\rm mix} > 1$). The described wing structure of the turbulent–thermal profile $f_{\rm HT}$ differs qualitatively from the Gaussian structure. First, there is a sharp break in the profile at $\hat{u}_{\rm H_{max}}$, and, second, nonmonotonicity (a nonmonotonic decrease in intensity, a spike at the edge) appears.

The asymmetry of the profile as a whole is related to the question of a large spike and a large wing extent. The point is that, above, when discussing the highest bump, we meant the absolute value of the deviation from the line center ($u = 0$) by its height. Meanwhile, the deviation has a sign: $\hat{u}_{\rm H_{max}} > 0$ and $-\hat{u}'_{\rm H_{max}} < 0$ are the right and left boundaries of the profile $f_{\rm H}$, respectively; see (9.1). Let the highest bump be "ejected" to the right; the condition $\hat{u}_{\rm H_{max}} > \hat{u}'_{\rm H_{max}}$ is then satisfied. In these cases, a group of ($N_{\rm mix} > 1$) low bumps happens to emerge on the left in a representative percentage of the spectra. Thus, the inequality $\hat{u}'_{\rm H_{max}} < \hat{u}_{\rm H_{max}}$ is a manifestation of the asymmetry. In addition, the function $f_{\rm HT}(\hat{u})$ behaves differently near the points $\hat{u}_{\rm H_{max}}$ and $-\hat{u}'_{\rm H_{max}}$ at which the spectrum $f_{\rm H}(\hat{u})$ ends. Recall that the spectrum $f_{\rm H}$ is obtained from the velocity field $u(x)$ by a kind of projection (Fig. 8). The "shadow" (projection) of the highest bump lies to the right in the spectrum

[31] The growth of an extended Gaussian wing is a process that requires a large number of attempts.

[32] In the set of random spectra, 40% of the spectra have $\hat{u}_{\rm H_{max}}$ lower than $\hat{u}_\star$ (typical spectra), in 50% of the spectra the condition $\hat{u}_{\rm H_{max}} \approx \hat{u}_\star$ is satisfied (typical spectra), and, finally, 10% of the spectra have high values of $\hat{u}_{\rm H_{max}}$ ($\hat{u}_{\rm H_{max}} > \hat{u}_\star$) (atypical or rare spectra).

[33] As we said, the problem on the wing of the hydrodynamic distribution $f_{\rm H}$ leads us to the analysis of $\hat{u}_{\rm H_{max}}$. Interest in the termination point of the distribution $f_{\rm H}$ stems from the peculiarities of the turbulent line profiles. Because of the fluctuations in the central zone of the profile and the sharp break at $\hat{u}_{\rm H_{max}}$, this profile differs greatly from the Gaussian distribution (10.3). The wing of the spectrum $f_{\rm H}(\hat{u})$ that breaks at $\hat{u}_{\rm H_{max}} = 2$ should be considered short. The fact is that the intensity ratio near $\hat{u}_{\rm H_{max}}$ and at the center is moderately small. If we use formula (10.3) for a rough estimation, this ratio is $\sim e^{-2} \sim 0.1$.

[34] That is, pertaining to the determination of the boundary value $\hat{u}_{\rm H_{max}}$.

[35] The number $N_{\rm mix}$ is small: $N_{\rm mix} \sim 1$–10.

at $\hat{u} \sim \hat{u}_{\mathrm{H_{max}}}$. Because of the gap Δ, its top is not shadowed by the projections of the remaining bumps.

The other position is the position to the left (at $\hat{u} \sim -\hat{u}'_{\mathrm{H_{max}}}$). A group of low (comparable in height) bumps of the function $u(x)$ forms this region of the spectrum.[36] Their shadows (projections) are superimposed on each other. As a result, whereas there is an individual spike on the right, several spikes on the left together form a roughly monotonic segment of the spectrum f_{HT} near $-\hat{u}'_{\mathrm{H_{max}}}$. Thus, the spectrum at the boundaries of range (9.1) for several mixers ($N_{\mathrm{mix}} > 1$) resembles the spectrum shown in Fig. 17 ($N_{\mathrm{mix}} = 1$).

11. TRANSVERSE CORRELATIONS AND THE IMAGE STRUCTURE IN THE PLANE OF THE SKY

11.1. Expansion into a Mesh of Random Three-Dimensional Harmonics

Below, we describe the procedure that was used to calculate the data shown in Figs. 1, 2, and 4–7. We represent the three-dimensional velocity field as a Fourier series:

$$u'(x,y,z;\psi) = N_{\mathrm{mix}}^{1/3} \sum_n \sum_m \sum_k q_{nmk}^{-11/6} \times \cos[2\pi(nx+my+kz)/L + \psi_{nmk}], \quad (11.1)$$

$$q_{nmk} = \sqrt{n^2+m^2+k^2}.$$

In (11.1), u is the x velocity component, the x axis is along the line of sight, y and z are the transverse coordinates, and ψ_{nmk} are the elements of the three-dimensional phase array. Each element of this array is generated by a random number generator independently. The ψ_{nmk} values are limited by the segment $0 < \psi_{nmk} < 2\pi$, which they cover uniformly. The summation in (11.1) is over the cubic mesh points (n,m,k) that fall into the space between the spheres with radii N_{mix} and N_ν. This implies, for example, that the center ($n=0$, $m=0$, $k=0$) is excluded from the summation for $N_{\mathrm{mix}} = 1$.

Using field (11.1), we calculate the mean velocity

$$u_1 = (2l)^{-3} \int_{-l}^{l}\int_{-l}^{l}\int_{-l}^{l} dxdydzu'(x,y,z)$$

of the matter in cube[37] $(2l)^3$, $l \sim L$. Let us write $u_0(x,y,z) = u'(x,y,z) - u_1$. In cube $(2l)^3$, the total x momentum component of the homogeneous (in density) matter that moves with velocity $u_0(x,y,z)$ is equal to zero. We normalize the velocity to the dispersion (cf. formula (4.3)). To compare the 1D (Section 4) and 3D (11.1) velocity representations, it is convenient to use the local dispersion as the unit of velocity:

$$u_{\mathrm{rms}}(y,z) = \left[\int_{-l}^{l} dx[u_0(x,y,z) - u_{av}(y,z)]^2\right]^{1/2}, \quad (11.2)$$

$$u_{av}(y,z) = (2l)^{-1}\int_{-l}^{l} dxu_0(x,y,z).$$

To be definite, we take (11.2) at point $y=0, z=0$ to make the velocity dimensionless. As a result, we obtain

$$u(x,y,z) = u_0(x,y,z)/u_{\mathrm{rms}}(0,0). \quad (11.3)$$

The procedure for calculating the 3D velocity field is defined by formulas (11.1)–(11.3).

11.2. The Spatial Structure of Eddies

The 1D and 3D representations yield statistically equivalent velocity distributions along a fixed line of sight, $y = y_{\mathrm{fix}}$ and $z = z_{\mathrm{fix}}$. Indeed, in contrast to the random phase ψ_{nmk}, the phase $2\pi(my_{\mathrm{fix}} + kz_{\mathrm{fix}})/L$ in formula (11.1) at fixed y_{fix} and z_{fix} may be omitted. By the summation over m and k, we reduce formula (11.1) to formula (4.1).

The representations from Sections 4 and 11.1 are intended to solve two different ranges of questions. Expansion (4.1) is required to analyze the relationships between the distributions $f_{\mathrm{HT}}(\hat{u}) \leftrightarrow u(x)$ and to describe the statistically representative multispike profiles (see Sections 9 and 10). The line profile is determined by the longitudinal hierarchical structure of eddies (the structure along the line of sight).

On the other hand, the eddies are spatial structures. Therefore, the longitudinal and transverse parameters of the velocity field are closely related.[38] Expansion (11.1), which is required to resolve the

[36] It would be more precise to talk about the dips of the function $u(x)$, because $u(x)$ is negative in the segments that correspond to the dips.

[37] Note that $\sim N_\nu^6$ calculations of the function cos are required for an accurate difference calculation of this integral (including the eddies of all sizes up to the viscous scale).

[38] For example, the large-scale eddy that clearly shows up in the velocity u distribution along the x axis necessarily has the corresponding distinct imprint or trace in the y, z plane of the sky.

questions concerning the plane of the sky (see the examples in Figs. 1–7), reflects this fact. We are talking about the 3D probing and change of the profile together with the change in the position of the observation point in the plane of the sky.

11.3. The Pattern in the Presence of Many Independent Mixers

The parameters of the line profile are the moments μ_n (6.3) calculated from the distribution $f_{\rm HT}(\hat{u})$. The moment μ_0 gives the profile normalization to the total number of line photons. If the spatial density distribution of the line-emitting ions n_i and the plasma temperature T are assumed to be uniform, then the moment μ_0 does not depend on coordinates y and z. The next moments ($\mu_n, n \geq 1$) are variable over the plane of the sky. Let us consider the variability of the first moment μ_1. In the part of the cluster uniform in n_i and T, the moment $\mu_1(y,z)$ is proportional to the mean velocity, the line-of-sight momentum $p(y,z)$ (1.5), and the CMB intensity fluctuations $\Delta T_r(y,z)/T_r$ (1.4). It determines the position of the profile center relative to the chosen frame of reference (Sections 1, 2, 11.1).

Consider the problem of profile variation for displacements $\Delta l_\perp$ in the plane of the sky as a function of the turbulence pattern. The most important qualitative parameter of the turbulence is the ratio $N_{\rm mix} = L/L_{\rm mix}$ (Sections 1, 3, 4). There are two cases: with $N_{\rm mix} \sim 1$ and $N_{\rm mix} \gg 1$ (many mixers[39]). Let us first consider the second case. We assume that uncorrelated mixes of size $\sim L_{\rm mix}$ cover a cluster of size L and produce (each) velocity fluctuations with an amplitude $\sim v_{\rm mix} \sim u_{\rm rms}$.

The Kolmogorov (short-wavelength) part of the spectrum $N_{\rm mix} \leq n \leq N_\nu$ responsible for the Kolmogorov velocity scaling $(\Delta u)_{\Delta l} \propto (\Delta l)^{1/3}$ (3.3) on small scales $\Delta l < L_{\rm mix}$ is represented in the Fourier series (4.1) and (11.1). For $N_{\rm mix} \gg 1$, it must be supplemented with the long-wavelength part of the harmonic spectrum $1 \leq n < N_{\rm mix}$. The harmonic expansion then takes the form

$$u(x,y,z)/v_{\rm mix} = N_{\rm mix}^{-1/2} F \sum\sum \sum_{(n,m,k)=1}^{N_{\rm mix}} q_{nmk}^{-1} \times \cos[2\pi(nx+my+kz)/L + \psi_{nmk}] + N_{\rm mix}^{1/3} \sum\sum \sum_{(n,m,k)=N_{\rm mix}}^{\infty} q_{nmk}^{-11/6} \times \cos[2\pi(nx+my+kz)/L + \psi_{nmk}], \quad (11.4)$$

where $1/F \sim \sqrt{\ln N_{\rm mix}}$. In our conditions, F is an insignificant factor of ~ 1 that is omitted below. Its estimate follows from analysis of the sum with random phases $|\sum_{N_1}^{N_2} \exp(i\psi_n)/\sqrt{n}| \sim \sqrt{\ln(N_2/N_1)}$. The line-of-sight velocity distribution $u(x, y_{\rm fix}, z_{\rm fix})$ can be determined from expansion (11.4). Fixing the position $(y,z)_{\rm fix}$ and summing (11.4) over m and k, we obtain

$$u(x)/v_{\rm mix} = N_{\rm mix}^{-1/2} \sum_{n=1}^{N_{\rm mix}-1} C + N_{\rm mix}^{1/3} \sum_{n=N_{\rm mix}}^{\infty} C/n^{1/2+1/3}, \quad (11.5)$$
$$C \equiv \cos(2\pi n x/L + \psi_n).$$

Let us analyze the velocity field specified by the above formulas. Consider the point $(x,y,z)_{\rm fix}$. The right and left boundaries of the summation range ($n \sim N_{\rm mix}$) give the largest contribution to the first and second sums in formulas (11.4) and (11.5), respectively. Therefore, the maximum velocity fluctuation amplitude is $\sim v_{\rm mix}$. The spatial scale of the velocity fluctuations with this amplitude is $\sim L_{\rm mix}$, because these fluctuations are produced by the group of harmonics with wavelengths $\sim L_{\rm mix}$. The correlator $K(|\Delta\mathbf{l}|) = \langle u(\mathbf{r}+\Delta\mathbf{l})u(\mathbf{r})\rangle$ decays on scales $|\Delta\mathbf{l}| > L_{\rm mix}$.

Consider the $(y,z)_{\rm fix}$ ray. The integral of the function $u(x)$ (11.5) that gives the mean velocity or momentum is estimated as $|\int_{-l}^{a} dx u(x)| \sim v_{\rm mix}(L/\sqrt{N_{\rm mix}})\sqrt{(a+l)/L}$. For $a+l > L_{\rm mix}$, the harmonics from the first (long-wavelength) sum in formula (11.5) with wavelengths on the order of the length of the integration segment ($\lambda \sim (a+l)$) give the largest contribution to this estimate. For $a+l \sim L$, we obtain[40] $|\int_{-l}^{a} dx u(x)| \sim v_{\rm mix}(L/\sqrt{N_{\rm mix}})$; cf. $\int_{-l}^{a} dx|u(x)| \sim v_{\rm mix} L$. Thus, as the parameter $N_{\rm mix}$ increases, the CMB fluctuation amplitude (1.4) related to the kinematic SZ-effect decreases.

Consider two adjacent lines of sight parallel to the x axis. Imagine a chain of eddies with a size $\sim L_{\rm mix}$ threaded on these lines of sight. Let the separation between the lines of sight be larger than $L_{\rm mix}$. The function

$$p(y,z) = (2l)^{-1} \int_{-l}^{l} dx u(x,y,z) \quad (11.6)$$

changes sign in the case of a displacement in the plane of the sky by a distance $\sim L_{\rm mix}$, because the

[39] Many relatively small strongly gravitationally bound structures "furrow" the cluster.

[40] This estimate was used in Section 1.

above correlator $K(|\Delta\mathbf{l}|)$ decays at these distances. To sum up, we conclude that, first, the amplitude the variations in the function $p(y,z) \sim v_{\rm mix}/\sqrt{N_{\rm mix}}$, and, second, a spatial scale $\sim L_{\rm mix}$ is associated with this function.

11.4. The Fractality of Intensity Fluctuations in the Kinematic SZ- Effect

Consider the small-scale functions ($\Delta l_\perp < L_{\rm mix}$) of p (11.6) for $N_{\rm mix} \sim 1$. Let there be two lines of sight separated by a distance $\Delta l_\perp$. Since the plane of the sky is isotropic in the case of small displacements, we may choose the y and z axes so that the displacement $\Delta l_\perp$ is directed along the y axis. Let us estimate the difference $\Delta p(\Delta l_\perp) = |p(\Delta l_\perp, 0) - p(0,0)|$ by using formula (11.4). We substitute $z = 0$ into expansion (11.4) and sum it over k. Since $N_{\rm mix} \sim 1$, the second sum in formula (11.4) is dominant. Our calculations yield the expression

$$u(x,y)/v_{\rm mix} = N_{\rm mix}^{1/3} \sum \sum_{(n+m)\geq N_{\rm mix}}^{\infty} \times \cos[2\pi(nx+my)/L + \psi_{nm}]/q_{nm}^{1+1/3}, \quad (11.7)$$

where $q_{nm} = \sqrt{n^2+m^2}$.

According what we said above, $p(\Delta l_\perp, 0) = (2l)^{-1}\int_{-l}^{l} dx u(x, \Delta l_\perp)$, where the function u is given by formula (11.7), $l \sim L$. Taking this integral and setting up the difference, we obtain

$$\Delta p(\Delta l_\perp) \sim v_{\rm mix} N_{\rm mix}^{1/3} | \times \sum \sum_{(n+m)\geq N_{\rm mix}}^{\infty} [\sin(2\pi m \Delta l_\perp/L + \psi_{nm}) - \sin\psi_{nm}]/(n q_{nm}^{4/3})|. \quad (11.8)$$

Consider the sum

$$I(M,n) = \sum_m \frac{\sin(2\pi m/M + \psi) - \sin\psi}{n(n^2+m^2)^{2/3}} \quad (11.9)$$

over m in formula (11.8), $\psi \equiv \psi_{nm}$. It depends on two parameters: n and $M = L/\Delta l_\perp$. We will separately consider the cases with $n \ll M$, $n \sim M$, and $n \gg M$.

As the index n increases, the terms of sum (11.8) decrease in absolute value no more slowly than $1/n$. Therefore, given the random phase, the terms with $n \sim N_{\rm mix} \sim 1$ mainly contribute to sum (11.8).

Consequently, only the case with $n \ll M$ must be considered when analyzing sum (11.9). We break down sum (11.9) into three sums by the indices $m \gg M$, $m \sim M$, and $m \ll M$. For $m > M$, the contributions from the two sines of the same order to sum (11.9) are, respectively,

$$I(M,n) \sim \sum_m \sin\psi_{nm}/(nm^{4/3}), \quad (11.10)$$

$$I(M,n) \sim \sin\psi_n M^{-5/6}/n,$$

where ψ_n is the new random phase.

For $m \ll M$, the difference between the arguments of the sines in formula (11.9) is small. Expanding (11.9) in this difference and retaining the linear term, we reduce expression (11.9) to

$$I(M,n) \sim \frac{1}{M}\sum_m \frac{m\sin\psi_{nm}}{n(n^2+m^2)^{2/3}} \sim \frac{1}{nM}\sum_m \frac{\sin\psi_{nm}}{m^{1/3}}.$$

The principal terms in this sum are those with large numbers $m \sim M$, because the sum diverges $\propto m^{1/6}$. Thus, we conclude that sum (11.8) is determined by contribution (11.10). The summation over n in (11.8) finally yields

$$\Delta p(\Delta l_\perp) \sim v_{\rm mix} N_{\rm mix}^{1/3}/M^{5/6} \sim v_{\rm mix}(\Delta l_\perp/L)^{5/6}.$$

Above, we rigorously derived the important law (1.8) of the short-scale CMB intensity fluctuation scaling for the kinematic SZ effect.

12. THE COMBINED EFFECT OF HYDRODYNAMIC, THERMAL, AND LORENTZ BROADENINGS

Let us take into account the effects related to the finite lifetime of the electron in an excited state (intrinsic or radiation broadening $\Delta\nu_{\rm R}$). In the hot rarefied intergalactic plasma of a cluster, the intrinsic line widths are small compared to the Doppler shifts $\Delta\nu_{\rm DT} = \nu_0\sqrt{2kT/m_i}/c$ and $\Delta\nu_{\rm DH} = \nu_0 u_{\rm rms}/c$, where ν_0 is the frequency of the profile center. Therefore, the shift $\Delta\nu_{\rm R}$ affects only the periphery of the profile (line wings) as the radiation intensity decreases by several orders of magnitude (see below). The corresponding effects are significant for intense lines, when the profile wings rise above the background (see Fig. 1). Since the intrinsic broadening is peripheral, it would be appropriate to analyze it following the above study of the central hydrodynamic part of the profile.

A radiator at rest in the laboratory frame of reference (the velocity of the cluster center was subtracted; Sections 1 and 2) sends a radiation line with a Lorentz profile (Ivanov 1973):

$$f_L(\nu) = \frac{\pi^{-1}\Delta\nu_{\rm R}}{(\nu-\nu_0)^2 + \Delta\nu_{\rm R}^2}, \qquad \int f_L d\nu = 1. \quad (12.1)$$

The hydrodynamic and thermal motions of ions lead to a Doppler frequency shift $\nu_0' = \nu_0 - \nu_0 u/c$, where u is the velocity component of the radiator along the x line of sight (Section 2). When the radiator moves, the frequency ν_0' replaces ν_0 in formula (12.1).

Hydrodynamic motions cause the parts of the cluster to be distributed in macroscopic velocities u_H. The fraction $f_\mathrm{H}(\hat{u}_\mathrm{H})d\hat{u}_\mathrm{H}$ of the entire radiating mass on the line of sight moves in the velocity range $[u_\mathrm{H}, u_\mathrm{H} + du_\mathrm{H}]$, where $\hat{u}_\mathrm{H} = u_\mathrm{H}/u_\mathrm{rms}$ is a dimensionless velocity. We take into account the Maxwellian broadening in the isothermal case where all parts of the cluster have the same temperature T. The fraction

$$[f_\mathrm{H}(\hat{u}_\mathrm{H})d\hat{u}_\mathrm{H}](\sqrt{2\pi}\sqrt{kT/m_i})^{-1} \times \exp[-m_i(u-u_\mathrm{H})^2/(2kT)]du$$

of $f_\mathrm{H}d\hat{u}_\mathrm{H}$ moves with velocity u relative to the observer. Therefore, the profile can be determined from the turbulent velocity distribution f_H by using the double integral

$$f_\mathrm{HTL}(\nu) = \frac{\Delta\nu_\mathrm{R}}{\sqrt{2\pi^3}\sqrt{kT/m_i}} \int_{-\infty}^{\infty}\int_{-\infty}^{\infty} d\hat{u}_\mathrm{H} \times du \frac{f_\mathrm{H}(\hat{u}_\mathrm{H})\exp[-m_i(u-u_\mathrm{H})^2/(2kT)]}{(\nu-\nu_0+\nu_0 u/c)^2+\Delta\nu_\mathrm{R}^2}, \quad (12.2)$$

where the subscripts H, T, and L denote the turbulent, Maxwellian, and Lorentz shifts, respectively.

It is easy to see that in the limit $u_\mathrm{rms} \to 0$, the integral over $d\hat{u}_\mathrm{H}$ can be taken, and expression (12.2) transformed to the Voigt function, the definition of which can be found in the book by Ivanov (1973). The Voight function describes the thermal–radiation profile without hydrodynamic broadening. In dimensionless variables, integral (12.2) takes the form

$$f'_\mathrm{HTL}(x;\mathrm{Ma}_i,a) = \frac{a\mathrm{Ma}_i}{\sqrt{2\pi^3}(\Delta\nu_\mathrm{DT})}\int\int dy \times dz \frac{f_\mathrm{H}(z)\exp[-(\mathrm{Ma}_i^2/2)(y-z)^2]}{(\mathrm{Ma}_i^2/2)(x-y)^2+a^2}, \quad (12.3)$$

$$x = -\frac{\nu-\nu_0}{\Delta\nu_\mathrm{DH}} = \frac{\nu-\nu_0}{\nu_0 u_\mathrm{rms}}c, \quad y = \frac{u}{u_\mathrm{rms}}, \quad (12.4)$$
$$z = \hat{u}_\mathrm{H} = \frac{u_\mathrm{H}}{u_\mathrm{rms}}, \quad a = \frac{\Delta\nu_\mathrm{R}}{\Delta\nu_\mathrm{DT}}.$$

As we see, profile (12.3) depends on two parameters, Ma_i and a. In contrast, profile (8.1) depends on one parameter.

At low values of a or $1/\mathrm{Ma}_i$, the functions

$$\frac{\mathrm{Ma}_i}{\sqrt{2}\pi a[(\mathrm{Ma}_i^2/2a^2)x^2+1]}, \quad \frac{\mathrm{Ma}_i}{\sqrt{2\pi}}\exp\left(-\frac{\mathrm{Ma}_i^2x^2}{2}\right)$$

tend to $\delta(x)$. If the radiation width is small [$\Delta\nu_\mathrm{R} \to 0, a \to 0$], then instead of (12.3), we return to the Doppler profile (8.1), with the difference that the function $f_\mathrm{HT}(u)$ in formula (8.1) gives the distribution per unit velocity, while the related formulas (12.1) and (12.3) give the distribution per unit frequency. For this reason, in the limit $a \to 0$, the factor c/ν_0 that distinguishes this limit from expression (8.1) emerges in formula (12.3). Note also that the signs of the $(\nu-\nu_0)/\Delta\nu_\mathrm{DH}$ frequency axis and the y or z velocity axis are opposite. The spatial x axis runs from the observer toward the cluster (Section 2). Therefore, positive velocities (the radiator recedes from the observer, y, $z > 0$), according to the Doppler formula, cause the frequency $\nu < \nu_0$ to decrease. To compensate for the difference in sign, we denoted $x = -(\nu-\nu_0)/(\Delta\nu_\mathrm{DH})$ when making the frequency in (12.4) dimensionless.

We now let $\mathrm{Ma}_i \to \infty$, because $\sqrt{kT/m_i} \to 0$. In place of (12.3), we then obtain the hydrodynamic–radiation profile

$$f_\mathrm{HR}(x;a_\mathrm{H}) = \frac{a_\mathrm{H}}{\pi(\Delta\nu_\mathrm{DH})}\int dz \frac{f_\mathrm{H}(z)}{(x-z)^2+a_\mathrm{H}^2},$$
$$a_\mathrm{H} = \frac{\Delta\nu_\mathrm{R}}{\Delta\nu_\mathrm{DH}} = \frac{\sqrt{2}a}{\mathrm{Ma}_i}.$$

In our calculations below, we use the double integral in a form that is more convenient for calculations:

$$f_\mathrm{HTL}(x) = \frac{\mathrm{Ma}_i}{\sqrt{2\pi}}\frac{a_\mathrm{H}}{\pi} \times \int\int dydz \frac{f_\mathrm{H}(z)\exp[-(\mathrm{Ma}_i^2/2)(y-z)^2]}{(x-y)^2+a_\mathrm{H}^2} = \frac{a_\mathrm{H}}{\pi}\int dy \frac{f_\mathrm{HT}(y)}{(x-y)^2+a_\mathrm{H}^2}. \quad (12.5)$$

Function (12.5) is dimensionless. It differs from function (12.3) by the factor $\Delta\nu_\mathrm{DH}$. Similarly, the function $f_\mathrm{HT}(y)$ in (12.5) differs from (8.1) by the factor u_rms. As we see from (12.5), the double integral can be taken in two steps. At the first step, the hydrodynamic distribution is folded with the Maxwellian distribution, and the profile f_HT (8.1) is determined. At the second step, the function f_HT is folded with the Lorentz distribution.

13. THE THREE-ZONE LINE STRUCTURE

Because of the qualitative difference between the functional asymptotic behaviors of the distributions f_L, f_M, and f_H on the periphery of the profile and because of the difference between the widths, the line separates into three characteristic zones. The central zone is the turbulent–thermal zone HT. It is followed by zone T of sharp thermal decrease as one recedes

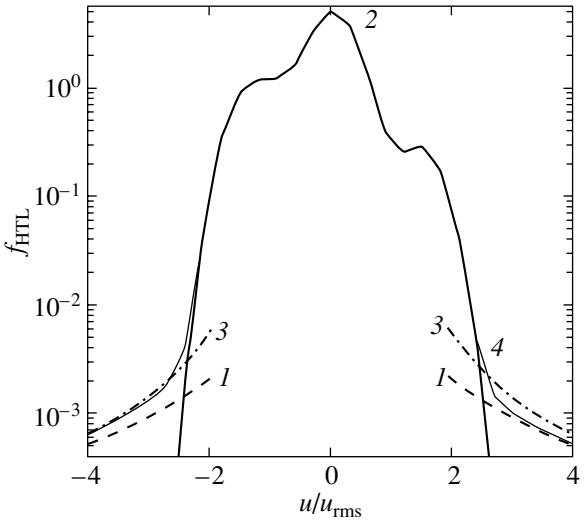

Fig. 18. Fe XXV w-line profile: *1* and *3*—the first and third approximations of (13.3) for the radiation wings, *2*—$f_{\rm HT}(\hat{u})$, *4*—$f_{\rm HTL}(\hat{u})$.

from the center in frequency. Finally, the profile wings (zone L) is formed under the effect of intrinsic broadening (12.1). Figures 1 and 18 show a typical sample spectrum with a broad central zone HT, a steep thermal break T, and a Lorentz pedestal L (an example of the helium-like Fe XXV permitted line). Let us first give the parameters that lead to this situation and then discuss the peculiarities related to the functional behavior. Consider the Fe XXV w- and z-lines. The photon energies and intrinsic widths of these lines are $h\nu_0 = 6.71$ keV, $\Delta\nu_{\rm R} = 0.38 \times 10^{14}$ Hz (w-line) and $h\nu_0 = 6.64$ keV, $\Delta\nu_{\rm R} = 1.87 \times 10^7$ Hz (z-line) (Janev *et al.* 1985). In a plasma with $kT = 3$ keV and $u_{\rm rms} = 300$ km s^{-1}, the turbulent, thermal, and particularly radiation broadenings differ significantly: $\Delta\nu_{\rm R}c/\nu_0 = 7$ km s^{-1} for the w-line and 0.3 cm s^{-1} for the z-line; cf. $\sqrt{kT/m_i} = 72$ km s^{-1} and $u_{\rm rms} = 300$ km s^{-1}, here m_i is the iron atomic mass. Since $\Delta\nu_{\rm R}$ is small, the ratio of the intensities at the center and at the transition point to the Lorentz wing is large.

Since the width $\Delta\nu_{\rm R}$ is small, the central zone is satisfactorily described by the function $f_{\rm HT}$ (8.1) (i.e., the Lorentz broadening is negligible here). For $N_{\rm mix} \sim 1$ (large-scale turbulence), the wings of the function $f_{\rm H}$ differ greatly from the Gaussian wings (the allowable velocities are strictly limited; see Fig. 1 and Section 10). The transition between zones HT and T occurs near the point $\hat{u}_{\rm H_{max}}$ at which the hydrodynamic distribution $f_{\rm H}(\hat{u}_{\rm H})$ becomes zero (see Fig. 18). At fixed boundaries $N_{\rm mix}$ and N_ν of the Kolmogorov range, $\hat{u}_{\rm H_{max}}$ vary statistically with random phases ψ_n and ψ_{nmk} (4.1), (11.1). In the numerous realizations considered above, $\hat{u}_{\rm H_{max}} = 1.9$–$2.7$ are typical values. The function $f_{\rm H}(\hat{u}_{\rm H})$ (the vanishing law) in the close neighborhood of the limit $\hat{u}_{\rm H_{max}}$ is determined by the number N_ν. Deriving this function is a separate statistical problem. In the conditions under consideration, the temperature smooths out this function. Note that at finite values of N_ν, the "cold" distribution $f_{\rm H}(\hat{u}_{\rm H})$ always has a root singularity at the edge $\hat{u}_{\rm H_{max}}$. For $N_\nu \sim 1$, this question was considered in Section 9. Of interest is the function $f_{\rm H}(\hat{u}_{\rm H})$ for $N_\nu = \infty$.

The width of the transition region T, which separates the central zone from the radiation wing, is on the order of the thermal velocity. In the dimensionless variables used in Fig. 18 (the normalization to the hydrodynamic velocity $u_{\rm rms}$; see Subsection 11.1), it is $\sim 1/{\rm Ma}_i$. Let us analytically estimate the profile in the transition region T. We denote the point that separates the transition region T and the Lorentz wing L by $\hat{u}_{\rm TL}$. In the inner (relative to the wings L) segment $-\hat{u}'_{\rm TL} < x < \hat{u}_{\rm TL}$, the shape of the profile is determined by integral (8.1). The function $f_{\rm H}(z)$ under integral (8.1) is nonzero in the band $-\hat{u}'_{\rm H_{max}} < z < \hat{u}_{\rm H_{max}}$, where the limits $\hat{u}_{\rm H_{max}}$ and $\hat{u}'_{\rm H_{max}}$ define the maximum positive and negative hydrodynamic velocities. Let us analyze integral (8.1) beyond the boundary of this band (i.e., when $x > \hat{u}_{\rm H_{max}}$). Hence follows the sought-for analytical estimate of the function $f_{\rm T}(x) = C(x)\exp[-({\rm Ma}_i^2/2)(x - \hat{u}_{\rm H_{max}})^2]$ in the interval $\hat{u}_{\rm H_{max}} < x < \hat{u}_{\rm TL}$, where $C(x)$ is a "sluggish" function of the argument x. The latter can be roughly substituted with a constant C in the narrow interval that corresponds to region T. We see that the function $f_{\rm T}(x)$ rapidly (the number ${\rm Ma}_i$ is large) decays when $x > \hat{u}_{\rm H_{max}}$. The constant C can be calculated by joining the distributions $f_{\rm HT}(x)$ and $f_{\rm T}(x)$ at the point $\hat{u}_{\rm H_{max}}$. We approximate the function $f_{\rm HT}$ by the Gaussian distribution

$$\ln f_{\rm HT} \approx -[\ln(2\pi) + x^2]/2. \qquad (13.1)$$

Writing the joining condition, we obtain the thermal parabola

$$\ln f_{\rm T} \approx -\frac{\ln(2\pi)}{2} - \frac{\hat{u}^2_{\rm H_{max}}}{2} - \frac{{\rm Ma}_i^2}{2}(x - \hat{u}_{\rm H_{max}})^2. \qquad (13.2)$$

Let us write out the Lorentz asymptotics. Consider the double integral (12.5) at large x. The integral over y in (12.5) can be broken down into two terms, I_1 and I_2. The integral $I_1(x)$ is concentrated in a small segment of width $\sim a_{\rm H}$ near the point $y = x$. The other integral (I_2) is taken over the entire y axis, except the neighborhood of the point $y = x$ that

entered into I_1. Since the parameter a_H is small, we may disregard the term a_H^2 in the denominator of the integrand (in the Lorentz function) in the integral I_2. The integral $I_1(x)$ gives the above functions $f_{HT}(x)$ (8.1) for $-\hat{u}'_{H_{max}} < x < \hat{u}_{H_{max}}$ and $f_T(x)$ (8.1) for $x > \hat{u}_{H_{max}}$. The function $f_T(x)$ (8.1) with the approximate asymptotics (13.2) exists at any $x > \hat{u}_{H_{max}}$, including the Lorentz wing for $x > x_{TL}$. For $x > \hat{u}_{TL}$, the function $I_1(x)$ is small compared to $I_2(x)$. In contrast, $I_2 \ll I_1$ inside the segment $\hat{u}'_{TL} < x < \hat{u}_{TL}$.

Let us consider the integral $I_2(x)$ at $x \gg \hat{u}_{TL}$. Expanding the denominator $(x-y)^{-2}$ into a power series of y/x, we obtain from expression (12.5)

$$I_2(x) = \frac{\mathrm{Ma}_i}{\sqrt{2\pi}}\frac{a_H}{\pi}(x^{-2}\int\int f_H \exp + 2x^{-3} \times \int\int y f_H \exp + 3x^{-4}\int\int y^2 f_H \exp + \ldots)$$
$$\approx (a_H/\pi)(1/x^2 + 3/x^4 + 15/x^6 + O(x^{-8})), \quad (13.3)$$
$$\int\int f_H \exp \equiv \int\int dy dz f_H(z) \times \exp[-(\mathrm{Ma}_i^2/2)(y-z)^2].$$

The Gaussian approximation (10.3) of the hydrodynamic velocity distribution f_H may be used to approximately calculate the integrals $b_n = (\mathrm{Ma}_i/\sqrt{2\pi})\int\int y^n f_H \exp$ in the numerators of the terms of series (13.3). In this approximation, the odd coefficients b_n become zero, $b_0 = 1$, $b_2 = 1 + 1/\mathrm{Ma}_i^2 \approx 1$ for $\mathrm{Ma}_i \gg 1$, $b_4 = 3(1 + 1/\mathrm{Ma}_i^2)^2 \approx 3$. The general formula for these coefficients is

$$b_n = 2^{n/2}\Gamma(n/2)(1 + 1/\mathrm{Ma}_i^2)^{(n-1)/2}/\sqrt{2\pi},$$

where $\Gamma(n/2)$ is the gamma function (Vinogradov 1979). Since the real distribution f_H is asymmetric relative to the zero velocity $u_H = 0$, the odd coefficients take on relatively low values that we disregarded in estimate (13.3). Curves *1* and *3* in Fig. 18 represent one and three terms of expansion (13.3), respectively. A comparison of these curves with the thin curve *4* (the exact calculation of integral (12.5)) shows that the influence of the hydrodynamic asymmetry is significant.

The dependence $I_2(x)$ (13.3) approximates the line profile $f_L(x)$ in the region of the radiation wing. The intersection of the approximate asymptotics (13.2) and (13.3) gives an estimate of the position of the point $\hat{u}_{TL}(\mathrm{Ma}_i, a_H)$. Adding the second and third expansion terms in (13.3) appreciably improves the analytical approximation near the point of intersection $\hat{u}_{TL}$ (see Fig. 18). The transition between zones T and L is sharp for the z-line, because the width $\Delta\nu_R$ is extremely small.

An important phenomenon is associated with the break of the wings of the hydrodynamic distribution $f_H(\hat{u}_H)$ for large-scale turbulence ($N_{mix} \sim 1$). This phenomenon (the first cause) gives rise to a three-zone profile with zone T of a sharp decrease in intensity at high values of Ma_i (the second cause). If the distribution $f_H(\hat{u}_H)$ were Gaussian with the wings extending to infinity, then, according to (8.1), the profile f_{HT} would also be Gaussian with infinite wings. Indeed,

$$f_{HT}(x) = \frac{\mathrm{Ma}_i}{\sqrt{2\pi}}\int_{-\infty}^{\infty} dy \frac{\exp(-y^2/2)}{\sqrt{2\pi}} \times \exp[-(\mathrm{Ma}_i^2/2)(x-y)^2]$$
$$= \frac{(2\pi)^{-1/2}}{\sqrt{1 + 1/\mathrm{Ma}_i^2}}\exp\left(-\frac{x^2}{2(1 + 1/\mathrm{Ma}_i^2)}\right). \quad (13.4)$$

Distribution (13.4) has the square of the dispersion equal to the sum of the squares of the hydrodynamic and thermal dispersions. The corresponding parabola is shown in Fig. 1. Its intersection with the Lorentz wings is much farther than its intersection with the three-zone curve. As we see, there is a qualitative difference between between the non-Gaussian (three-zone structure) and Gaussian (two-zone structure) hydrodynamic distributions f_H. In the Gaussian case, zone T of sharp decrease disappears, while the point $\hat{u}_{TL}$ moves far away.

Just as in the case of the Voigt function (Ivanov 1973), an estimate for the position of the point of intersection of the parabola with total dispersion (13.4) with the Lorentz wing follows from the equation

$$\frac{(2\pi)^{-1/2}}{\sqrt{1 + 1/\mathrm{Ma}_i^2}}\exp\left(-\frac{x^2}{2(1 + 1/\mathrm{Ma}_i^2)}\right) = \frac{a_H}{\pi x^2}.$$

For the three-zone structure, the situation is distinctly different. The width of zone T on the $\hat{u}$ axis is on the order of $1/\mathrm{Ma}_i$. At high values of Ma_i, this width is small compared to $\hat{u}_{H_{max}}$. Therefore, the function $f_{HT}(\hat{u})$ (8.1) and the Lorentz wing (13.3) (see Figs. 1 and 18) intersect approximately at $\hat{u}_{TL} \approx \hat{u}_{H_{max}}$. Hence, the ratio of the intensities at the point of intersection and at the line center is

$$f(\hat{u}_{TL})/f(0) \approx \sqrt{2/\pi}a_H/\hat{u}_{H_{max}}^2.$$

It would be of interest to experimentally determine the point at which the profile reaches the Lorentz asymptotics (Figs. 1 and 18). This would allow the maximum hydrodynamic velocity to be estimated.

CONCLUSIONS

Our calculations show that there must be large-scale turbulence with characteristic sizes $L_{\rm mix} > 0.1L$ for the deviations from the Gaussian distribution to be noticeable. It follows from our analysis of the temperature effect that the distribution remains essentially non-Gaussian even when the thermal smoothing of the line profile is taken into account. We have constructed a theory for the turbulent broadening of the line obtained by pointing an X-ray telescope at a fixed point in the cluster plane of the sky. A two-dimensional map in the plane of the sky for the dependence on the position of the point in the plane of main deviations from the Gaussian distribution must contain information about the localization of turbulence spots and the characteristic turbulence scale. Thus, we showed that valuable information about the turbulent motions of intergalactic plasma inside clusters of galaxies can be extracted from analysis of X-ray lines with an accuracy $\sim$1–2 eV (3D probing of the state after a cluster merger).

ACKNOWLEDGMENTS

We are grateful to M.V. Burnashev, S.V. Molkov, K. Mitsuda, and S.Yu. Sazonov for their valuable discussions. N.A. Inogamov wishes to thank A.M. Oparin for his valuable help with the numerical calculations and the Russian Foundation for Basic Research (project no. 02-02-17499) as well.

REFERENCES

1. E. Churazov, M. Brueggen, C. R. Kaiser, *et al.*, Astrophys. J. **554**, 261 (2001).
2. E. Churazov, R. Sunyaev, W. Forman, and H. Boehringer, Mon. Not. R. Astron. Soc. **332**, 729 (2002).
3. E. Churazov, W. Forman, C. Jones, *et al.*, Mon. Not. R. Astron. Soc. (2003, in press); astro-ph/0309427.
4. A. C. Fabian, J. S. Sanders, C. S. Crawford, *et al.*, Mon. Not. R. Astron. Soc. **344**, L48 (2003).
5. C. S. Frenk, S. D. M. White, P. Bode, *et al.*, Astrophys. J. **525**, 554 (1999).
6. J. P. Ge and F. N. Owen, Astron. J. **105**, 778 (1993).
7. M. R. Gilfanov, R. A. Sunyaev, and E. M. Churazov, Sov. Astron. Lett. **13**, 3 (1987).
8. V. V. Ivanov, *Radiative Transfer and the Spectra of Celestial Bodies* (Nat. Bureau of Standards, Washington, 1973), Spec. Publ., no. 385.
9. R. K. Janev, L. P. Presnyakov, and V. P. Shevelko, *Physics of Highly Charged Ions. Springer Series in Electrophysics* (Springer, Berlin, 1985), Vol. 13.
10. A. N. Kolmogorov, Dokl. Akad. Nauk SSSR **30**, 299 (1941).
11. L. D. Landau and E. M. Lifshitz, *Hydrodynamics* (Nauka, Moscow, 1986).
12. *Mathematical Encyclopaedia,* Ed. by I. M. Vinogradov (Sov. Éntsiklopediya, Moscow, 1979), Vol. 2.
13. A. S. Monin and A. M. Yaglom, *Statistical Hydromechanics* (Nauka, Moscow, 1965).
14. D. Nagai, A. Kravtsov, and A. Kosowsky, Astrophys. J. **587**, 524 (2003).
15. M. L. Norman and G. L. Bryan, *The Radio Galaxy Messier 87,* Ed. by H.-J. Roeser and K. Meisenheimer (Springer, Berlin, 1999), Lect. Notes Phys. **530**, ISSN0075-8450.
16. F. S. Porter and K. Mitsuda (Astro-E2/XRS Collab.), *American Astron. Soc. HEAD Meeting no. 35, no. 33.05* (2003).
17. M. N. Rosenbluth and R. Z. Sagdeev, *Handbook of Plasma Physics* (North-Holland, Amsterdam, 1983).
18. R. K. Smith, N. S. Brickhouse, D. A. Liedahl, and J. C. Raymond, Astrophys. J. **556**, L91 (2001).
19. R. A. Sunyaev, Pis'ma Astron. Zh. **3**, 491 (1977) [Sov. Astron. Lett. **3**, 268 (1977)].
20. R. A. Sunyaev and Ya. B. Zeldovich, Astrophys. Space Sci. **7**, 3 (1970).
21. R. A. Sunyaev and Ya. B. Zeldovich, Mon. Not. R. Astron. Soc. **190**, 413 (1980).
22. R. Sunyaev, M. Norman, and G. Brian, Pis'ma Astron. Zh. **29**, 883 (2003) [Astron. Lett. **29**, 783 (2003)].

Translated by V. Astakhov

Astronomy Letters, Vol. 29, No. 12, 2003, pp. 825–830. Translated from Pis'ma v Astronomicheskiĭ Zhurnal, Vol. 29, No. 12, 2003, pp. 927–933.

Rotation Curves and Mass Distributions in Flat Self-Gravitating Disks

N. R. Sibgatullin[1,2*], A. A. Garcia[2], and V. S. Manko[2]

[1] *Moscow State University, Vorob'evy gory, Moscow, 119992 Russia*

[2] *Center for Modern Research, National Polytechnical Institute (CINVESTAV-IPN), Mexico*

Received May 6, 2003

Abstract—We have developed a new approach that allows the surface-density distribution in flat finite-radius galactic disk models to be reconstructed from an arbitrary smooth angular-velocity distribution. Upper limits for the disk mass and radius are shown to exist for a wide class of rotation curves analytically extended to the unseen part of the disk. © *2003 MAIK "Nauka/Interperiodica"*.

Key words: *rotation curves, galactic disks, surface density.*

The rotation curves of spiral galaxies yield direct information about the gravitational potential distribution in the part of the galactic disk from where photons with statistically significant Doppler line shifts can be recorded. Hα, H I, and CO measurements made it possible to construct the rotation curves for our Galaxy and neighboring galaxies (see the early reviews by de Vaucouleurs and Freeman 1972; Burbidge and Burbidge 1975; van der Kruit and Allen 1978). An improved technique for measurements and statistical data analysis allowed the rotation curves to be constructed at much larger galactocentric distances and the discovery of rotation curves with non-Keplerian or growing tails (van der Kruit and Allen 1978; Binney and Tremaine 1987; Binney and Merrifield 1998; Sofue and Rubin 2001; and Persic *et al.* 1996). The first galactic disk models were based on the concepts of ellipsoidal layers between confocal spheroids (homeoids) (see, e.g., Babcock 1939; Burbidge *et al.* 1960; and Schmidt 1957). Brandt (1960) and Brandt and Belton (1962) let the eccentricity of homoeoids tend to zero and, as a result, obtained flat infinite-radius disks in the $z = 0$ plane. They suggested special rotation curves with Keplerian asymptotic behavior to describe M31 and NGC5055 and numerically calculated the corresponding surface-density distribution in the galactic disk. Toomre (1963) developed a different approach. This author derived a formula for the surface-density distribution in an infinite disk with an arbitrary rotation curve. He also considered a new class of rotation curves with Keplerian asymptotic behavior and analytically calculated the corresponding density distributions. From a mathematical point of view, the boundary conditions of the Neumann problem for the Laplace equation in half-space in these papers were expressed in terms of the boundary conditions of the Dirichlet problem.

Mathematically, the problem of determining the surface density from a given gravitational potential distribution in the disk is equivalent to the classical electrostatic problem of determining the surface-density distribution of electric charge from a given electrostatic potential distribution in a disk. This problem was solved in 1873 by Weber in the special case of a constant potential and in 1881 by Beltrami in the general case. Since then, many authors have turned to the solution of this electrostatic problem and suggested their original methods (Lebedev 1948, 1966; Titchmarsh 1948; Heins and MacCamy 1958; Sneddon 1960); the corresponding references can be found in the book of problems on mathematical physics by Lebedev (1965) and in the monograph by Sneddon (1966); note that the method by Heins and Maccemi leads to a solution of the problem in the form by Lebedev (1948)). Previously (Sibgatullin *et al.* 2003), we solved the problem of reconstructing the surface density from a given rotation curve for infinite flat galactic disks with a central black hole.

Kuzmin (1956) and, subsequently, Mestel (1963) emphasized that highly flattened galaxies (beginning from S_c according to the Hubble classification, when the influence of the spherical component may be disregarded) could be modeled by self-gravitating flat disks of *finite* radius R. Mestel considered two limiting cases: rigid rotation and a model with a constant linear velocity. Analytical special cases in self-gravitating disk models were found by Hunter (1963) and Morgan and Morgan (1969). The applicability of thin self-gravitating circular disk models to galactic disks was discussed by Kuzmin (1956), Kiladze (1958), Bisnovatyi-Kogan and Blinnikov (1972),

*E-mail: sibgat@mech.math.msu.su

1063-7737/03/2912-0825$24.00

Morozov and Fridman (1973), Polyachenko and Fridman (1976), and Kutuzov and Osipkov (1988).

In our paper, we suggest a new method for reconstructing the surface-density distribution in a self-gravitating finite-radius disk for an arbitrary smooth angular-velocity distribution in the disk. The solution of the problem was obtained in a much simpler form than that found by the above authors. The derived formula for the density distribution in the form of a single integral generalizes the formula by Toomre (1963) for infinite disks to finite-radius disks and is also simple. We have derived a formula for the mass of a finite disk. The following three situations can be encountered in principle when extrapolating the rotation curve to the nonradiating part of the disk. (i) As the radius of the disk increases indefinitely, its mass tends to a certain constant value. Such rotation curves have Keplerian "tails." (ii) The disk mass increases infinitely. In particular, the rotation curves with a finite limit of the linear velocity as the radius increases has this property. (iii) The disk radius cannot exceed a certain value R_*. Formally, this case corresponds to maximum mass at $R = R_*$ and negative densities near the outer disk radius at $R > R_*$. Case (iii) has not been studied previously, and in our paper we give examples of such rotation curves. It has an analogy in the theory of barotropic models for neutron stars with maximum mass (a statistical stability criterion).

Like the authors of classic studies (Brandt 1960; Brandt and Belton 1962; Toomre 1963; and Mestel 1963), we strongly idealize the real spiral galaxies by assuming that they are flat, axisymmetric, and infinitely thin disks in which the noncircular motions and the out-of-disk spheroidal component are disregarded. In addition, the gravitational fields of hidden (dark) mass have the same effect on the rotation curves as does the gravitational field of luminous mass. A reliable mechanism for separating the contributions of dark and luminous masses to the rotation curve is not yet known (Binney and Tremaine 1987; Burstein and Rubin 1985; Persic and Salucci 1988). However, the authors assume that maximum mass at a finite radius of a spiral galaxy also exists for more realistic models. An exact analytical solution of the idealized problem can also be used to analyze the results of detailed numerical calculations of such realistic models.

Our approach to the problem of Newtonian self-gravitating disks is based on a new representation of the gravitational potential of a disk with radius R. We take it in the form

$$\Phi(\rho, z) = \sqrt{\tilde{\rho}^2 + \tilde{z}^2}\,\tilde{\Phi}(\tilde{\rho}, \tilde{z}), \qquad (1)$$

where the auxiliary spatial variables $\tilde{\rho}$ and $\tilde{z}$ are related to the ρ and z cylindrical coordinates by

$$\tilde{\rho} = R^2\rho/r^2, \quad \tilde{z} = R^2 z/r^2, \quad r^2 \equiv \rho^2 + z^2; \quad (2)$$

the potential $\tilde{\Phi}$ is defined as

$$\tilde{\Phi}(\tilde{\rho}, \tilde{z}) = \frac{1}{2\pi^2}\int_0^\pi d\theta \int_R^\infty \ln[(s - \tilde{\rho}\cos\theta)^2 + \tilde{z}^2]\alpha(s)ds. \qquad (3)$$

Here, $\alpha(s)$ is a real function that has the meaning of the density of source distribution. Owing to the analytical properties of the logarithmic function on the complex plane, the Laplace equation for the gravitational potential of the disk holds everywhere outside the disk. In addition, the function $\alpha(s)$ is related to the disk surface density $\sigma(\rho)$ and the angular-velocity distribution $\omega(\rho)$ by simple integral relations. The potential $\Phi(\rho, z)$ is related to the potential $\tilde{\Phi}$ by the Thomson transformation and satisfies the Laplace equation everywhere except the disk. On a $z = 0$, $\rho \le R$ circle, the normal derivative $\partial\Phi/\partial z$ changes abruptly. Indeed, let z tend to zero. Using (2), we then have

$$\lim_{z\to+0}\frac{\partial\Phi}{\partial z} = \frac{\tilde{\rho}^3}{R^2}\lim_{\tilde{z}\to+0}\frac{\partial\tilde{\Phi}}{\partial\tilde{z}}, \qquad (4)$$

while it follows from (3) that

$$\lim_{\tilde{z}\to+0}\frac{\partial\tilde{\Phi}}{\partial\tilde{z}} = \lim_{\tilde{z}\to+0}\frac{1}{2\pi^2}\int_0^\pi d\theta\int_R^\infty \qquad (5)$$
$$\times\left(\frac{-i}{s - \tilde{\rho}\cos\theta - i\tilde{z}} + \frac{i}{s - \tilde{\rho}\cos\theta + i\tilde{z}}\right)\alpha(s)ds.$$

Using the Sokhotski formula for Cauchy-type integrals, we can obtain the following relation from (5):

$$\left.\frac{\partial\tilde{\Phi}}{\partial\tilde{z}}\right|_{\tilde{z}\to+0} = \begin{cases} 0, & 0 \le \tilde{\rho} < R \\ \dfrac{1}{\pi}\displaystyle\int_R^{\tilde{\rho}}\frac{\alpha(s)ds}{\sqrt{\tilde{\rho}^2 - s^2}}, & \tilde{\rho} > R \end{cases} \qquad (6)$$

or, returning to the ρ and z coordinates,

$$\left.\frac{\partial\Phi}{\partial z}\right|_{z\to+0} = -2\pi G\sigma(\rho) \qquad (7)$$
$$= \begin{cases} \dfrac{R^4}{\pi\rho^2}\displaystyle\int_R^{R^2/\rho}\frac{\alpha(s)ds}{\sqrt{R^4 - \rho^2 s^2}}, & 0 \le \rho < R \\ 0, & \rho > R, \end{cases}$$

where $\sigma(\rho)$ is the disk surface density.

The equilibrium condition for particles in the disk or, in other words, the equality of the gravitational and centrifugal forces for dustlike matter in the $z = 0$, $\rho < R$ disk,

$$\left.\frac{\partial\Phi}{\partial\rho}\right|_{z\to0} + \omega^2\rho = 0 \qquad (8)$$

can be represented as

$$\frac{\partial}{\partial\tilde{\rho}}(\tilde{\rho}\tilde{\Phi}) = \frac{\omega^2 R^4}{\tilde{\rho}^3}; \quad (9)$$

whence it follows that

$$\tilde{\rho}\frac{\partial\tilde{\Phi}}{\partial\tilde{\rho}} = \frac{R^4}{\tilde{\rho}}\int\tilde{\rho}\left(\frac{\omega^2}{\tilde{\rho}^3}\right)_{,\tilde{\rho}}d\tilde{\rho}. \quad (10)$$

The left-hand side of (10) can be represented using (3) in the limit $z \to 0$ as

$$\tilde{\rho}\frac{\partial\tilde{\Phi}}{\partial\tilde{\rho}} = \frac{1}{\pi}\left(\int_R^\infty \alpha(s)ds - \int_{\tilde{\rho}}^\infty \frac{\alpha(s)sds}{\sqrt{s^2-\tilde{\rho}^2}}\right). \quad (11)$$

Below, we pass to the dimensionless variables

$$t \equiv R^2/s^2, \quad x \equiv R^2/\tilde{\rho}^2 = \rho^2/R^2. \quad (12)$$

and denote the complex functions $f(s(t))$ and $\psi(\rho(x))$ just as $f(t)$ and $\psi(x)$.

Formula (7) for the surface-density distribution then takes the form

$$\sigma(x) = -\frac{R}{4\pi^2 Gx}\int_x^1 \frac{\alpha(t)dt}{t\sqrt{t-x}} \quad (13)$$

(we emphasize that $\sigma(x)$ has no singularity at $x = 0$ due to condition (15)). We can now calculate the total mass of the disk:

$$M = 2\pi\int_0^R \sigma(\rho)\rho d\rho = -\frac{R^3}{4\pi G}\int_0^1 \frac{dx}{x}\int_x^1 \frac{\alpha(t)dt}{t\sqrt{t-x}}. \quad (14)$$

For the disk mass M to be finite, the following equality must be satisfied:

$$\lim_{x\to 0}\int_x^1 \frac{\alpha(t)dt}{t\sqrt{t-x}} = \int_0^1 \frac{\alpha(t)dt}{t^{3/2}} = 0. \quad (15)$$

Using (14) and (15), we can derive a simpler formula for the disk mass:

$$M = -\frac{R^3}{4\pi G}\int_0^1 \frac{\alpha(t)}{t^{3/2}}\ln t\mathrm{d}t = \frac{2}{\pi G}\int_0^R \frac{v^2\rho d\rho}{\sqrt{R^2-\rho^2}}. \quad (16)$$

Taking into account (11) and (15), we can derive the following Abel integral equation for $\alpha(t)$ from the equilibrium condition (10):

$$-\frac{1}{2\pi}\int_0^x \frac{\alpha(t)\mathrm{d}t}{t^{3/2}\sqrt{x-t}} = \int_0^x (\omega^2 t^{3/2})'_t\frac{\mathrm{d}t}{\sqrt{t}} + A_0, \quad (17)$$

where the integration constant should be determined by using condition (15).

The solution of Eq. (17) can be written as (see, e.g., Sneddon 1956, p. 318):

$$\frac{\alpha(x)}{2x^{3/2}} = -\frac{\mathrm{d}}{\mathrm{d}x}\int_0^x \frac{\mathrm{d}t}{\sqrt{x-t}} \quad (18)$$

$$\times\left(A_0 + \int_0^t \frac{1}{\sqrt{s}}(\omega^2 s^{3/2})'_s\mathrm{d}s\right) = -\frac{A_0}{\sqrt{x}} - \int_0^x \frac{(\omega^2 t^{3/2})'_t\mathrm{d}t}{\sqrt{t}\sqrt{x-t}},$$

where the constant A_0 from condition (15) is given by the formula

$$A_0 = -\frac{1}{2}\int_0^1 \frac{\omega^2(t)dt}{\sqrt{1-t}}.$$

In general, the surface density has the following asymptotics near the outer edge $x \to 1$:

$$\sigma(x) \approx A\sqrt{1-x}, \quad (19)$$

$$A = \frac{2R}{\pi^2 G}\int_0^1 \frac{(\omega^2 t^{3/2})'_t\sqrt{t}\mathrm{d}t}{\sqrt{1-t}}.$$

Formulas (13) and (18) give a *general* solution of the problem under consideration in the form of two sequential quadratures: for a given function $\omega(\rho)$ (angular velocity), we must first find the function $\alpha(\rho)$ using formula (18) and then calculate the surface density $\sigma(\rho)$ using formula (13). Thus, we obtain

$$\sigma(\rho) = \frac{1}{\pi^2 G}\int_\rho^R \frac{d\rho'}{\sqrt{\rho'^2-\rho^2}}\int_0^{\rho'} \frac{dv^2}{dr}\frac{dr}{\sqrt{\rho'^2-r^2}}$$

$$= \frac{1}{\pi^2 G}\left[\int_0^\rho \frac{dv^2}{d\rho'}F\left(\mu,\frac{\rho'}{\rho}\right)\frac{d\rho'}{\rho} + \int_\rho^R \frac{dv^2}{d\rho'}F\left(\mu',\frac{\rho}{\rho'}\right)\frac{d\rho'}{\rho'}\right], \quad (20)$$

$$\mu \equiv \arcsin\sqrt{\frac{R^2-\rho^2}{R^2-\rho'^2}}, \quad \mu' \equiv \arcsin\sqrt{\frac{R^2-\rho'^2}{R^2-\rho^2}}.$$

In this formula, we denote the incomplete elliptical integral of the first kind by

$$F(\phi,k)=\int_0^\phi (1-k^2\sin^2\alpha)^{-1/2}d\alpha.$$

When $R\to\infty$, the derived formula (20) asymptotically transforms into the formula by Toomre (1963) for infinite disks (see the monograph by Binney and Tremaine (1987) for a discussion of Toomre's formula). In this case, the total disk mass is defined by formula (16). A simpler formula can be derived from (20) for the surface density at the center of the galactic disk:

$$\sigma(0)=\frac{1}{\pi^2 G}\int_0^R\left(\frac{\rho}{\sqrt{R^2-\rho^2}}+\arcsin\sqrt{1-\frac{\rho^2}{R^2}}\right)\frac{v^2 d\rho}{\rho^2}. \tag{21}$$

Let us consider specific analytical examples, primarily Kuzmin–Toomre rotation curves (Kuzmin 1956; Toomre 1963):

$$\omega^2=\omega_0^2 b^3/(b^2+\rho^2)^{3/2}, \quad \omega_0, b=\text{const}. \tag{22}$$

These rotation curves belong to the family of rotation curves suggested by Brandt (1960) for *infinite* disks with Keplerian asymptotic behavior when $\rho\to\infty$ as a special case; the parameter b multiplied by $\sqrt{2}$ has the meaning of the radius of the circumference on which the linear velocity reaches its maximum; ω_0 has the meaning of angular velocity at the disk center. Toomre (1963) considered a wide class of asymptotically Keplerian rotation curves:

$$\omega_n^2=\frac{\omega_0^2 b^{2n+2}}{n!}\left(-\frac{\partial}{\partial b^2}\right)^{n-1}\frac{1}{b(b^2+\rho^2)^{3/2}}, \quad n=1,2\ldots. \tag{23}$$

This class includes the Kuzmin–Toomre rotation curves (20) as a special case for $n=1$. At $\rho=0$, the functions $\omega_n(\rho)$ take on ω_0. For *infinite* disks, the corresponding density distributions are given by the formula

$$\sigma_n(\rho)=\frac{\omega_0^2 b^{2n+2}(2n-1)!!}{2^n n!\pi G(b^2+\rho^2)^{(2n+1)/2}}. \tag{24}$$

Let us now derive an analogue of formulas (24) for *finite* disks. To this end, we rewrite formulas (23) as functions of the dimensionless variable $x=\rho^2/R^2$ and the parameter $a=b^2/R^2$:

$$\omega_n^2=\frac{\omega_0^2 a^{n+1}}{n!}\left(-\frac{\partial}{\partial a}\right)^{n-1}\frac{1}{\sqrt{a}(x+a)^{3/2}}. \tag{25}$$

We first consider the case where $n=1$. Substituting ω_1^2 into (18) yields

$$\frac{\alpha_1(x)}{2x^{3/2}}=-\omega_0^2\left(\frac{\sqrt{x}(3a+x)a}{(a+x)^2}-\frac{2-a}{(1+a)\sqrt{x}}\right). \tag{26}$$

The corresponding formula for the surface density can be obtained using (13):[1]

$$\sigma_1(x)=\frac{\omega_0^2 a^{3/2} bS}{\pi^2 G}, \qquad S\equiv\frac{\sqrt{(1-x)(a+x)}+(1+a)\arctan\sqrt{(1-x)/(a+x)}}{(1+a)(a+x)^{3/2}}. \tag{27}$$

Since the problem is linear, the surface density corresponding to the rotation curve (25) is given by the formula

$$\sigma_n(x)=\frac{\omega_0^2 a^{n+\frac{1}{2}}R}{n!\pi^2 G}\left(-\frac{\partial}{\partial a}\right)^{n-1}S. \tag{28}$$

In the limit $R\to\infty$, formula (28) reduces to Toomre's formula (24). Figure 1 shows the surface-density distribution (27) as a function of ρ/b for various b^2/R^2 ratios.

The total mass of a disk with the surface density (28) is

$$M_n=\frac{2\omega_0^2 a^{n+1}R^3}{n!\pi G}\left(-\frac{\partial}{\partial a}\right)^{n-1} \tag{29}$$

[1] Formula (25) was first discussed by Hunter *et al.* (1984) in terms of the approach by Mestel (1963).

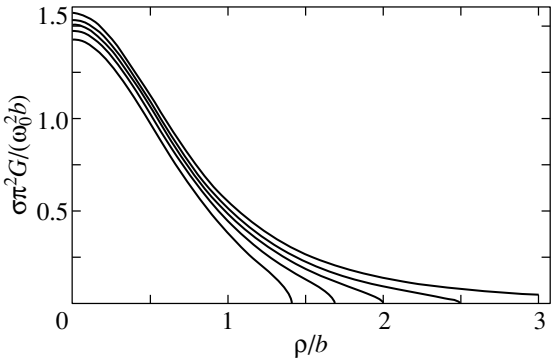

Fig. 1. Density distribution (25) for $a = 0, 0.16, 0.25, 0.35$, and 0.5 (the lines are ordered from top to bottom).

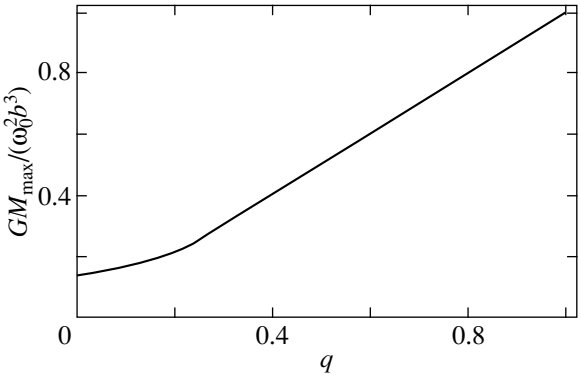

Fig. 2. Maximum possible disk mass versus parameter q in the examples given by formulas (34)–(36).

$$\times \left(-\frac{1}{1+a} + \frac{1}{\sqrt{a}} \arctan \frac{1}{\sqrt{a}} \right).$$

Consider the rotation curves formed by linear combinations of the functions ω_n^2 defined by formulas (23):

$$\omega^2 = \sum_{n=1}^{N} c_n \omega_n^2, \qquad \sum_{n=1}^{N} c_n = 1. \tag{30}$$

Such rotation curves also exhibit Keplerian asymptotic behavior at large ρ^2 and a given angular velocity ω_0 at the disk center. The corresponding density distribution and the total mass are given by the formulas

$$\sigma(x) = \sum_{n=1}^{N} c_n \sigma_n(x), \quad M = \sum_{n=1}^{N} c_n M_n(x). \tag{31}$$

Near the outer edge of the disk, the surface density has the asymptotics

$$\sigma(x) \approx \frac{\omega_0^2 R \sqrt{1-x}}{\pi^2 G} \sum_{n=1}^{N} c_n \left(\frac{a}{a+1} \right)^n. \tag{32}$$

An important outstanding problem that we would like to discuss in connection with the formalism developed above is the estimation of the upper limit for the galactic mass and the outer radius of the disk (it is well known that galactic disks can extend to distances much larger than the observable region (Schmidt 1957)).

Let the smooth distribution $\omega^2(\rho)$ be known from observational data for $0 \le \rho \le R_v$, where R_v is the known radius of the visible part of the disk. The corresponding function $\sigma(\rho)$ can then be constructed from formulas (13) and (18) under the condition of a hypothetical extrapolation of the rotation curve to the unseen region, with the outer radius of the disk R being the unknown parameter to be determined. The upper limit $R_{\max}$ for the disk radius can be found from the conditions $\sigma(\rho = R) = 0, d\sigma/d\rho = 0$ or $A = 0$ (see formula (19)). The value of $R_{\max}$ obtained in this way can then be substituted into formula (16) to estimate the upper limit for the mass. An equivalent way of obtaining $R_{\max}$ is to use the condition for maximum mass. The radii R and masses M of galactic disks then satisfy the inequalities $R_v \le R \le R_{\max}$ and $M \le M_{\max}$, respectively. For Toomre's rotation curves ω_n^2 (which act as "pure states"), $R_{\max} = \infty$. However, for a linear superposition of various ω_n^2 (mixed states), the disk mass can have a maximum at some finite $R_{\max}$. Therefore, for the radii of disks with such rotation curves, the upper limit is $R \le R_{\max}$. The existence of an upper limit for the mass at a finite disk radius for analytically extended rotation curves is a new physical phenomenon (similar to the existence of a limiting mass for barotropic, uniformly rotating neutron stars (Tassoul 1978)). For example, for the angular-velocity distributions in (30), the condition $(A = 0)$ yields the algebraic equation

$$\sum_{n=1}^{N} c_n \left(\frac{a}{a+1} \right)^n = 0. \tag{33}$$

As can be easily seen, when all $c_n > 0$ and $n = \overline{1, N}$, this equation has the only nonnegative root $a = 0$ that corresponds to $R = \infty$. However, when $c_1 < 0$, $c_i > 0, i = \overline{2, N}$, an additional positive root $a = a_* > 0$ appears. In the interval $0 < a < a_*$, the surface density is negative near the outer disk edge $x = 1$, so formulas (31) are physically meaningful only for $a \ge a_*$. Therefore, the upper limit for the disk radius is $R_{\max} = b/\sqrt{a_*}$. We illustrate the above discussion by the following simple linear combination of

[2] However, the actual disk radius (cutoff radius) can be much smaller than the ρ values for which Keplerian asymptotic behavior shows up.

curves (22):

$$\omega^2 = \frac{4q-1}{3}\omega_1^2 + \frac{4}{3}(1-q)\omega_2^2 = \omega_0^2 \qquad (34)$$
$$\times \left[q\left(\frac{a}{a+x}\right)^{3/2} + (1-q)\left(\frac{a}{a+x}\right)^{5/2}\right],$$
$$0 \le q \le 1, \quad 0 < a < 0.5.$$

The corresponding surface-density distributions are given by

$$\sigma(x) = \frac{4q-1}{3}\sigma_1(x) + \frac{4}{3}(1-q)\sigma_2(x), \qquad (35)$$

where σ_1 and σ_2 are defined by formula (27).

The derivative $(d\sigma/d\rho)_{\rho=R}$ is equal to zero at $-1+3a+4q=0$; whence $a=(1-4q)/3$.

On the other hand, the mass of a disk with the angular-velocity distribution (34) is

$$M = \frac{2\omega_0^2 b^3}{\pi}\left[\frac{\sqrt{a}(2-5q-3aq)}{3(1+a)^2} + q\arctan\frac{1}{\sqrt{a}}\right]. \qquad (36)$$

For a fixed value of $\omega_0^2 b^3$, the disk mass as a function of a reaches its maximum at $a_* = (1-4q)/3$.

Therefore, we reach the following important conclusion:

If $0 \le q < 0.25$, then the disk radius is limited from above by $b\sqrt{3/(1-4q)}$. For $0.25 \le q \le 1$ (as follows from formula (36)), the disk mass is a monotonically decreasing function of a, so the disk mass reaches its maximum in the limit $R \to \infty$. Maximum mass $M_{\max}$ is plotted against q in Fig. 2. This example in particular demonstrates the difficulties in fitting the observed rotation curve by a superposition of standard rotation curves for infinite self-gravitating disks. These difficulties are naturally resolved for finite disks.

ACKNOWLEDGMENTS

We wish to thank the referees for their helpful remarks. This work was supported by CONACyT, Mexico (project nos. 34222-E and 38495-E). N.R. Sibgatullin would like to express his gratitude to SNI-CONACyT, Mexico.

REFERENCES

1. H. W. Babcock, Lick Obs. Bull. **19**, 41 (1939).
2. J. Binney and M. Merrifield, *Galactic Astronomy* (Princeton Univ. Press, Princeton, 1998).
3. J. Binney and S. Tremaine, *Galactic Dynamics* (Princeton Univ. Press, Princeton, 1987).
4. G. S. Bisnovatyi-Kogan and S. I. Blinnikov, Astrophys. Space Sci. **19**, 93 (1972).
5. J. C. Brandt, Astrophys. J. **131**, 293 (1960).
6. J. C. Brandt and M. J. S. Belton, Astrophys. J. **136**, 352 (1962).
7. E. M. Burbidge and G. R. Burbidge, *Stars and Stellar Systems IX: Galaxies and the Universe,* Ed. by A. Sandage, M. Sandage, and J. Kristian (Chicago Univ. Press, 1975), p. 81.
8. E. M. Burbidge, G. R. Burbidge, and K. N. Prendergast, Astrophys. J. **131**, 286 (1960).
9. D. Burstein and V. C. Rubin, Astrophys. J. **297**, 423 (1985).
10. C. Hunter, Mon. Not. R. Astron. Soc. **126**, 299 (1963).
11. J. H. Hunter, R. Ball, and S. T. Gottesman, Mon. Not. R. Astron. Soc. **208**, 14 (1984).
12. R. I. Kiladze, Byull. Abastuman. Obs. No. 22, 125 (1958).
13. P. C. van der Kruit and R. J. Allen, Ann. Rev. Astron. Astrophys. **16**, 103 (1978).
14. S. A. Kutuzov and L. P. Osipkov, Astron. Zh. **65**, 468 (1988) [Sov. Astron. **32**, 240 (1988)].
15. G. G. Kuzmin, Astron. Zh. **33**, 27 (1956).
16. N. N. Lebedev, *A Collection of Problems on Equations of Mathematical Physics* (Nauka, Moscow, 1965).
17. L. Mestel, Mon. Not. R. Astron. Soc. **126**, 553 (1963).
18. T. Morgan and L. Morgan, Phys. Rev. **183**, 1097 (1969).
19. A. G. Morozov and A. M. Fridman, Astron. Zh. **50**, 1028 (1973) [Sov. Astron. **17**, 651 (1973)].
20. M. Persic and P. Salucci, Mon. Not. R. Astron. Soc. **234**, 131 (1988).
21. M. Persic, P. Salucci, and F. Stel, Mon. Not. R. Astron. Soc. **281**, 27 (1996).
22. V. L. Polyachenko and A. M. Fridman, *Equilibrium and Stability of Gravitating Systems* (Nauka, Moscow, 1976), p. 214.
23. M. Schmidt, Bull. Astron. Inst. Neth. **14**, 17 (1957).
24. N. R. Sibgatullin, A. A. Garcia, and V. S. Man'ko, Pis'ma Astron. Zh. **29**, 88 (2003) [Astron. Lett. **29**, 70 (2003)]; astro-ph/0209200.
25. I. N. Sneddon, *The Use of Integral Transforms* (McGraw-Hill, New York, 1956).
26. I. N. Sneddon, *Mixed Boundary Value Problems in Potential Theory* (North-Hooland, Amsterdam, 1966).
27. Y. Sofue and V. C. Rubin, Ann. Rev. Astron. Astrophys. **39**, 137 (2001).
28. J.-L. Tassoul, *Theory of Rotating Stars* (Princeton Univ. Press, Princeton, 1978; Mir, Moscow, 1982).
29. A. Toomre, Astrophys. J. **138**, 385 (1963).
30. G. de Vaucouleurs and K. C. Freeman, Vistas in Astronomy **14**, 163 (1972).

Translated by A. Dambis

Astronomy Letters, Vol. 29, No. 12, 2003, pp. 831–845. Translated from Pis'ma v Astronomicheskiĭ Zhurnal, Vol. 29, No. 12, 2003, pp. 934–950.

The Toroidal Iron Atmosphere of a Protoneutron Star: Numerical Solution

V. S. Imshennik*, K. V. Manukovskii, and M. S. Popov

Institute for Theoretical and Experimental Physics, ul. Bol'shaya Cheremushkinskaya 25, Moscow, 117259 Russia

Received June 20, 2003

Abstract—A numerical method presented by Imshennik *et al.* (2002) is used to solve the two-dimensional axisymmetric hydrodynamic problem on the formation of a toroidal atmosphere during the collapse of an iron stellar core and outer stellar layers. An evolutionary model from Boyes *et al.* (1999) with a total mass of $25M_\odot$ is used as the initial data for the distribution of thermodynamic quantities in the outer shells of a high-mass star. Our computational region includes the outer part of the iron core (without its central part with a mass of $1M_\odot$ that forms the embryo of a protoneutron star at the preceding stage of the collapse) and the silicon and carbon–oxygen shells with a total mass of $(1.8–2.5)M_\odot$. We analyze in detail the results of three calculations in which the difference mesh and the location of the inner boundary of the computational region are varied. In the initial data, we roughly specify an angular velocity distribution that is actually justified by the final result—the formation of a hydrostatic equilibrium toroidal atmosphere with reasonable total mass, $M^{\rm tot} = (0.117–0.122)M_\odot$, and total angular momentum, $J^{\rm tot} = (0.445–0.472) \times 10^{50}$ erg s, for the two main calculations. We compare the numerical solution with our previous analytical solution in the form of toroidal atmospheres (Imshennik and Manukovskii 2000). This comparison indicates that they are identical if we take into account the more general and complex equation of state with a nonzero temperature and self-gravitation effects in the atmosphere. Our numerical calculations, first, prove the stability of toroidal atmospheres on characteristic hydrodynamic time scales and, second, show the possibility of sporadic fragmentation of these atmospheres even after a hydrodynamic equilibrium is established. The calculations were carried out under the assumption of equatorial symmetry of the problem and up to relatively long time scales ($\sim$10 s). © *2003 MAIK "Nauka/Interperiodica".*

Key words: *plasma astrophysics, hydrodynamics, and shock waves.*

INTRODUCTION

The theory of the spherically symmetric gravitational collapse of iron stellar cores is known to have led to a clear separation of the collapse into two stages (see, e.g., Imshennik and Nadyozhin 1982). At the first stage, the inner part of the iron core with a mass $M_{i\rm Fe} \leq 1M_\odot$ (Imshennik 1992) or, more precisely, with a mass of $(0.6–0.8)M_\odot$ (Nadyozhin 1998) collapses homologically. The remaining outer part of the iron core with a mass $M_{e\rm Fe} = M_{\rm Fe} - M_{i\rm Fe} \cong (0.4 - 1.4)M_\odot$ in the known range of iron core masses $M_{\rm Fe} = (1.2 - 2.0)M_\odot$ lags well behind its inner part in contraction. In a rough approximation, it may even be assumed to maintain a hydrostatic equilibrium of the initial state. This is especially true for the outer layers of a high-mass star. Imshennik *et al.* (2002) reduced the question about the hydrodynamic behavior of the outer part of the iron core (the second stage of its collapse) and other outer layers of a collapsing star to the problem of their accretion from a hydrostatic equilibrium onto the embryo of a protoneutron star (PNS) with a mass of about $1M_\odot$. The end of the first stage of iron core collapse was taken as the initial time of hydrodynamic post-shock accretion; the corresponding problem was formulated by Brown *et al.* (1992). This simplification of the problem allowed us, first, to exclude the complex neutrino processes from consideration (i.e., to restrict our analysis to the approximation of ideal hydrodynamics), and, second, to include the hydrodynamic processes in the remaining onion stellar structure that surrounds the iron core of a high-mass star with a total mass

*E-mail: imshennik@vxitep.itep.ru

$M_{\rm MS} \geq 10M_\odot$.[1] In this paper, we continue to numerically analyze this post-shock accretion, but now we take into account the rotation effects by solving the two-dimensional axisymmetric problem.

The main result of the gravitational collapse of a rapidly rotating iron stellar core can be a binary system of neutron stars (Imshennik 1992) and its surrounding iron gaseous medium that did not enter into the composition of the rotating PNS at the second stage of the collapse. In this case, the rotating PNS is generally unstable against fragmentation and turns into a binary system of neutron stars (Aksenov *et al.* 1995). Based on a quasi-one-dimensional model, Imshennik and Nadyozhin (1992) showed that, with a sufficiently rapid initial rotation of an $M_{\rm Fe} = 2M_\odot$ iron core and a full allowance for the neutrino processes, an iron atmosphere with a mass of $(0.1{-}0.2)M_\odot$ distributed almost uniformly throughout the iron core with an initial outer radius $R_{\rm Fe} = 4.38 \times 10^8$ cm, i.e., with a mean density $\rho_{e\rm Fe} \cong (5.66 \times 10^5{-}1.13 \times 10^6)$ g cm^{-3}, is formed. The presumed long existence of this binary system of neutron stars, possibly for several hours (Imshennik and Popov 1994), made the problem of steady iron gas accretion onto this binary (actually, onto its more massive component located almost at the stellar center) of relevant interest. For the one-dimensional accretion of a cold (with zero temperature) iron gas with quasi-one-dimensional rotation, Imshennik and Popov (2001) managed to generalize the standard steady-state solution by Bondi (1952) due to the very simple form of the specific enthalpy for the degenerate electron gas of an iron atmosphere with the complete ionization of iron atoms and arbitrary electron relativity. Application of this solution to the physical conditions near PNSs (with masses $(1.4{-}1.8)M_\odot$) showed that the accretion rate was very high, $(20{-}30)M_\odot$ s^{-1} at the above typical densities $\rho_{e\rm Fe}$ and a neutron star mass of $1.8M_\odot$. On the other hand, the steady-state accretion solution obtained does not fit into the iron core; besides, the time it takes for this solution to be established is too long. In short, it is not applicable to our problem on the second stage of the collapse of the outer iron core (Imshennik and Popov 2001). The quasi-one-dimensional rotation effects taken into account in the above paper proved to be negligible because of the severe constraints on the specific angular momentum j_∞ (at infinity!) specified in addition to the density ρ_∞. At the same time, based on ideal two-dimensional hydrodynamics, we were able to analytically construct a steady-state solution with the same equation of state for a cold iron gas in the form of toroidal atmospheres with a given arbitrary rotation law (Imshennik and Manukovskii 2000).

A natural continuation of the above studies of analytical solutions seems to be the application of our numerical method of solution (Imshennik *et al.* 2002) to the problem of postshock accretion near neutron stars, using a complete equation of state with temperature effects (arbitrary electron degeneracy, the appearance of positrons, the presence of a nuclide gas and blackbody radiation), and a consistent allowance for the gravitational interaction, including the two-dimensional self-gravitation of the accreted matter. As was done previously (Imshennik *et al.* 2002), the hydrostatic equilibrium solutions obtained in evolutionary calculations (Boyes *et al.* 1999) and modified to incorporate the quasi-one-dimensional rotation effects can also be used as the initial time and the initial conditions that describe the statement of the postshock accretion problem (see above). Note that the accuracy of the hydrostatic equilibrium of these outer layers, including the action of centrifugal forces is not of such fundamental importance as it was in Imshennik *et al.* (2002), because it essentially does not matter precisely what time is taken as the initial one in the unsteady-state hydrodynamic simulation of the outer layers of a high-mass star under consideration.

As we show in this paper, the hydrodynamic postshock accretion actually gives rise to toroidal structures at the locations of the outer layers of an iron stellar core, in agreement with the analytical solutions from Imshennik and Manukovskii (2000). Thus, we clearly prove the hydrodynamic stability of such toroidal iron atmospheres against arbitrarily small two-dimensional perturbations. As regards the steady one-dimensional accretion, it does not take place during the postshock accretion: instead, significant accretion onto the embryo of a PNS (with an initial mass of approximately $1M_\odot$) takes place in the near-axis region for part of the matter with the sufficiently low specific angular momenta specified in the initial conditions (with a total mass of about $0.8M_\odot$).

[1] Imshennik *et al.* (2002) showed that the previously assumed influence of the decrease in the gravitational mass of a PNS due to intense neutrino energy losses during collapse was negligible: it does not lead to the emersion of the outer stellar layers in a wide range of total masses, $(12{-}25)M_\odot$. Unfortunately, another effect, the imitation of nucleon bubbles embedded in an initial spherically symmetric configuration under equilibrium conditions, was considered with the erroneous overestimation of their total energy attributable to the unacceptably abrupt changes in initial specific internal energy at the outer boundary of the nucleon bubbles. After the rectification of these unfortunate inaccuracies (a several-fold decrease in initial specific internal energy), the emersion effect of the outer layers also vanished, and it was generally interpreted as a small correction to the adopted equation of state because of the energy release of free-nucleon recombination into iron.

This accretion is not only non-one-dimensional but also unsteady, with the ejection of whole fragments of matter from the toroidal atmosphere, a curious effect that was found in these calculations.

FORMULATION OF THE PROBLEM

The System of Equations, the Equation of State, and the Numerical Method of Solution

In most cases, the hydrodynamic behavior of the envelope of a high-mass star can be described by the system of equations of ideal hydrodynamics. In our axisymmetric case $\left(\frac{\partial}{\partial\varphi}, g_\varphi = 0\right)$, this system in spherical coordinates (r, θ, φ) is

$$\frac{\partial\rho}{\partial t} + \frac{1}{r^2}\frac{\partial}{\partial r}(r^2\rho V_r) + \frac{1}{r\sin\theta}\frac{\partial}{\partial}(\sin\theta\rho V_\theta) = 0, \quad (1)$$

$$\frac{\partial\rho V_r}{\partial t} + \frac{1}{r^2}\frac{\partial}{\partial r}(r^2\rho V_r^2) + \frac{1}{r\sin\theta}\frac{\partial}{\partial\theta}(\sin\theta\rho V_r V_\theta) + \frac{\partial P}{\partial r} - \frac{\rho(V_\theta^2 + V_\varphi^2)}{r} = \rho g_r, \quad (2)$$

$$\frac{\partial\rho V_\theta}{\partial t} + \frac{1}{r^2}\frac{\partial}{\partial r}(r^2\rho V_r V_\theta) + \frac{1}{r\sin\theta}\frac{\partial}{\partial\theta}(\sin\theta\rho V_\theta^2) + \frac{1}{r}\frac{\partial P}{\partial\theta} + \frac{\rho V_r V_\theta}{r} - \frac{\rho V_\varphi^2\cot\theta}{r} = \rho g_\theta, \quad (3)$$

$$\frac{\partial\rho V_\varphi}{\partial t} + \frac{1}{r^2}\frac{\partial}{\partial r}(r^2\rho V_r V_\varphi) + \frac{1}{r\sin\theta}\frac{\partial}{\partial\theta}(\sin\theta\rho V_\theta V_\varphi) + \frac{\rho V_\varphi}{r}(V_r + \cot\theta V_\theta) = 0, \quad (4)$$

$$\frac{\partial\rho E}{\partial t} + \frac{1}{r^2}\frac{\partial}{\partial r}(r^2 V_r(\rho E + P)) + \frac{1}{r\sin\theta}\frac{\partial}{\partial\theta}(\sin\theta V_\theta(\rho E + P)) = \rho(V_r g_r + V_\theta g_\theta), \quad (5)$$

where $E = \varepsilon + \dfrac{\mathbf{v}^2}{2}$ is the sum of the specific internal (ε) and kinetic energies. The acceleration of gravity is $\mathbf{g} = \mathbf{g}_{\rm ns} + \mathbf{g}_{\rm atm}$; i.e., it is the sum of two components. The first component is attributable to the gravitational field that is produced by the PNS located exactly at the coordinate origin:

$$\mathbf{g}_{\rm ns} = \left(-\frac{GM_{\rm ns}}{r^2}, 0, 0\right). \quad (6)$$

The second component is attributable to the intrinsic gravitational field of the iron atmosphere. The acceleration of this field is defined by the standard equation $\mathbf{g}_{\rm atm} = -\nabla\Phi$, and the potential satisfies the Poisson equation

$$\Delta\Phi = 4\pi G\rho. \quad (7)$$

An efficient algorithm convenient for use in the finite-difference scheme of integrating the hydrodynamic equations on a stationary mesh in spherical coordinates (Aksenov 1999) is used to solve the Poisson equation (7) and determine the gravitational acceleration $\mathbf{g}_{\rm atm}$. Thus, in the problem under consideration, we abandon the Roche approximation that was used previously for simplicity (Imshennik and Manukovskii 2000; Imshennik and Popov 2001) and take into account the atmospheric self-gravitation effects. Note that, in general, they are of minor importance.

In this paper, as in our previous paper (Imshennik *et al.* 2002), we use the equation of state for the matter treated as a mixture of a perfect Boltzmann gas of nuclei with a perfect Fermi–Dirac electron–positron gas and blackbody radiation. In a wide temperature range, the matter is assumed to be a mixture of a baryonic component that includes free nucleons (n, p) and helium ($^4_2$He) and iron ($^{56}_{26}$Fe) nuclides, and a Fermi–Dirac electron–positron gas with blackbody radiation. The equation of state obeys the nuclear statistical equilibrium (NSE) conditions with a constant ratio of the mass fractions of neutrons and protons, including those bound in the helium and iron nuclides, $\theta_0 = 30/26$ (Imshennik *et al.* 2002). As previously, we use a tabulated equation of state and precompute the thermodynamic functions with a high accuracy. This method allows complex calculations at each step of the solution of system (1)–(5) to be avoided.

The numerical solution of our problem is based on the popular and universal PPM method. This method uses the Eulerian finite-difference scheme (Colella and Woodward 1984) and is a modification of Godunov's method (Godunov *et al.* 1976). The salient features of the method used were given previously (Imshennik *et al.* 2002). In particular, the real equation of state in the numerical method is locally simulated by the so-called binomial equation of state

$$P = [(\bar\gamma - 1)\varepsilon + c_0^2]\rho - \rho_0 c_0^2; \quad (8)$$

the constants $\bar\gamma$, c_0^2, and ρ_0 are determined by the pressure and its derivative at a given point (ρ, ε):

$$c_0^2 = \left(\frac{\partial P}{\partial\rho}\right)_\varepsilon - \frac{\varepsilon}{\rho}\left(\frac{\partial P}{\partial\varepsilon}\right)_\rho, \quad (9)$$

$$\rho_0 c_0^2 = \rho\left(\frac{\partial P}{\partial\rho}\right)_\varepsilon - P, \quad \bar\gamma - 1 = \frac{1}{\rho}\left(\frac{\partial P}{\partial\varepsilon}\right)_\rho.$$

Using the binomial approximation for the equation of state considerably simplifies the solution of the

problem on discontinuity breakup that underlies our numerical method.

Below, we also give the system of units used in our calculations. The scales of the physical quantities in this system are

$$[r] = R_0, \quad [V_r] = [V_\theta] = [V_\varphi] = (GM_0/R_0)^{1/2}, \tag{10}$$
$$[\rho] = M_0/(4\pi R_0^3), \quad [t] = R_0^{3/2}/(GM_0)^{1/2},$$
$$[P] = GM_0^2/(4\pi R_0^4), \quad [E] = GM_0/R_0,$$
$$[T] = (GM_0^2/(4\pi R_0^4 a_r))^{1/4},$$

where R_0 and M_0 are some length and mass scales, and a_r is the radiation density constant. In units (10), the hydrodynamic equations with Newtonian gravitation contain no dimensionless parameters. It would be natural to use the following characteristic values from our problem as R_0 and M_0: $R_0 = 10^8$ cm and $M_0 = 10^{32}$ g. The numerical values for the scales of the physical quantities from (10) are then

$$[r] = 10^8 \text{ cm}, \quad [V_r] = [V_\theta] \tag{11}$$
$$= [V_\varphi] = 2.583 \times 10^8 \text{ cm s}^{-1},$$
$$[\rho] = 7.958 \times 10^6 \text{ g cm}^{-3}, \quad [t] = 3.971 \times 10^{-1} \text{ s},$$
$$[P] = 5.310 \times 10^{23} \text{ erg cm}^{-3}, [E] = 6.674 \times 10^{16} \text{ erg},$$
$$[T] = 2.894 \times 10^9 \text{ K}.$$

Initial Conditions

As we noted in the Introduction, the formation time of the PNS embryo with the mass (about $1M_\odot$) characteristic of our problem, when all of the outer layers may be assumed to be in hydrostatic equilibrium, may arbitrarily be taken as the initial time ($t = 0$). We used the distributions of thermodynamic quantities obtained in the studies of the evolution of high-mass stars (Boyes *et al.* 1999) as the initial data for constructing the initial conditions of our problem. From the above paper, we took the density and temperature profiles, which, in turn, serve to determine the initial pressure and internal energy distributions by using the adopted equation of state. Of course, the equation of state used in our calculations differs slightly from the equation of state used in obtaining these profiles. The main difference is that we took into account a large number of nuclides of chemical elements in our numerical calculations of stellar evolution. However, a detailed comparison of the equations of state (Imshennik *et al.* 2002) shows that, quantitatively, these differences are moderately large, and passing to a simpler equation of state in our calculations has no significant effect on the radial profiles of thermodynamic quantities. Nevertheless, the initial profiles were recalculated with the new equation of state. In these calculations, we used the radial density distribution from Boyes *et al.* (1999) and reconstructed the new equatorial distributions of the pressure (P) and the remaining thermodynamic quantity ε by solving the system of hydrostatic equilibrium equations with nonzero rotation (in the form of a centrifugal force):

$$\frac{\partial P}{\partial r} = \rho\left(\frac{V_\varphi^2}{r} - \frac{Gm}{r^2}\right), \tag{12}$$

$$\frac{\partial m}{\partial r} = 4\pi r^2 \rho; \tag{13}$$

the pressure P and the radius r at the inner boundary were also taken from Boyes *et al.* (1999) for $m \approx 1M_\odot$. Thus, strictly speaking, the initial spherically symmetric distribution of matter was one of a hydrostatic equilibrium only in the equatorial plane. The sizes of the computational region were chosen in such a way that the inner boundary was at the radius (0.876×10^8 cm) that bounded the region of mass $1M_\odot$ in the initial profile (except the test calculation, in which the inner boundary was a factor of about 2 closer to the center along the radius (0.401×10^8 cm)). There was arbitrariness in choosing the outer boundary along the radius. Since the outer, weakly rotating presupernova layers have no fundamental effect on our result, it was not necessary to include them in our analysis. The outer boundary of the computational region in all our calculations was specified at a radius of 10.002×10^8 cm. The calculations were performed for the evolutionary model of a star with a mass of $25M_\odot$ and solar metallicity ($Z_\odot = 0.02$).

As the initial differential rotation law, we took the analytical formula

$$\omega = \omega_0 \exp\left(-\frac{r^2}{r_0^2}\right), \tag{14}$$

as in our previous paper (Imshennik and Manukovskii 2000), but as a function of the spherical radius. This rotation law corresponds well to the results of the quasi-one-dimensional hydrodynamic calculations of collapse by Imshennik and Nadyozhin (1992), particularly with the given specific values of ω_0 and r_0. We emphasize that, according to the data from Boyes *et al.* (1999), the total angular momentum J_0 within the iron core is $\sim 10^{50}$ erg s; i.e., it is almost equal to the value from the paper mentioned above. Expression (14) was used to construct the hydrostatic equilibrium distribution of thermodynamic quantities on the equator: V_φ in Eq. (12) was calculated by using the formula $V_\varphi = \omega r$. Outside the equator, the initial angular velocity distribution was assumed to

be spherically symmetric, in accordance with (14). In contrast, the initial distributions of the azimuthal velocity V_φ and the specific angular momentum j were, of course, not spherically symmetric, because they were calculated by using the formulas

$$V_\varphi = \omega r \sin\theta, \quad j = V_\varphi r \sin\theta. \qquad (15)$$

In particular, this choice of initial data allows us to avoid such singularities as nonzero azimuthal velocity and angular momentum at $\theta = 0$, and softens a violation of the hydrostatic equilibrium conditions outside the equator.

Boundary Conditions

The region of the solution of our problem, or the computational region, has the shape of a spherical envelope, $r_{\min} \le r \le r_{\max}$. The choice of $r_{\min}$ and $r_{\max}$ has already been determined by the physical considerations outlined in the Subsection "Initial Conditions." Sufficient boundary conditions should be specified precisely at these constant boundary values of the Eulerian radius. The inner boundary at $r = r_{\min}$ is essentially a transparent wall on which the radial gradients of all physical quantities (**V**, ρ, and ε) are assumed to be zero. However, it should be immediately noted that the fact that these derivatives become zero does not adequately fit the physical concept of transparency, being only its simplified, but formally sufficient realization. At the outer boundary, the boundary condition simulates a vacuum outside the computational region: the values of all thermodynamic quantities (ρ, ε, and P) are set equal to nearly zero at $r = r_{\max}$.

Because of equatorial symmetry in addition to axial symmetry, we may restrict our calculations to only one quadrant, so the angle θ for the computational region ranges from 0 to $\pi/2$. At the $\theta = \pi/2$ boundary, the velocity component V_θ is assumed to be zero (and again the derivatives of all thermodynamic quantities become zero). The necessary boundary condition for the gravitational potential, $\Phi \to -\dfrac{GM}{r}$ as $r \to \infty$, is automatically satisfied in the algorithm used to solve the Poisson equation (Aksenov 1999).

RESULTS OF THE NUMERICAL SOLUTION

Below, we describe the results of our numerical solution of the system of differential equations (1)–(5) with the above initial and boundary conditions. In all our post-shock accretion simulations, we used the same model of a high-mass star with a total mass of $25M_\odot$ (Boyes *et al.* 1999). In the main hydrodynamic calculations, the outer computational boundary was exactly at a radius of 1.000168×10^9 cm, and the inner computational boundary was at a radius of 8.764082×10^7 cm. The cases differed in the number of zones into which the computational region was divided. In calculation [1], the total number of zones was 100 in the radial direction and 30 in the direction of change of the polar angle; in calculation [2], these numbers were 150 and 45, respectively. The same set of initial data (see the Subsection *Initial Conditions*) was used as the initial presupernova state. To solve the Poisson equation, we expanded the integral representation of the gravitational potential in terms of Legendre polynomials up to the number $l_{\max} = 20$.

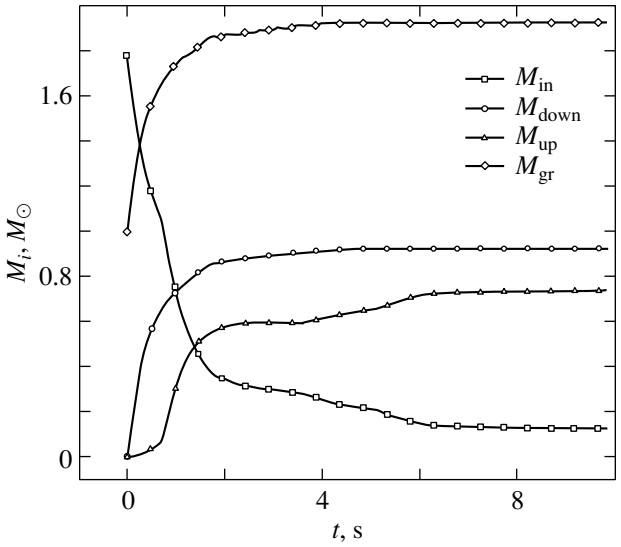

Fig. 1. Total mass of the matter versus time ($0 \le \theta \le \pi$): $M_{\rm in}$ is the mass inside the computational region; $M_{\rm down}$ is the mass that passed through the inner boundary $r = r_{\min}$; $M_{\rm up}$ is the mass that passed through the outer boundary $r = r_{\max}$; $M_{\rm gr}$ is the total mass at $r \le r_{\min}$. All data are for calculation [2].

The behavior of the matter was identical in all our calculations. The initially equilibrium (see the Subsection *Initial Conditions*) outer part of the iron core and the outer layers of the presupernova included in the computational region begin to accrete matter. An atmosphere in the form of a torus or, to be more precise, a thick disk is formed near the central PNS during this accretion. As a result of the accretion, part of the matter passes through the transparent inner computational boundary. By the time the toroidal atmosphere may be considered to have been formed, the total mass of the matter that passed inward is the same, with high accuracy, in all our calculations: $\sim 0.93M_\odot$ (Fig. 1). This mass is mainly determined by the choice of the initial rotation law (14) for the matter (see ω_0 and r_0 below). Because of the vacuum-simulating artificial boundary condition, the matter at the outer (along the radius) boundary also flows out from the computational region away from the center.

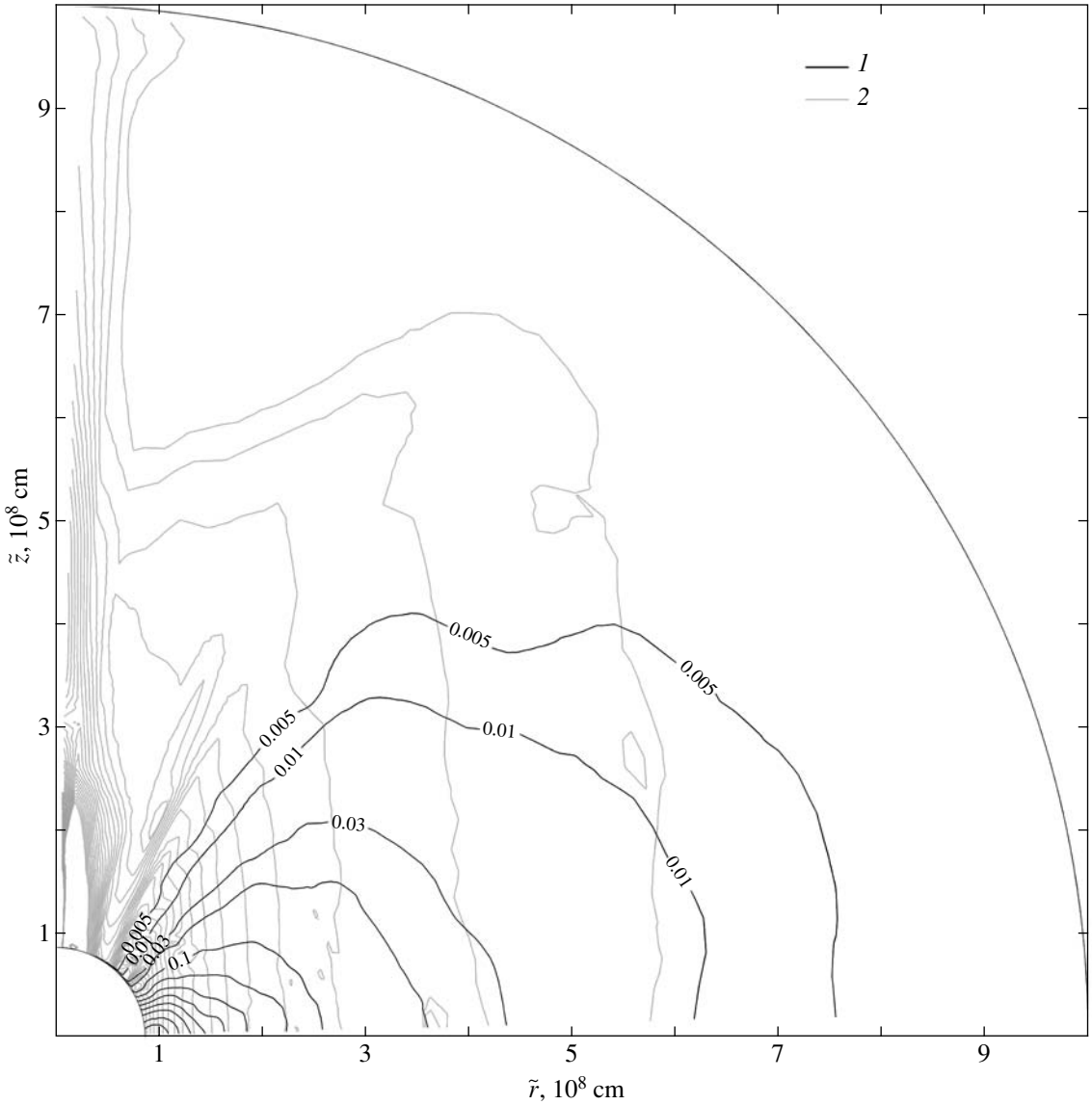

Fig. 2. *1*—Lines of equal matter density at the final time for calculation [1] ($t_f = 29.034$ s); *2*—line of equal angular velocity ω for the same time.

The total mass of the matter that passes outward is $\sim 0.7 M_\odot$ (Fig. 1).

Figures 2 and 3 show lines of equal matter density at the final times for calculations [1] ($t_f = 29.034$ s) and [2] ($t_f = 9.678$ s), respectively. Here (and in Figs. 2–7, 8a, and 9–11), we use the cylindrical coordinates, $\tilde{r} = r \sin\theta$ and $\tilde{z} = r \cos\theta$. Of course, these coordinates are equivalent to the spherical coordinates used in the system of equations (1)–(5) and the finite-difference scheme, but are more convenient for the physical interpretation of the results of our numerical solution. We see that the final state of the matter has an identical structure in both cases. The forming PNS atmosphere is almost twice as extended in the equatorial direction as it is along the rotation axis. For this reason, it would be more precise to call the forming atmosphere a thick disk rather than a torus. The density maximum in both calculations lies in the immediate vicinity of the inner computational boundary. In this situation, the concern about the artificial influence of the chosen boundary condition on the forming atmosphere is quite natural. This circumstance needs the following additional comment.

In an equilibrium rotating atmosphere, the specific angular momentum of the matter is directly proportional to the fluid particle radius. Consequently, particles with a minimum specific angular momentum are located near the inner boundary of the computational region (see below for a discussion of rela-

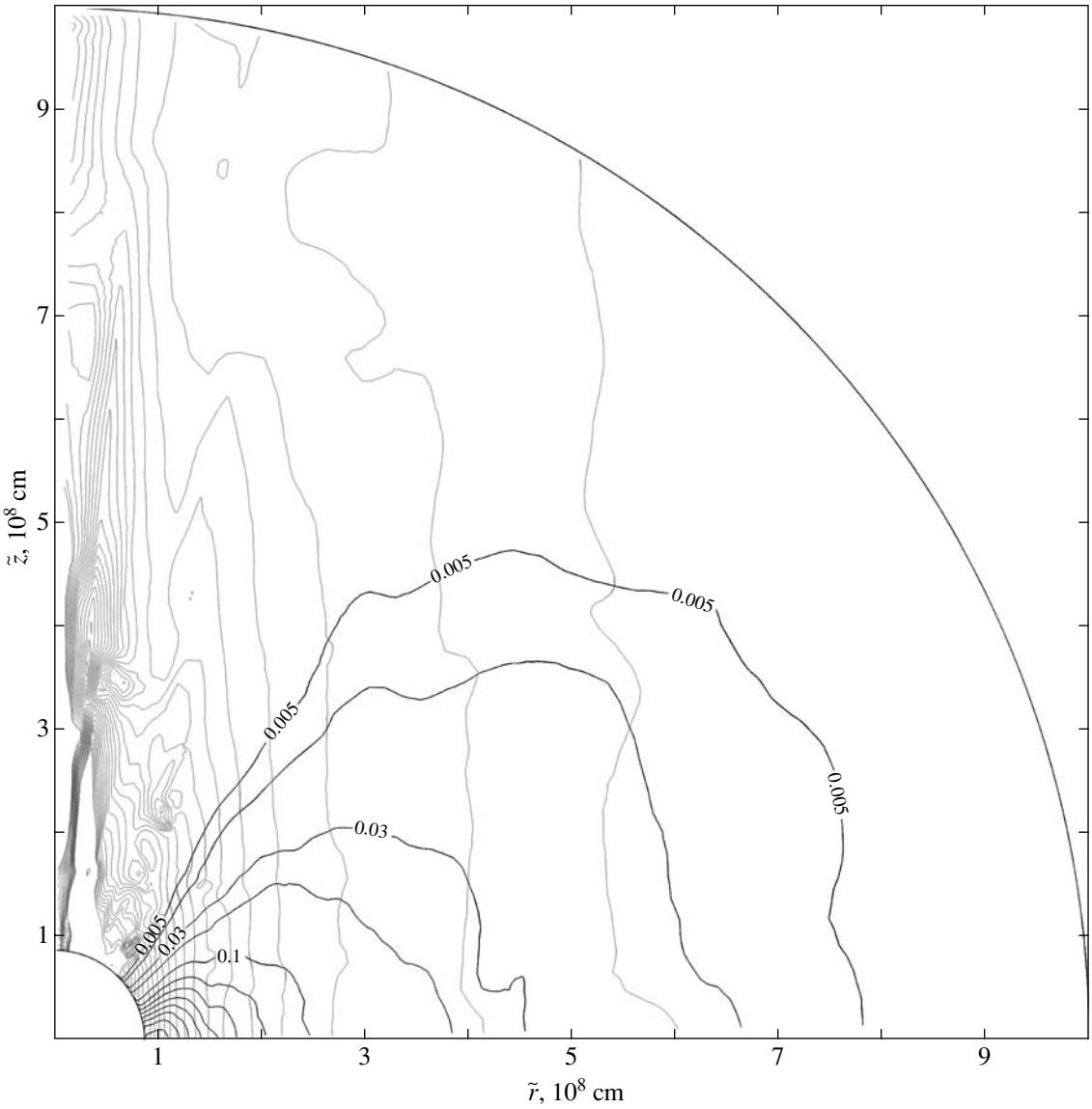

Fig. 3. Same as Fig. 2 for calculation [2] ($t_f = 9.678$ s).

tion (16)). Therefore, if we transfer the inner boundary to a smaller radius, then the formed region will be filled with matter with a lower specific angular momentum; thus, the density maximum will again displace to the inner boundary. The fact that the angular velocity in our initial data varies smoothly ($\omega_0 = 2\ \mathrm{s}^{-1}$, $r_0 = 5 \times 10^8$ cm; see the Subsection *Initial Conditions*), so that there is always an appreciable amount of matter with low specific angular momenta, may also contribute to this displacement. However, the rotation in real high-mass stars is most likely concentrated mainly in the region of the iron core, at the boundary of which the specific angular momentum decreases appreciably. In addition, the concentration of matter near the inner boundary may also be partly attributable to the following factor: In our axisymmetric case $\left(\dfrac{\partial}{\partial\varphi}, g_\varphi\right) = 0$, the specific angular momentum of each fluid particle must be conserved during its motion. However, the Eulerian scheme used here does not ensure the exact fulfillment of this conservation law. As a result, the specific angular momentum of fluid particles during their predominantly meridional flow can decrease. To check these concerns, we carried out an auxiliary calculation [3].

In calculation [3], which should be compared with calculation [1], the inner computational boundary was exactly at the radius of 4.010748×10^7 cm, and the distance to the radius of 8.764082×10^7 cm was covered by an additional 20 zones (the computational region was divided into 120 cells along the radius). So, in the remaining part of the computational region

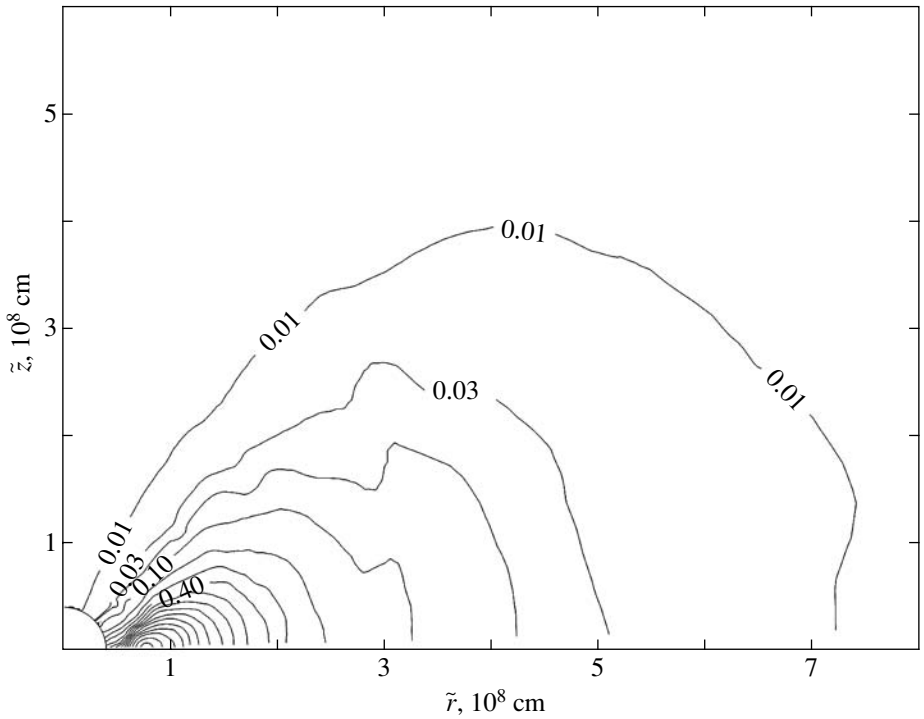

Fig. 4. Same as Fig. 2 for the test calculation [3] ($t_f = 6.388$ s). Here, there is no other family of lines of equal angular velocity.

(from the radius of 8.764082×10^7 cm to the outer boundary), the division into computational cells coincided exactly with the difference mesh from calculation [1]. The minimum specific angular momentum of the matter from calculation [1] determined at the final time was taken as the minimum admissible value. For matter with a specific angular momentum lower than the value in calculation [3], this value was taken to be identically equal to zero. The data of this calculation are shown in Fig. 4. The lines of equal density, if they are carefully compared with those in Fig. 2, show that the coordinates of the density maximum remained essentially unchanged. As we see from this comparison, the density maximum located in Fig. 2 near a radius $r \approx 0.95$ is clearly established at a radius $r \approx 0.8$ in Fig. 4 for the test calculation. This circumstance removes the above concerns about the decisive influence of the boundary condition specified at the inner boundary on the formation of an atmosphere.

In addition, the results obtained in calculations [1] and [2] should be interpreted as follows. Let $j_{\min}$ be the minimum specific angular momentum of the atmospheric matter in a steady equilibrium state. The simulated steady-state rotating atmosphere is then a result of the post-shock accretion of the outer layers of a high-mass star with the bulk of their rotating matter at the initial time having specific angular momenta higher than the above value of $j_{\min}$. In calculations [1] and [2], the total mass of the matter remaining inside the computational region by the establishment of a steady state is $\sim 0.13 M_\odot$. As we see from the plots in Fig. 1, a steady-state configuration is formed in a time of approximately 6 s; subsequently, the outflow of matter from the computational region virtually ceases, although its weak outflow results from the possible violation of the law of conservation of specific angular momentum. The rates of artificial accretion and ejection due to this circumstance are so low that they have no appreciable effect on the final result of our calculations.

Figure 5 shows lines of constant angular velocity for the final time ($t_f = 9.678$ s) of calculation [2]. As we see from the figure, the angular velocity distribution is cylindrical in pattern; i.e., it depends only on the cylindrical radius $\tilde{r}$ and does not depend on the other cylindrical coordinate $\tilde{z}$. In this case, appreciable deviations from this rotation law appear only in the low-density regions outside the thick disk concentrated near the axis within $\theta \leq \pi/4$. The rotation law $\partial\omega/\partial\tilde{z} = 0$ under discussion and the barotropy of the equation of state $P = P(\rho)$ for steady-state rotating self-gravitating matter are known to be equivalent (Tassoul 1978). The lines of constant (gray) angular velocity were also plotted in Figs. 2 and 3. Their shape also confirms the aforesaid.

More accurate data on the angular velocity distribution for calculation [2] are presented in Fig. 6. In this figure, the angular velocities taken on different

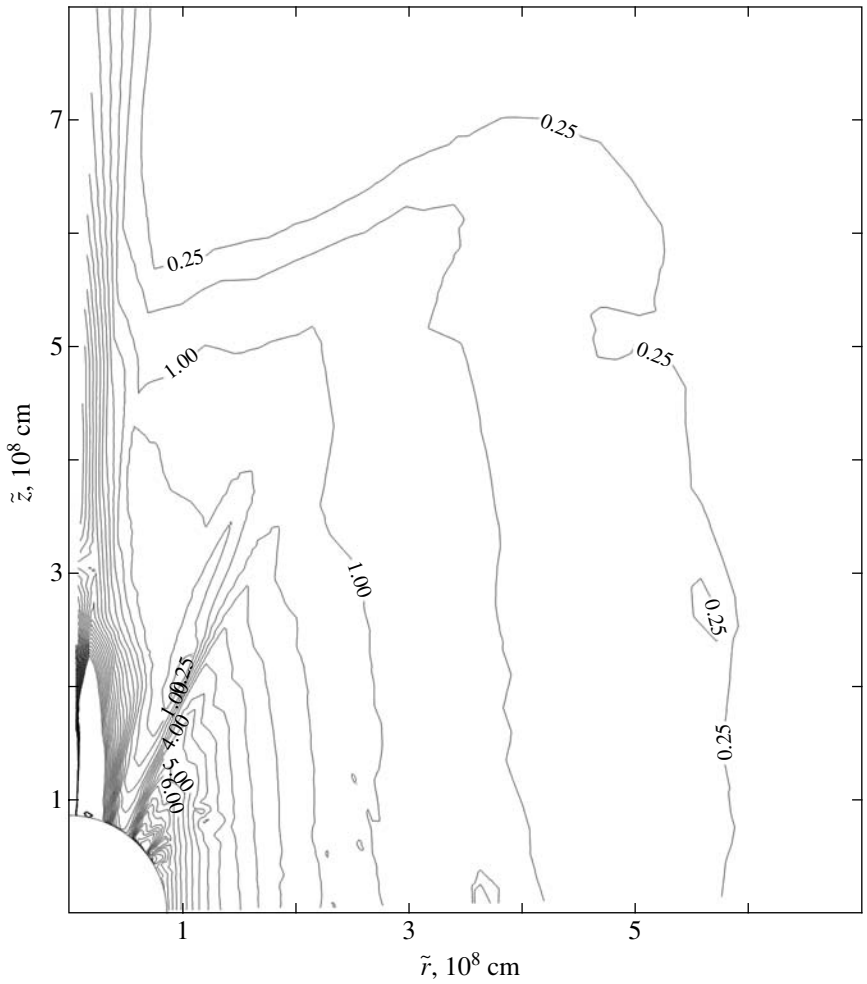

Fig. 5. Lines of equal angular velocity ω at the final time for calculation [2] ($t_f = 9.678$ s).

rays (their angles are measured from the rotation axis) are plotted against the cylindrical radius $\tilde{r} = r\sin\theta$. As we see, all points satisfactorily fall on the same curve that is best fitted by a power law of the form $\omega = \omega_0^*(r\sin\theta)^\alpha$ rather than an exponential (Gaussian) law of the same argument. Thus, the best fit to the steady-state rotation law in a thick disk is

$$\omega = \omega_0^*(r\sin\theta)^\alpha = 6.0562(r\sin\theta)^{-1.8044}\ \mathrm{s}^{-1}, \quad (16)$$

where the spherical radius r is given in units of the problem $[r] = 10^8$ cm from (11). Note that the exponential (Gaussian) best fit shown in Fig. 6 had $\omega_0 = 13.207\ \mathrm{s}^{-1}$ and $r_0 = 1.706$ (in units of $[r] = 10^8$ cm), but its quality was much lower than that of the power-law fit (16). Thus, we can easily confirm the above assertion that the specific angular momentum is at a minimum near the inner boundary of the computational region. Indeed, $j = \omega r^2\sin^2\theta = \omega_0^*(r\sin\theta)^{0.1956} \propto r^{0.1956}$; i.e., the function increases monotonically but very slowly with radius r.

A remark should also be made about the identification of the presupernova envelope layers that entered into the composition of the toroidal atmosphere rather than collapsing onto the PNS embryo or being ejected outward. The law of conservation of local specific angular momentum allows this identification to be made in principle, because this law is actually violated in the numerical solution (see above). This approach clearly reveals that a rather narrow layer of matter is transferred into the atmosphere from the outer part of the initial iron core and the silicon shell of the presupernova. The assertion that the layer of matter transferred into the toroidal atmosphere is narrow is based on the insignificant change in local angular momentum obtained in our calculation ($j \propto r^{0.2}$). Since the change in atmospheric radius does not exceed a factor of 10, the angular momentum j changes by a factor of $\sim$1.5 (from $j_{\min} \approx 1.51 \times 10^{17}$ to $j_{\max} \approx 2.28 \times 10^{17}\ \mathrm{cm}^2\ \mathrm{s}^{-1}$), while the initial angular momentum changes by a factor much larger than $\sim$10. Figure 7 shows the initial distribution of

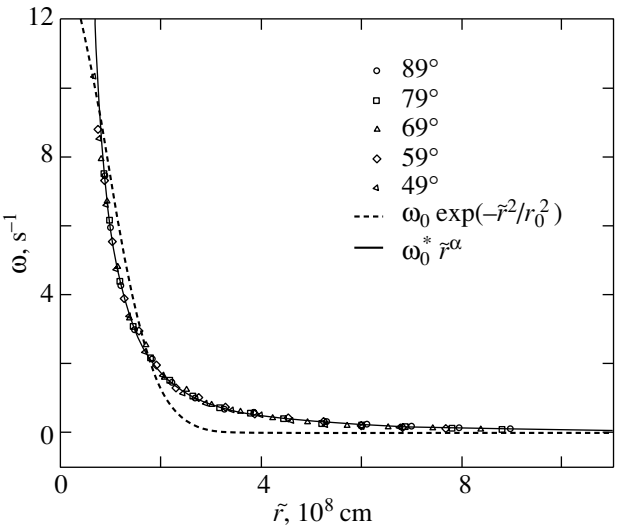

Fig. 6. Angular velocity ω versus cylindrical radius $\tilde{r}$, as constructed from the data on different rays (with a given constant angle θ) at the final time for calculation [2] ($t_f = 9.678$ s): separate points on the rays adjacent to the equator at the location of the thick disk. The analytical fits are represented by the solid (power law) and dashed (exponential) lines. The parameters ω_0^*, ω_0, and r_0 are given in the text.

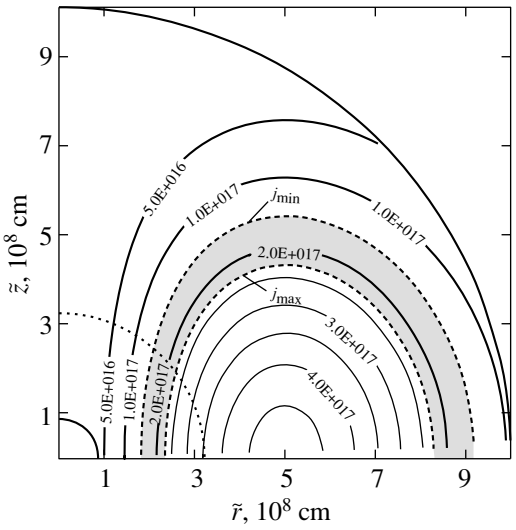

Fig. 7. Lines of equal specific angular momentum j at the initial time for calculation [1]. The region of matter whose specific angular momentum lies within the range from $j_{\min} \approx 1.51 \times 10^{17}$ to $j_{\max} \approx 2.28 \times 10^{17}$ cm^2 s^{-1} is colored gray; $j_{\min}$ and $j_{\max}$ are the limiting specific angular momenta in the toroidal atmosphere at the final time $t_f = 29.034$ s). The dotted line represents the boundary of the region of constant entropy.

angular momentum j in accordance with the specified ω distribution (14) (for the constants ω_0 and r_0, see above) in spherical radius r. In this figure, the region of matter whose specific angular momentum j lies within the range from $j_{\min}$ to $j_{\max}$ (see above) and which, therefore, could enter the toroidal atmosphere is colored gray. Note that the light areas in Fig. 7 represent the matter that either fell through the inner boundary to the central PNS or was ejected through the outer boundary into outer stellar layers.

Let us consider the question of how strongly the derived nonzero temperatures of the matter in a toroidal atmosphere affect the numerical solution. The temperature reaches its maximum near the density maximum of a toroidal atmosphere ($\rho_{\max}$ at $r_{\max}$), $\sim 3 \times 10^9$ K, with solely iron nuclides being present in the nuclear composition of the atmospheric matter. As can be easily verified, this temperature, with the adopted equation of state, leads to a significant temperature correction to the pressure (see Table 1) and specific internal energy of the matter (see Table 2), mainly through an increase in the pressure and specific internal energy of the electron–positron matter and through the appreciable effect of the blackbody radiation at these temperatures. The estimate of the temperature effect by Imshennik and Manukovskii (2000) as $T \sim 2 \times 10^9$ K also qualitatively agrees with its numeric determination in our calculation. Let us discuss the question of whether these temperature corrections are consistent with the requirement that the equation of state for the matter be barotropic. Below, we discuss calculation [1]. Figure 8a shows the initial spherically symmetric distribution of specific entropy S in cylindrical radius $\tilde{r}$ on the equator. The matter that can be in the composition of a toroidal atmosphere (with the corresponding specific angular momentum) is colored gray. The volume in which this matter is contained has the shape of a hollow torus (see Fig. 7). Within this region, the specific entropy takes on two almost constant values: $S_1 \approx 2.4 \times 10^8$ erg g^{-1} K^{-1} up to the radius $r \approx 3.2 \times 10^8$ cm (see Fig. 8a) at which the specific entropy abruptly changes (this radius is marked by the dotted line in Fig. 7) and $S_2 \approx 4.4 \times 10^8$ erg g^{-1} K^{-1} at larger radii. In Fig. 8b, the adiabatic curves with specific entropies S_1 and S_2 are plotted in the (ρ, T) plane (the variables ρ and T are on a logarithmic scale). As we see from the figure, in the density range concerned (10^5–2×10^7 g cm^{-3}), the simple Poisson laws with almost constant and similar adiabatic indices $\gamma_1 \approx 1.346$ and $\gamma_2 \approx 1.307$ (see Fig. 8b) hold for S_1 and S_2, respectively. Thus, particles of matter with two different specific entropies (S_1 and S_2) could in principle enter a toroidal atmosphere, which would be strange in view of the requirement that the equation of state for the matter of a toroidal atmosphere be barotropic. Interestingly, the total masses of these two regions in Fig. 7 are close

Table 1. Pressures of the matter at density $\rho = 3.9 \times 10^6$ g cm^{-3} and two different temperatures (1.0×10^3 and 3.3×10^9 K)

T, K	$P_{\rm rad}$	$P_{\rm ep}$	$P_{\rm n}$	$P_{\rm tot}$
1.0×10^3	2.500×10^{-3}	1.891×10^{23}	5.791×10^{15}	1.891×10^{23}
3.3×10^9	2.904×10^{23}	6.028×10^{23}	1.897×10^{22}	9.122×10^{23}

Note: $P_{\rm rad}$ is the blackbody radiation pressure; $P_{\rm ep}$ is the pressure of the Fermi–Dirac electron–positron gas; $P_{\rm n}$ is the pressure of the perfect Boltzmann gas of nuclides; and $P_{\rm tot}$ is the total pressure of the matter ($P_{\rm tot} = P_{\rm rad} + P_{\rm ep} + P_{\rm n}$). The pressures are given in units of erg cm^{-3}.

Table 2. Specific internal energies of the matter at density $\rho = 3.9 \times 10^6$ g cm^{-3} and two different temperatures (1.0×10^3 and 3.3×10^9 K)

T, K	$\mathcal{E}_{\rm rad}$	$\mathcal{E}_{\rm ep}$	$\mathcal{E}_{\rm n}$	$\mathcal{E}_{\rm tot}$
1.0×10^3	1.940×10^{-9}	8.540×10^{16}	2.227×10^9	8.540×10^{16}
3.3×10^9	2.382×10^{17}	3.800×10^{17}	7.350×10^{15}	6.254×10^{17}

Note: $\mathcal{E}_{\rm rad}$ is the specific blackbody radiation energy; $\mathcal{E}_{\rm ep}$ is the specific energy of the Fermi–Dirac electron–positron gas; $\mathcal{E}_{\rm n}$ is the specific internal energy of the perfect Boltzmann gas of nuclides; and $\mathcal{E}_{\rm tot}$ is the total specific internal energy ($\mathcal{E}_{\rm tot} = \mathcal{E}_{\rm rad} + \mathcal{E}_{\rm ep} + \mathcal{E}_{\rm n}$). The specific internal energies are given in units of erg g^{-1}.

Table 3. Physical parameters of the numerical solutions for calculations [1–3] of toroidal atmospheres

Calculation	[1]	[2]	[3]
t_f, s	29.03449	9.678182	6.387759
$\rho_{\rm max}$, 10^7 g cm^{-3}	0.396113	0.374559	1.152099
$r_{\rm max}$, 10^8 cm	0.955023	0.981689	0.766656
$M^{\rm tot}$, $M_\odot$	0.117120	0.121641	0.211936
$J^{\rm tot}$, 10^{49} cm^2 s^{-1} g	4.453701	4.716711	8.152932
$E_{\rm in}^{\rm tot}$, 10^{50} erg	0.604490	0.635241	1.203042
$E_{\rm gr}^{\rm tot}$, 10^{50} erg	−1.792622	−1.786542	−3.893123
$E_{\rm kin}^{\rm tot}$, 10^{50} erg	0.507197	0.528444	1.228717
$E_{\rm kin}^{\rm rot}$, 10^{50} erg	0.501609	0.509417	1.169783

Note: t_f is the final time of the calculation; $\rho_{\rm max}$ is the density maximum; $r_{\rm max}$ is the cylindrical radius at which the density maximum is located; $M^{\rm tot}$ is the total mass; $J^{\rm tot}$ is the total momentum; $E_{\rm in}^{\rm tot}$ is the total internal energy; $E_{\rm gr}^{\rm tot}$ is the total gravitational energy; $E_{\rm kin}^{\rm tot}$ is the total kinetic energy; $E_{\rm kin}^{\rm rot}$ is the rotational kinetic energy ($\propto V_\varphi^2/2$).

and equal to $M_1 = 0.1136 M_\odot$ and $M_2 = 0.1392 M_\odot$, respectively. Remarkably, $M_1 \approx M_2 \approx M^{\rm tot}$ (see Table 3) in this case. The data on the specific entropy distribution in the toroidal atmosphere itself, which are plotted in Fig. 9, introduce a larger uncertainty. They convincingly show that only particles with specific entropies in the narrow range $S \approx (3.3–4.5) \times 10^8$ erg g^{-1} K^{-1} entered the toroidal atmosphere. Thus, it is clear that only the second group of particles with the initial specific entropy S_2 constituted the toroidal atmosphere obtained in our calculations. At the same time, the first group of particles with the initial specific entropy S_1 was accreted onto the PNS embryo (or may have been ejected outward through the outer boundary) in the post-shock accretion process under study. As a result, the equation of state for the matter of a toroidal atmosphere proved to be approximately barotropic, given some errors in the

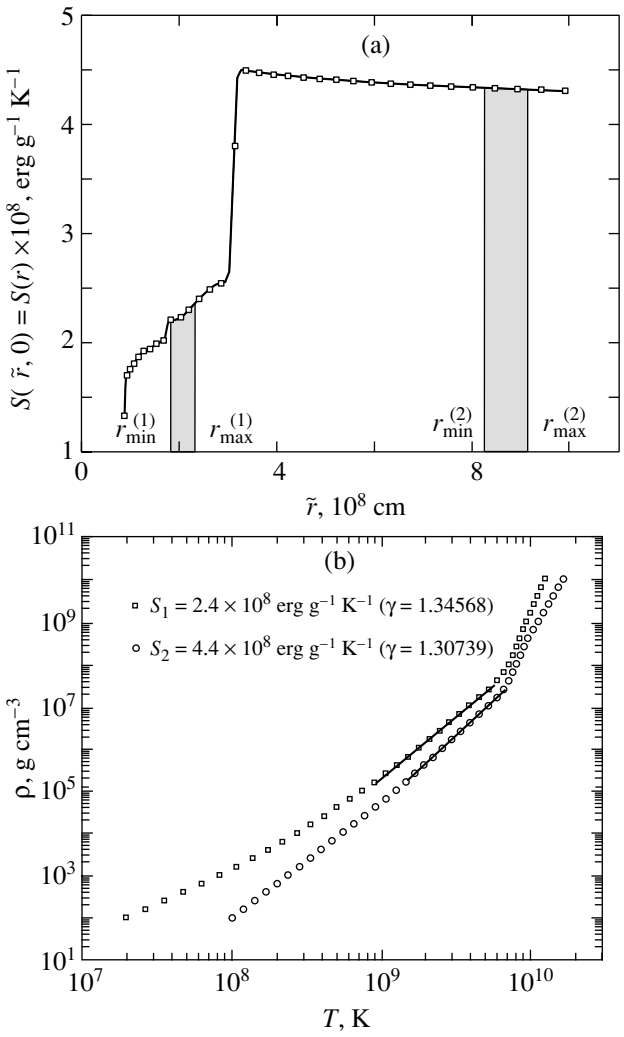

Fig. 8. (a) Specific entropy S versus cylindrical radius $\tilde{r}$ on the equator for calculation [1] at the initial time ($r_{\min}^{(1)} \approx 1.82 \times 10^8$ cm, $r_{\max}^{(1)} \approx 2.35 \times 10^8$ cm and $r_{\min}^{(2)} \approx 8.28 \times 10^8$ cm, $r_{\max}^{(2)} \approx 9.15 \times 10^8$ cm). (b) The adiabatic curves of the tabulated equation of state for two specific entropies, $S_1 \approx 2.4 \times 10^8$ erg g^{-1} K^{-1} and $S_2 \approx 4.4 \times 10^8$ erg g^{-1} K^{-1}. The rectilinear segments are the best linear fits to the adiabatic curves for the density range 10^5–2×10^7 g cm^{-3}.

entropy calculation, which, according to Fig. 8b, is quantitatively of little importance.

The fact that our numerical solution (see above) is approximately isoentropic (i.e., $\nabla S \cong 0$) (Fig. 9) has a direct bearing on the dynamical stability of toroidal atmospheres. The Viertoft–Lebowitz stability criterion exists for the axisymmetric motions under consideration (Tassoul 1978). In our case (constant entropy), this criterion is

$$\frac{\partial j^2}{\partial \tilde{r}} > 0 \qquad (17)$$

and, as can be easily verified, it is satisfied in accordance with (16). We immediately see from Fig. 9 that the angular velocity distribution in regions with a variable specific entropy ($\nabla S \neq 0$) deviates appreciably from the cylindrically symmetric distribution ($\partial\omega/\partial\tilde{z} \neq 0$). This property is in close agreement with one of the corollaries of the more general formulation of the above criterion (Tassoul 1978).

It is well known that an analytical solution in the form of rotating toroidal atmosphere can be constructed in the axisymmetric case in the Roche approximation for matter with the equation of state of a cold iron gas and arbitrary relativity (Imshennik and Manukovskii 2000). In this case, the dependence on the cylindrical radius alone is the only constraint imposed on the rotation law. If we generalize the analytical solution from the cited paper to the power-law rotation (16), then for our empirically derived rotation law, the formula for the atmospheric density distribution in the plane that passes through the rotation axis is

$$\rho(r,\theta) = B^{-3}\left\{\left[\sqrt{1 + B^2\rho_0^{2/3}} + \frac{GM_0}{M}\left(\frac{1}{r} - \frac{1}{r_0}\right) + \frac{(\omega_0^*)^2}{(2\alpha+2)M} \times \left\langle (r\sin\theta)^{(2\alpha+2)} - (r_0\sin\theta_0)^{(2\alpha+2)}\right\rangle\right]^2 - 1\right\}^{3/2}, \qquad (18)$$

where $B = 7.792 \times 10^{-3}$ cm g$^{-1/3}$ and $M = 2.272 \times 10^{17}$ cm^2 s^{-2} are the constants from the equation of state, G is the gravitational constant, M_0 is the mass of the central object, and (r_0, θ_0) are the coordinates of the point at which the boundary density ρ_0 is specified; the dimension relation for the coefficient ω_0^* is $[\omega_0] = \lfloor \omega_0^* r_0^\alpha \rfloor$. In Fig. 10, the lines of equal density for this analytically specified atmosphere are compared with the lines of equal density for the atmosphere obtained in calculation [1]. The parameter $M_0 = M_{\rm gr} = 1.93 M_\odot$ (see Fig. 1) was taken from our calculation. The constants ρ_0, r_0, and θ_0 were chosen so that the total atmospheric mass from the analytical solution was equal to the numerically calculated atmospheric mass. It should be noted that this choice is ambiguous. However, a common property for any admissible set of these parameters is not only the total mass of the atmosphere but also the position of its density maximum. The latter is determined solely by the properties of the analytical solution and does not depend on these parameters. As we see from Fig. 10, a more compact and denser atmosphere corresponds to the analytical solution. This difference could be explained by the use of different equations of state and by the fact that the meridional flow of matter, which is clearly present in the numerical calculation,

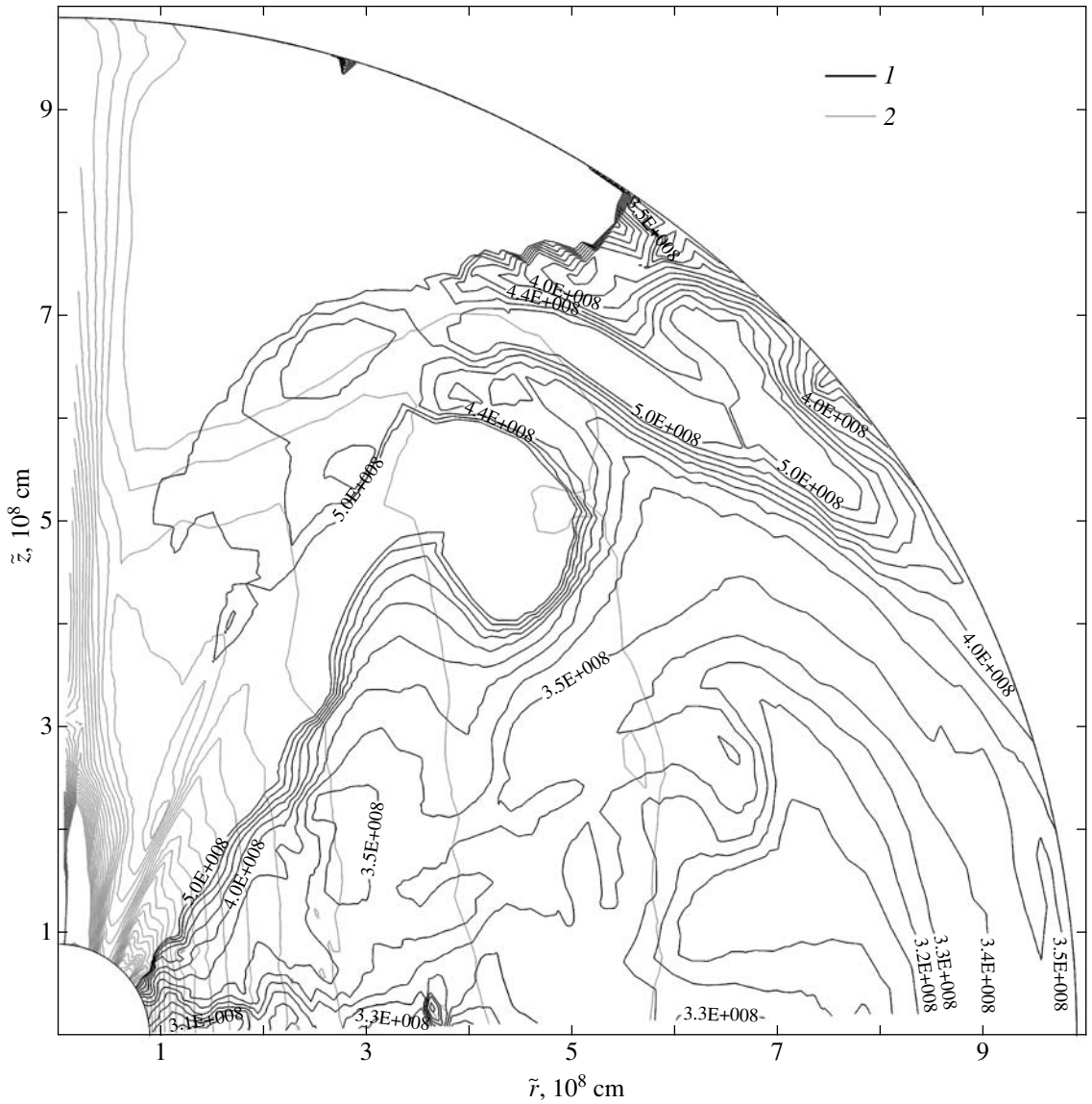

Fig. 9. *1*—Lines of equal specific entropy at the final time for calculation [1] ($t_f = 29.034$ s); *2*—lines of equal angular velocity ω for the same time.

was disregarded when deriving the analytical formula. In Fig. 11, atmospheric density is plotted against radius in the equatorial plane. This figure shows the density profiles for both calculations, [1, 2], taken at different times. As we see from the figure, the atmospheric density in calculation [2] (on a finer mesh) is appreciably lower than the density from calculation [1]. The reason is as follows: in calculation [2], at approximately the fifth second of our calculation, we observed the fragmentation of the atmosphere that had already formed by this time; as a result, part of the matter was ejected outward. Concurrently with the fragmentation, the rotation law of the atmosphere changed to a form independent of the cylindrical coordinate $\tilde{z}$. In calculation [1] (on a coarse mesh), we observed no such event; to be more precise, weak perturbations were noticeable near the above time of the calculation (5 s), but they did not eventually lead to its fragmentation. We carried out an additional test numerical calculation [4] on an even finer mesh. The total number of zones in calculation [4] was 200 in the radial direction and 60 in the direction of change of the polar angle. This calculation also confirmed the fragmentation of the atmosphere. In both calculations ([2, 4]), the initial perturbation that arose at the inner boundary of a toroidal atmosphere led to intense ejection of a small fraction of atmospheric matter in the axial direction and to a division of the main volume of the thick disk into two parts approximately equal in mass. As the outer atmospheric fragment receded

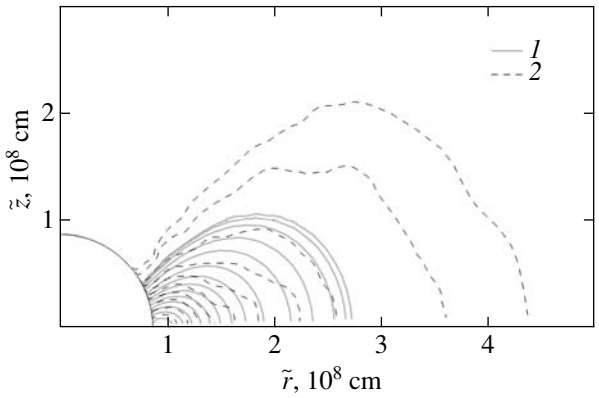

Fig. 10. Comparison of the lines of equal atmospheric density at the final time for calculation [1] (*1*) (t_f = 29.034 s) and the lines of equal density for the analytical solution (*2*).

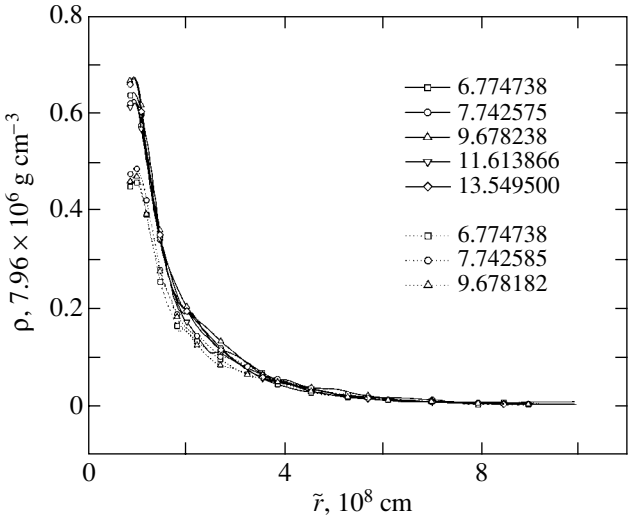

Fig. 11. Atmospheric density versus cylindrical radius $\tilde{r}$ in the equatorial plane at various times for calculations [1] (solid lines) and [2] (dotted lines).

from the center, part of the matter was transferred back onto the remnant. As a result, the mass of the outward ejected matter did not exceed 30% of the total mass of the thick disk before the onset of fragmentation. The fact that fragmentation in both calculations (calculation [2] and test calculation [4]) began at the same time and developed identically most likely suggests that the observed fragmentation is not numerical in origin.

Table 3 gives the physical model parameters obtained in calculations [1–3] of toroidal atmospheres. The integrated quantities in the table refer to the entire computational region. Without any particular error, they may be considered to pertain to the atmosphere, because the latter has no well-defined boundary. In addition, its surrounding matter has such a low density that it gives no significant contribution to the integrated quantities. These integrated quantities qualitatively agree with those obtained in the analytical solution (cf. the data from Table 1 for $M = 1.8M_\odot$ from Imshennik and Manukovskii (2000)). Of course in this case, there are appreciable differences between the differential rotation laws of the atmospheres being compared (see above in this section). Finally, note that the parameters in calculation [3], in which the inner boundary of the computational region was moved to the center by twice the radius, significantly differ. This change can be mainly explained by the fact that the density maximum is closer to the center and corresponds to a lower specific angular momentum that a substantial mass of the matter has in the initial state; in particular, it can be explained by the shorter computational time. Unfortunately, the influence of the boundary condition itself, which simulates the physical transparency condition for this Eulerian boundary very roughly, cannot be ruled out either. This question probably needs further study.

CONCLUSIONS

The formation of a toroidal atmosphere near a protoneutron star obtained by the hydrodynamic method may be considered to be the main result of our study. The parameters of this atmosphere with a specified initial rotation law in the outer layers of a high-mass presupernova with a structure from the evolution calculations by Boyes *et al.* (1999) were found to be the following: $M^{\rm tot} = (0.117{-}0.122)M_\odot$, $J^{\rm tot} = (0.445{-}0.472) \times 10^{50}$ erg s, $\rho_{\rm max} = (0.375{-}0.396) \times 10^7$ g, and $r_{\rm max} = (0.955{-}0.982) \times 10^8$ cm (calculations [1, 2]). The ranges of these quantities characterize the accuracy of our numerical model for the axisymmetric two-dimensional hydrodynamic problem on post-shock accretion onto the PNS embryo. The atmospheric parameters for the auxiliary calculation [3] differ markedly for the reasons given above (see the Section "Results of the numerical solution"): $M^{\rm tot} = 0.21M_\odot$, $J^{\rm tot} = 0.82 \times 10^{50}$ erg s, $\rho_{\rm max} = 1.2 \times 10^7$ g cm^{-3}, and $r_{\rm max} = 0.77 \times 10^8$ cm. Of course, this set of numerical results is attributable to the rotation law specified in the initial conditions. Moreover, this law provided a reasonable PNS mass of $\sim 1.8M_\odot$ at the end of our calculation because of the outward ejection of a relatively large mass of $\sim 0.8\mathrm{M}_\odot$ and the formation of a toroidal atmosphere with a mass of $\sim 0.2\mathrm{M}_\odot$ (the initial mass was equal to the sum of $\sim 1.0\mathrm{M}_\odot$ in the PNS embryo and $\sim 1.8\mathrm{M}_\odot$ in the outer presupernova layers up to the adopted radius of $\sim 10^9$ cm). This mass distribution between the PNS and the atmosphere was previously obtained in the quasi-one-dimensional calculations

of the collapse of an iron stellar core with a mass $M = 2M_\odot$ by Imshennik and Nadyozhin (1992). This is not surprising, given the similarity between the rotation laws with the total angular momentum $J_0 \sim 10^{50}$ erg s specified in the initial conditions of the two problems (for the problem within the iron core of mass $M_{\rm Fe} \sim 1.6M_\odot$ discussed here). It seems that the chosen rotation law has yet to be justified by gradually developing evolution calculations for rotating high-mass stars until the onset of their collapse, which is undoubtedly a very complex problem. The barotropic properties of atmospheres and the z independence of their angular velocity ω established in our numerical calculations are sufficient conditions for the validity of the Lichtenstein theorem (see, e.g., Tassoul 1982) that states the existence of an equatorial symmetry plane, a property that is obvious at first glance but far from trivial in reality. Thus, it is quite justifiable to use equatorial symmetry to simplify the numerical solution (see the Subsection *Boundary Conditions*).

It should also be emphasized that the numerically calculated specific parameters of toroidal atmospheres are largely determined by the form of the chosen initial rotation law for the inner presupernova layers (the outer part of the iron core and the silicon shell). In particular, they determine the fact that the matter that was initially in the region of the silicon shell (rather than the iron core) mainly entered the toroidal atmosphere (see the Section "Results of the numerical solution"). In addition, by choosing a different initial rotation law, we could avoid the nonuniformity in the specific entropy distribution of the matter from which a toroidal atmosphere is formed and, as a result, avoid its fragmentation (see above), which may well be associated precisely with this distribution. Nevertheless, the very formation of a toroidal atmosphere during post-shock accretion is a universal phenomenon that depends weakly on this circumstance.

The formulation of the problem on the formation of a toroidal atmosphere was itself largely reinforced by the existence of analytical solutions to the hydrostatic equilibrium equations for a cool iron atmosphere in the gravitational field of a protoneutron star (Imshennik and Manukovskii 2000). Our numerical solution, first, shows the stability of such atmospheres against two-dimensional perturbations (the hydrodynamic sense of the relaxation method!) and, second, removes several restrictions in the formulation of the problem by Imshennik and Manukovskii (2000) due to the allowance for nonzero matter temperature and the effect of self-gravitation, which undoubtedly does not extend beyond minor corrections given the above parameters of a toroidal atmosphere.

ACKNOWLEDGMENTS

We wish to thank A.V. Zabrodin for his assistance in developing the finite-difference method for solving the problem. This work was supported in part by the Russian Foundation for Basic Research (project no. 00-15-96572) and the Federal Program "Research and Development in Priority Fields of Science and Technology" (contract no. 40.022.1.1.1103).

REFERENCES

1. A. G. Aksenov, Pis'ma Astron. Zh. **25**, 226 (1999) [Astron. Lett. **25**, 185 (1999)].
2. A. G. Aksenov, S. I. Blinnikov, and V. S. Imshennik, Astron. Zh. **72**, 717 (1995) [Astron. Rep. **39**, 638 (1995)].
3. H. Bondi, Mon. Not. R. Astron. Soc. **112**, 195 (1952).
4. H. Boyes, A. Heger, and S. Woosley, www.supersci.org (1999).
5. G. E. Brown, S. W. Bruenn, and J. S. Wheeler, Comments Astrophys. **16**, 153 (1992).
6. S. K. Godunov, A. V. Zabrodin, M. Ya. Ivanov, *et al.*, *Numerical Solution of Multi-Dimensional Gas-Dynamical Problems* (Nauka, Moscow, 1976).
7. V. S. Imshennik, *Astrophysics on the Threshold of 21st Century,* Ed. by N. S. Kardashev (Gordon and Breach Sci., Philadelphia, 1992), p. 167.
8. V. S. Imshennik and K. V. Manukovskii, Pis'ma Astron. Zh. **26**, 917 (2000) [Astron. Lett. **26**, 788 (2000)].
9. V. S. Imshennik and D. K. Nadyozhin, Itogi Nauki Tekh., Ser. Astron. **21**, 63 (1982).
10. V. S. Imshennik and D. K. Nadyozhin, Pis'ma Astron. Zh. **18**, 195 (1992) [Sov. Astron. Lett. **18**, 79 (1992)].
11. V. S. Imshennik and D. V. Popov, Pis'ma Astron. Zh. **20**, 620 (1994) [Astron. Lett. **20**, 529 (1994)].
12. V. S. Imshennik and M. S. Popov, Pis'ma Astron. Zh. **27**, 101 (2001) [Astron. Lett. **27**, 81 (2001)].
13. V. S. Imshennik, K. V. Manukovskii, D. K. Nadyozhin, and M. S. Popov, Pis'ma Astron. Zh. **28**, 913 (2002) [Astron. Lett. **28**, 821 (2002)].
14. P. Colella and P. R. Woodward, J. Comput. Phys. **54**, 174 (1984).
15. D. K. Nadyozhin, *Surveys High Energy Physics* (OPA, Amsterdam, 1998), Vol. 11, p. 121.
16. J.-L. Tassoul, *Theory of Rotating Stars* (Princeton Univ. Press, Princeton, 1978; Mir, Moscow, 1982).

Translated by V. Astakhov